Micromagnetic Simulations of Circular Nano-magnets for Room Operable Quantum Cellular Automata

BY

TEJUMADE DUROWADE

B.S., University of Illinois at Chicago, 2013

M.S., University of Illinois at Chicago, 2016

THESIS

Submitted in partial fulfillment of the requirements

for the degree of Doctor of Philosophy in Electrical and Computer Engineering

in the Graduate College of the

University of Illinois at Chicago, 2020

Chicago, Illinois

Defense Committee:

Vitali Metlushko, Chair and Advisor, Electrical & Computer Engineering

Sivalingam Sivananthan, Co-Adivsor, Department of Physics

Michael Stroscio, Electrical & Computer Engineering

Pai-Yen Chen, Electrical & Computer Engineering

Danilo Erricolo, Electrical & Computer Engineering

Se-Young An, Research Resource Center

DEDICATION

This thesis is dedicated to my loving family. You have all been there for me, never questioning, but always asking what I needed.

And to Richard and Faith Choi of University Bible Fellowship. For the hours of studying the Word of God together and your prayers of support and generosity.

May the Lord continue to smile on you all!

ACKNOWLEDGMENTS

CONTRIBUTION OF AUTHORS

Portions of sections 4.1 – 4.5 of Chapter IV. Simulation Dynamics were previously published in March 2020 in the open access journal AIP Advances, volume 3, number 10 under the title 'Micro-magnetic simulations of correlated switching in touching circular nano-magnetic elements.' In addition to the simulations performed by me, further advanced analysis of the presented data was performed by Vitali Metlushko. Reuse of the published material is in line with the publisher's copyright policy.

TABLE OF CONTENTS

TABLE OF CONTENTS

LIST OF FIGURES

LIST OF FIGURES (Continued)

LIST OF ABBREVIATIONS

CMOS   Complementary Metal Oxide Semiconductor

M Tr/mm2   Million Transistor per square millimeter

QC   Quantum Computing

PAL   Programmable Array Logic

RSA   Riverst-Shamir-Adleman

QCA   Quantum Cellular Automata

EQCA   Electronic Quantum Cellular Automata

SQCA   Superconducting Quantum Cellular Automata

JS   Josephson Junction

SQUID   Superconducting Quantum Interference Device

CBJJ   Current Biased Josephson Junction

RSFQ   Rapid Single Flux Quantum

MOQCA   Molecular Quantum Cellular Automata

MQCA   Magnetic Quantum Cellular Automata

STT   Spin Torque Transfer

OOMMF   Object Oriented Micro-Magnetic Framework

NIST   National Institute of Standards and Technology

LLG   Landau-Lifshitz-Gilbert

EBL   Electron Beam Lithography

PMMA   Poly (Methyl MethAcrylate)

TE   Thermionic Emission

FE   Field Emission

SEM   Scanning Electron Microscopy

TEM   Transmission Electron Microscopy

SUMMARY

We report on the study on the circular nano-magnets as candidates for room operable quantum cellular automata. As quantum computing paradigms are being explored to replace traditional metal-oxide-semiconductor transistors, we explore a new way of thinking about magnetic elements in computing. Owing to their bistability based on stable magnetization ground states, their extremely low power dissipation and ability to maintain magnetization for longs period time, interest in nano-magnetic elements is building.

We take a look at quantum entanglement in linear chains featuring touching elements. The roles of symmetry and aspect ratio in the switching dynamics of these chains is discussed as well as how those dynamics evolve with added elements. Implementing elementary circuit components is discussed as well as variations of a complex gate. The simulations herein represent a first step into the potential use of magnetic elements in quantum computing.

I.   Introduction to Quantum Computing

1.1   Moore's Law and Quantum Computing

The continued scaling of complementary metal-oxide-semiconductor (CMOS) transistors has resulted in beneficial advances for many fields of research over the decades. The current state-of-art features 51.82 million transistors per mm2 (M Tr/mm^2) on Samsung's 10 nm technology node and 52.51 M Tr/mm2 on TMSC's version. Intel's version of the technology node boasts an impressive 100.8 M Tr/mm2 although on a limited production [1,2,3]. New packaging techniques employed in tandem with existing technologies have stretched scaling far beyond its limits. However, approaching the next process node represents the proverbial hitting of the wall, as quantum mechanical effects begin to dominate transistor operation [4]. Further scaling would require mitigation of the technological challenges that abound in developing new process nodes in addition to implementing practical prototypes dominated by physics at the quantum level. This also proves extremely difficult when viewed on the economic front. According to the National Institute of Standards and Technology, in 1995, the cost of building a new fab facility was $1 billion, 1% of the annual semiconductor market. In 2010, the cost had risen to ~10% of the market at $50 billion. Upgrading and maintaining fab facilities for even smaller process nodes is becoming prohibitively expensive [5]. In fact, as of August 2018, GlobalFoundries announced it would end further development of its 7 nm and lower process nodes. The International Technology Roadmap for Semiconductors has also estimated that the dominance of quantum mechanical effects at these small process nodes would limit further development beyond 2018/2019 [4,6]. Alternative technologies, or more drastically, new forms of computing are needed in order provide the continued increase in performance we have come to expect from our computing devices.

Quantum computing (QC) could represent this next step in the evolution of computing. While classical computing is based on the principle of driving components away from equilibrium states, QC exploits the ground state energies of its elements, also known as qubits, in its operations. The representation of data is achieved by having distinct ground states define logic 1 and logic 0 states, with an additional state that is a superposition of both states [7]. Computation is the done as elements interact with one another via some phenomenological mechanism – each element deciding on its logic state based on its interaction with its neighbors. Tunability of the strength of interactions indicates the computer's robustness when deployed to solve some computational problem. At the end of computation, the computer's elements resolve themselves into classical 1 or 0 states to minimize the system's total energy and reach a solution.

To illustrate the concept of QC further, consider Figure 1 [8]. It shows a series of light switches that are to be turned on or off to minimize the total energy dissipated in a room while keeping the room sufficiently lit. One can associate with each switch a 'bias value' which could represent the importance of each switch to the objective. This is shown in the red or blue circle on each switch. Which switches stay on and which are off is determined by the coupling; illustrated in Figure 2 as the connections between all the switches. Each bias value and each coupling constant can be then be mapped to the Hamiltonian operator corresponding to the total energy of the system and given by

$$E(s) = \sum_i h_i S_i + \sum_i J_{i,j} S_i S_j \qquad (1.1)$$

where h_i is the bias value of ith switch, S_i and S_j are the on or off values of the ith and j^{th} switches respectively, and $J_{i,j}$ is the coupling between the ith and j^{th} switches. It denotes the minimum total energy dissipated by the light switches in the still sufficiently lit room. The complexity of the switch problem dramatically increases as more switches are added. For 100 switches, the number of possible outputs for the entire system is 10^{48}, more than half the number of atoms in the observable universe.

The amount of time required to run this problem on a classical computer would run into the hundreds to thousands of years. However, given that quantum mechanical effects happen on time scales that are much faster than their classical computing counterparts, the time required would be exponentially much less on a quantum system. This is what is known as 'Quantum Supremacy' [9]. Achieving this feat would represent a paradigm shift in how the world does computing.
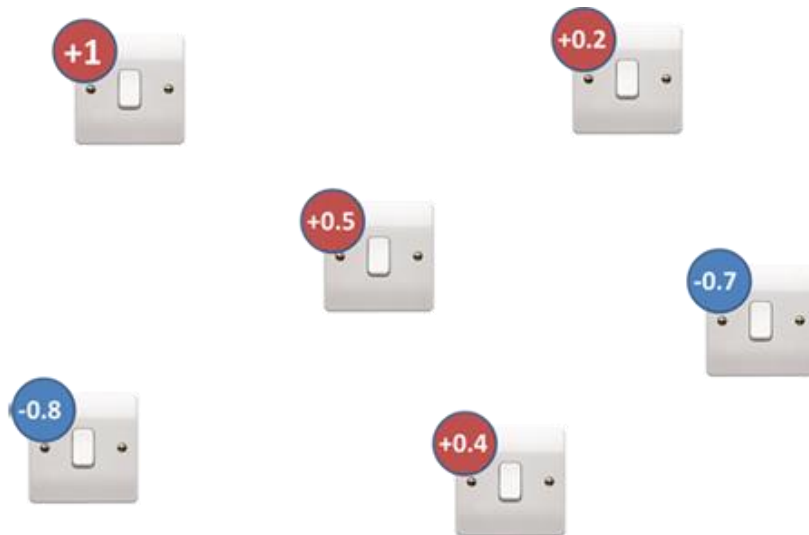
Figure 1 A set of switches in room with associated bias value [8].
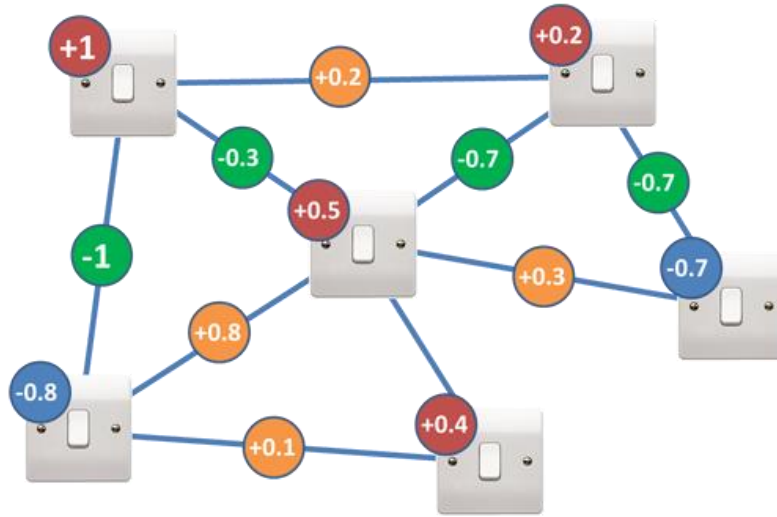
Figure 2 A set of switches in room with associated bias value and coupling constants [8].

To achieve this, a quantum computer would first require feasible and robust computing elements. At present, several have been proposed but resulted in few working prototypes. Secondly, it would require the implementation of an algorithm that evaluates the myriad of states in (1.1) and computes the best solution with regards to the problem statement. With a run of the mill algorithm like Simulated Annealing, solutions are calculated and then accepted or rejected based on a probabilistic distribution of minima in the entire solution space [10]. This approach left to run on a quantum computer would provide a final solution at the end of the computation that would be an average of 'best solutions' the computer came up with. The veracity of the solutions produced by a quantum computer is thus a sticking point as the quality of the applied algorithm greatly affects the precision with which the system provides optimal solutions. The switch problem above gives some insight into the complexity of designing algorithms for quantum computing. Coupling is present because interactions between a switch and its neighbor determine if said switch is left on or off. How that coupling is

achieved and how can it be tuned then gives birth to a further question, – how can the quantum computer be made programmable?

Programming new functions unto an existing architecture is an important aspect of computing. Classical computers do this by employing switching elements as connection points between larger operational elements. In Programmable Array Logic (PAL) devices for example, any array of inputs can be selectively diverted towards available logic gates at the output in varying combinations, thereby achieving an overarching logic function [11]. In the case of QC though, the governing principle is given by the Hamiltonian operator. Theoretically, this means interactions between elements spatially located far from one another can affect the resulting computation and overall energy of the system [7]. In practice though, contributions from far away neighbors are less likely to have a significant impact on the result of a computation. A point of consideration then is the number of neighbors one includes in computation – nearest neighbors only, second, or third order neighbors?

1.2   Impact of Quantum Computing

Quantum computing goes beyond application to specialized problems in physics and engineering. In medicine, sequencing deoxyribonucleic acid and protein samples could speed up the discovery of new drugs and help bring them to the market faster. Medical imaging could also see benefit as QC in tandem with machine learning would allow for more advanced analyses of images taken during the treatment process. Optimization of disease diagnosis and treatment with drugs tailored to individual patient genomes would be possible [12,13]. Other areas such as weather forecasting would see improved modeling capabilities and more reliable long-term forecasting.

In cryptography, the world's dependence on encryption for sensitive information such bank transactions and internet traffic would be significantly impacted. A quantum computer could perform

factorization of large integers used in cryptography much faster than a classical computer. It is not out of the realm of imagination that brute force attacks by nefarious actors on critical systems and infrastructure would be far easier to mount if a quantum computer boasted the density and operational reliability of today's computers. In fact, a quantum computer running Shor's algorithm would be capable of breaking the Riverst-Shamir-Adleman (RSA) cryptosystem in just 229 hours with 1.12×10^7 physical qubits [7]. It is no surprise then that governments around the world view QC as paramount to their national security and true to form, algorithms that employ mathematical problems that can be intractable even for large quantum systems are being researched at places like the U.S. National Institute of Standards and Technology.

For the promises it offers, QC is not without its controversies. The most recent being the claim and counterclaim by Google and IBM respectively regarding Google's achievement of quantum supremacy. Google's publication in October 2019, mentioned the use of 53 qubits on its Sycamore programmable superconducting processor. The computational task given to the computer was sampling the output of a pseudo-random quantum circuit by comparing how often output strings were observed experimentally to their ideal probability simulated on a classical computer. They claimed the sampling of the processor took 200 seconds for 1 million cycles. They also estimated this task would take a modern classical computer 10,000 years [14]. Enter IBM with pre-emptive response to a leaked manuscript of Google's publication. They claimed that the classical Summit supercomputer could accomplish a similar task with classical algorithms in a matter of days by breaking it into smaller sub-tasks [15]. The question of who is right or wrong is up in the air, though both present valid arguments. In the case of IBM, perhaps a better way of solving such difficult problems would be the efficient use of current architectural techniques coupled with new ways to represent information algorithmically. From Google's point of view, it is a matter of practicality as what is represented on paper may not always translate to effective use of resources in the real applications. Both sides present reasonable

arguments though both approaches are resource intensive and require significant financial investments. Needless to say, until more examples of quantum supremacy can be demonstrated, *nullius in verba*.

At present, QC today could be said to be analogous to what computing was in the early 20th century when computers like ENIAC occupied entire rooms and performed a modest number of calculations with the aggressive maintenance [16,17]. Regardless of the challenges that still face QC, it is imperative to explore all avenues that could lead to realizing a multi-purpose computer that addresses fundamental aspects such as element viability, coherence, tunability, and fidelity of solutions.

1.3   Quantum Cellular Automata

First proposed in 1993 by Craig Lent et al., Quantum Cellular Automata (QCA) are the building blocks of any QC regime. QCAs consist of cells arranged in pre-determined architectures designed to achieve some form of information transmission locally via one or more quantum mechanical phenomena. The bistability of the QCA cell or qubit is contingent upon having two stable ground states that can be used to represent logic states 1 or 0. These states could be based on various phenomenon such as [18,19]

- Electronic charge configuration - Coulomb repulsion between quantized charge particles

- Collective magnetic moments – interaction between magnetic moments

- Superconducting ground states – superconducting currents

- Nuclear spin or position – occupied orbitals of a molecule

Cell-cell interaction is possible either directly through or in response to a quantum property of the cell, e.g. charged particles, fields, or energy levels. The switching of any individual cell happens as it interacts with its neighbors to reach an equilibrium state. No direct connection to the interior of the

cell is present, hence the cell will always tend to its equilibrium ground state, meaning adiabatic operation of the system possible. For quantum effects to be dominant, cell size needs to be small. How small depends on the type of quantum effect being exploited. Environmental conditions and physical proximity to neighboring cells are also important to ensure the desired mechanism dominates the area occupied by the cells [18,19,20].

QCAs offer substantial advantages. As mentioned above, the lack of connections to the cell interior means the difficultly of optimizing interconnect layouts can be eliminated. This can lead to increased density of on-chip elements in tandem with the size restrictions posed in the quantum regime. The additional operation at ground logic states means, extremely low power dissipation which in turn could lead to even higher density storage elements. They offer faster operational frequencies, as the timescale attributed to quantum effects are much faster than their classical counterparts. All in all, they can be used to solve problems that have plagued the CMOS industry for decades [5].

The number of cells that can be coupled is unique to each QCA system and it can vary with parameters such as cell size, temperature, and quality of fabrication, amongst others. Coherence is therefore a limiting factor when considering what can be QCA. Currently, many types of QCA exist. Exotic options based on atomic vacancies in aggregate lattices, topological models, and trapped ions have been proposed, but this work will discuss models that have either working prototypes or offer potential for breakthrough computing in the future.

1.4   Low Temperature QCA

A class of QCA employing cells at liquid helium temperatures. These include silicon or metallic quantum dots, or superconducting loops. Operation at these low temperatures is paramount to isolate the qubits from the environmental conditions that would otherwise cause decoherence.

1.4.1   Electronic QCA (EQCA)

Commonly depicted as the four or six-dot model with coupled electrons occupying two dots in the cell at any given time. The diagonal along which the electrons sit is used to represent logic states. The extra set of dots in the six-dot model represent a reset or null state as depicted in Figure 3. The cell structure is based on the quantum confinement of electrons with charge quantization responsible for the cell polarization [18,19]. A clocked version of this model uses a clocking signal, typically a time varying voltage to force the cell into or out of the null state. Initially, the signal relaxes the null state dot energies below those of the active states and the electrons tunnel into the null state dots. Conversely, when the signal raises the null state dot energies above those of the active states, the electrons tunnel into one of the active states.

Polarization P = +1
Bit Value "1"

Polarization P = -1
Bit Value "0"

Polarization P = 0
Null/Reset State

(a)   (b)   (c)
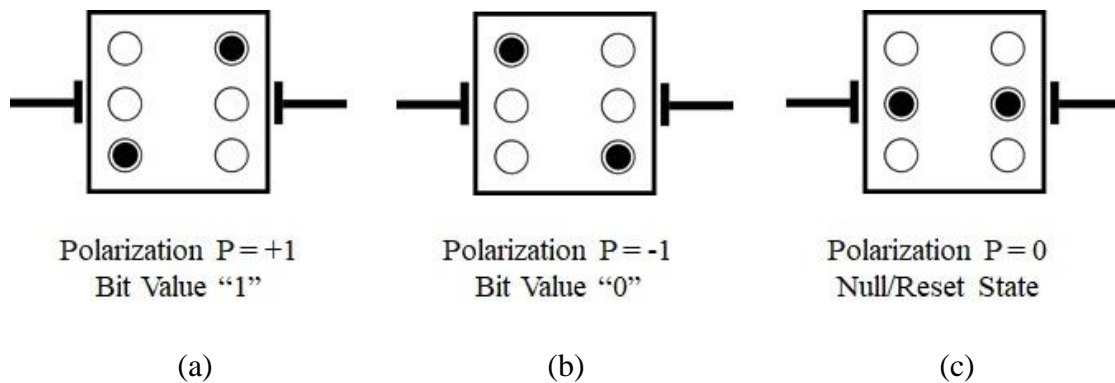
Figure 3 Unit cell representations of EQCA with (a, b) representing the active logic states. (c) Represents the reset state. The potential of the middle dots is varied by a clock potential, switching the cell from the null state to the active state.

The coupling mechanism between neighboring cells is Coulomb repulsion. The polarization of one cell forces the opposite polarization in a neighbor as the electrons will repel each other if they meet

at adjacent edges. This is edge driven switching as information can enter a cell only through the edges with no external connection needed. It is then easy to see as in Figure 4A that a simple wire would be 2 or more cells put together in a line. In Figure 4B, a logical NOT gate is formed by duplicating the input line and shifting the duplicates up and down. The rightmost cell of these duplicates meets the leftmost cell of the output line and Coulomb repulsion forces the opposite polarization to propagate down the output line. More complex logic is possible with a majority gate where the output polarization is determined by the majority polarization of the inputs. In Figure 5, the input cells A and B, are the of the same polarization and therefore the majority. They force the center cell to respond and the output cell, D, mirrors the polarization of the majority inputs. This is essentially the logical AND operation of inputs A and B.

Designs for larger building block components such as adders have been proposed by [21,22,23]. Figure 6 shows the schematic representation of a 1-bit ripple carry adder that uses three majority gates and two inverters. The sum given in (1.2) can also be written as a majority function of input bits as in (1.3). Similarly, the carry bits are represented by (1.4) and (1.5). Naturally, one can see that this could lead to assembling an arithmetic logic unit and eventually a processor. Electronic QCA designs of complex components employing majority gates have been extensively studied and simulated. From multipliers and dividers, to multiplexers, proposed designs rely four or six-dot models have been studied, some in QCA Designer, an open source simulator from the University of British Colombia [24,25,26,27,28].

$$s_i = a_i b_i c_i + a_i \overline{b_i}\, \overline{c_i} + \overline{a_i} b_i \overline{c_i} + \overline{a_i}\, \overline{b_i} c_i \qquad (1.2)$$

$$s_i = M\,\{\overline{M}(a_i, b_i, c_i), M\,(a_i, b_i, \overline{c_i}), c_i\} \qquad (1.3)$$

$$c_{i+1} = a_i b_i + b_i c_i + a_i c_i \qquad (1.4)$$

$$c_{i+1} = M(a_i, b_i, c_i) \qquad (1.5)$$

(a)

(b)
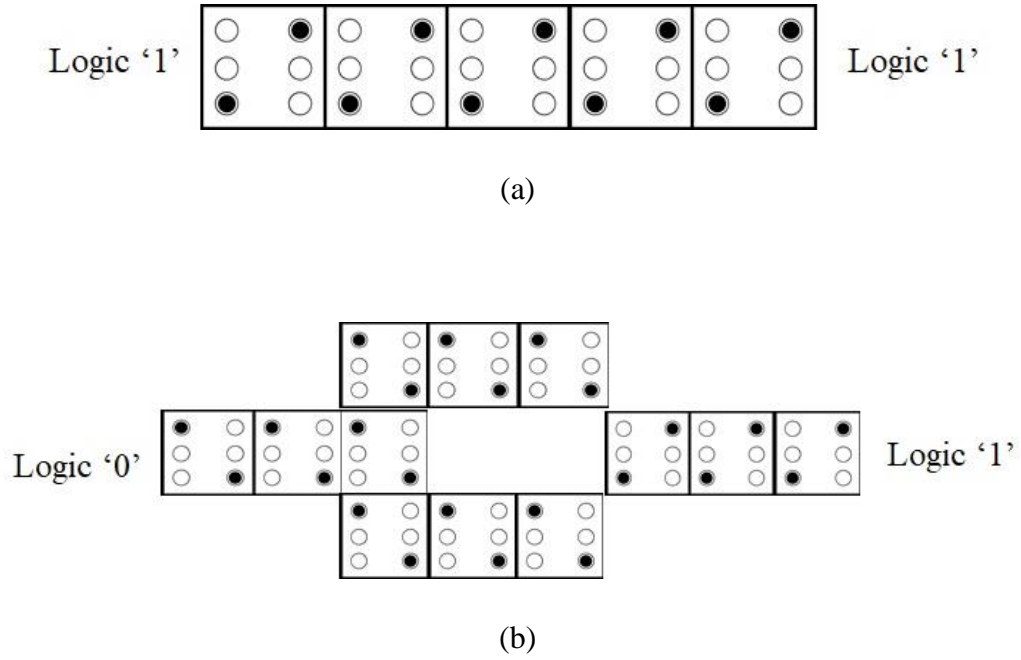
Figure 4 (a) Binary wire based on EQCA. (b) A logical NOT Gate.

One limitation of this form of electronic QCA is controllability of dot size. Experimental demonstrations show that a dot size of ~10 nm is needed to control the electron occupancy [21]. For semiconducting dots, the effects of surface states need to be included in modeling. This can be extremely difficult as surface conditions change based on the quality of fabrication. Also, coherence is maintained with minimal errors below liquid helium temperature and any fluctuation in temperature could result in signal decay.
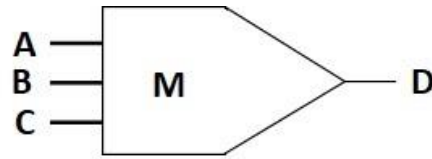
(a) Majority gate circuit schematic
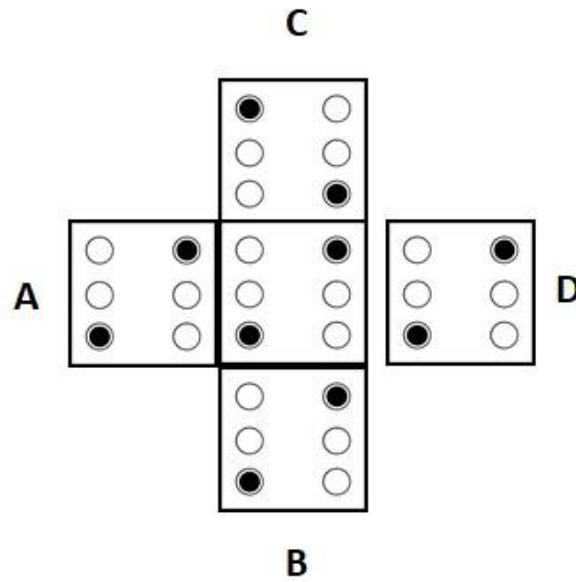
(b) QCA representation

Figure 5 (a) Circuit representation of a majority gate. (b) Equivalent EQCA representation where inputs A and B force the center cell and by extension, output D, into the same polarization regardless of input C.
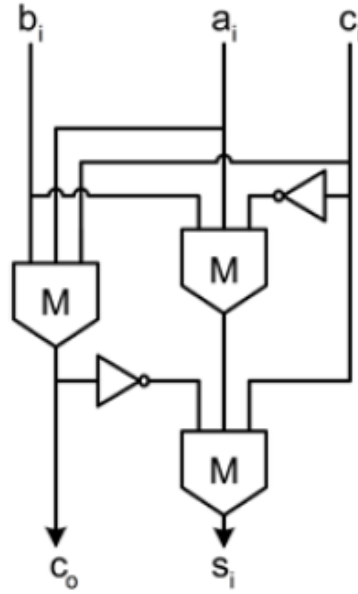
Figure 6 A 1-bit ripple carry adder schematic employing majority gates.

1.4.2   Superconducting QCA (SQCA)

Primarily referring to the Josephson Junction (JJ) as the unit cell, this class of QCA makes use of a superconducting loop of current to represent logic states. Brian Josephson, in 1962, conjectured that pairs of superconducting electrons could tunnel from one superconductor to another through a non-superconducting barrier. This is known as the Josephson Effect, and it is the principle governing the operation of JJ [29]. A typical representation, shown in Figure 7, involves two superconducting electrodes separated by a thin layer known as the 'weak link' across which electrons can quantum mechanically tunnel. The term weak link refers to the low value of the material's critical current in relation to its superconducting neighbors. The critical current, I_C, is the maximum supercurrent that flow through the JJ. In addition to an insulating barrier, further studies have shown that weak links

could be made from a diffusive normal metal, another superconductor, or in some cases, a constriction in thickness between the two superconductors [30,31,32,33].

| Superconductor | Barrier | Superconductor |

Figure 7 Schematic diagram of a Josephson Junction. Barrier could be an insulator, metal, or superconductor with restricted thickness. A common structure is the $Nb/AlO_x/Nb$ tri-layer.

For an insulating barrier, the supercurrent, I_S, flowing across the junction is given by (1.6), where δ is the difference between the phases of the wavefunctions in both superconductors that allows a net current to flow.

$$I_S = I_C \sin(\delta) \tag{1.6}$$

If a bias, V, is applied across the junction, the phase will vary with time giving rise to an alternating current defined in (1.7), where Φ_0 is the quantized magnetic field known as the magnetic flux quantum. It is a constant given by (1.8). In a closed section of a superconductor, the magnetic flux present is discretized by multiples of Φ_0 for h, and e being Planck's constant and the electron charge, respectively.

$$\frac{dI_S}{dt} = \frac{2\pi}{\Phi_0} I_C \cos(\delta)V \tag{1.7}$$

$$\Phi_0 = \frac{h}{2e} \approx 2.07 \times 10^{-5} \, Wb \tag{1.8}$$

This oscillating current is proportional to the applied bias, making the JJ very sensitive to the electromagnetic field [29,33]. For small variations in I_S, this relationship can be thought to describe the non-linear inductor expressed in (1.9), in which degeneracy of the energy levels is restricted to two states.

$$L_J = \frac{dV}{d\left(\frac{dI_s}{dt}\right)} = \frac{\Phi_0}{2\pi I_c \cos(\delta)} \tag{1.9}$$

Unlike EQCA, coupling superconducting qubits is not so straightforward. In the case of Superconducting Quantum Interference Devices (SQUID), Maasen et al., studied the coupling of two radio frequency (rf)-SQUIDs via a third coupler rf-SQUID. This coupler, tunable via an external bias, was passive and in its ground state as to not get entangled with its neighboring qubits [34]. Another study by Blais et al., focused on the coupling of two qubits via a current-biased JJ (CBJJ) implemented with an LC-circuit. In this case, the coupling CBJJ, initially in its ground state, was first tuned to entangle with qubit 1, then qubit 2, and tuned again to entangle with qubit 1. Afterward, the coupler was disentangled from both qubits [35]. In another approach, two qubits were coupled together via a third qubit with higher tunneling energy. Niskanen et al., interpreted this as the direct inductive coupling of qubits 1 and 2 in addition to the non-linear ground state inductance of qubit 3. The application of microwaves through qubit 3 allowed for the modulation of this non-linear inductance, although they mentioned further optimization of this scheme is needed [36].
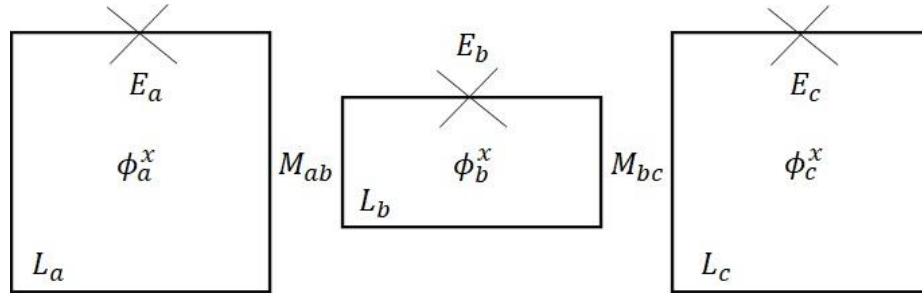
(a)
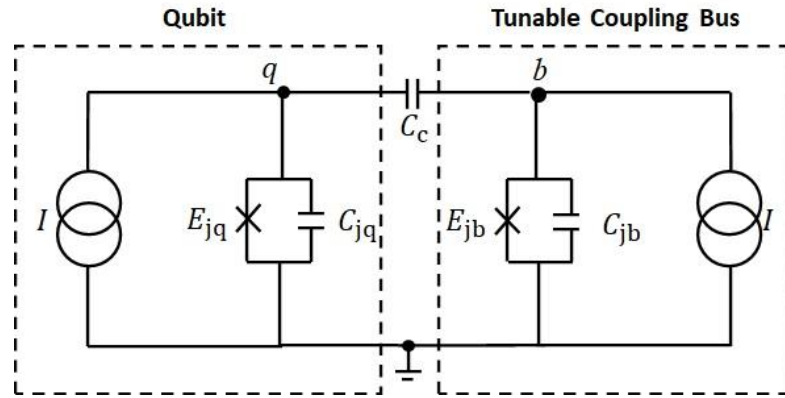
(b)
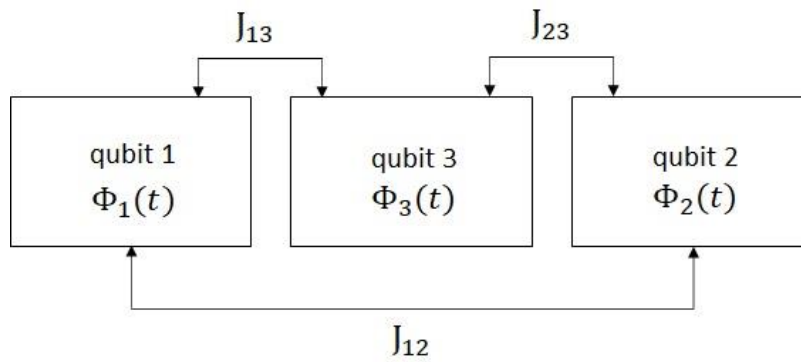
(c)

Figure 8 Schematic representations of different coupling regimes in superconducting QCA. (a) Passive rf-SQUID coupler in its ground state. (b) Current-biased JJ. (c) Inductive coupling of two qubits via a third qubit with higher tunneling energy.

A major limitation of superconducting QCA is their practicality. There are existing implementations of quantum computers that employ them, from IBM's Q System One, to Google's Sycamore, and Dwave Systems' 2000Q [8,14,37,38]. While fabrication of the components is possible with current integrated circuit manufacturing techniques, operation requires cooling to liquid helium temperatures, with a significantly large cooling system, a prospect that would discourage most. And while extremely sensitivity and precise, thermal variations above their critical cooling temperature introduces errors in readout. Robustness of the computer also come into play, as tailoring them to solve large scale problems requires algorithms that can produce high fidelity solutions. Currently, Dwave Systems Inc. (Burnaby, British Colombia, Canada), is the only company in the world with a commercialized product based on SQUID. According to the company, their elements are superconducting Josephson Junctions (JJ) that can be coupled and tuned with an attached inductance. Given the proprietary nature of their product, their method(s) of tuning and the extent to which coupling is controllable is unclear. Nonetheless, the company boasts several customers such as Lockheed Martin, Oak Ridge National Laboratory, and Volkswagen as well as collaborations with the defense industry [37].

A variant of superconducting QCA, bearing similarities to SQUID is the Rapid Single Flux-Quantum (RSFQ). RSFQ are also based on JJ, but, unlike the SQUID where logic states are represented by the direction of the magnetic field, integer multiples of Φ_0 , are used instead [40]. The single flux-quanta result in voltage pulses that can then be read out. Most superconducting QCA prototypes were designed to mimic semiconductor voltage level logic. This runs into the problem of *latching logics* where to avoid errors the time for switching from '1' → '0' is considerably longer than that required for '0' → '1', by a factor of 10^3. This is because, for $-I_c < I < I_c$, there is a superconducting state where voltage across the junction is zero and a resistive state where voltage is non-zero. RSFQ bypasses

this because it uses the inherent Φ_0 property of superconductors that can be finely controlled and tuned, allowing finer control over switching times. They have been implemented in memory devices in destructive and non-destructive read/write schemes. Other devices such as logic gates, shift registers, and digital to analog converters based on RSFQ are also available; a notable supplier being Hypres Inc.

The speed of RSFQ is derived from Φ_0, not from scaling as in conventional MOS. They are therefore desirable because they can overcome the speed saturation that arises with MOS as interconnect schemes grow ever more complicated. They are virtually immune to crosstalk, and more tolerant of thermal fluctuations than their SQUID cousins. One major issue with RSFQ is that it requires high current to power in large scale integration. This is major consideration for dynamic power dissipation, especially when designing clocking schemes [40,41].

<div align="center">(a)</div>
<div align="center">(b)</div>

<div align="center">(c)</div>
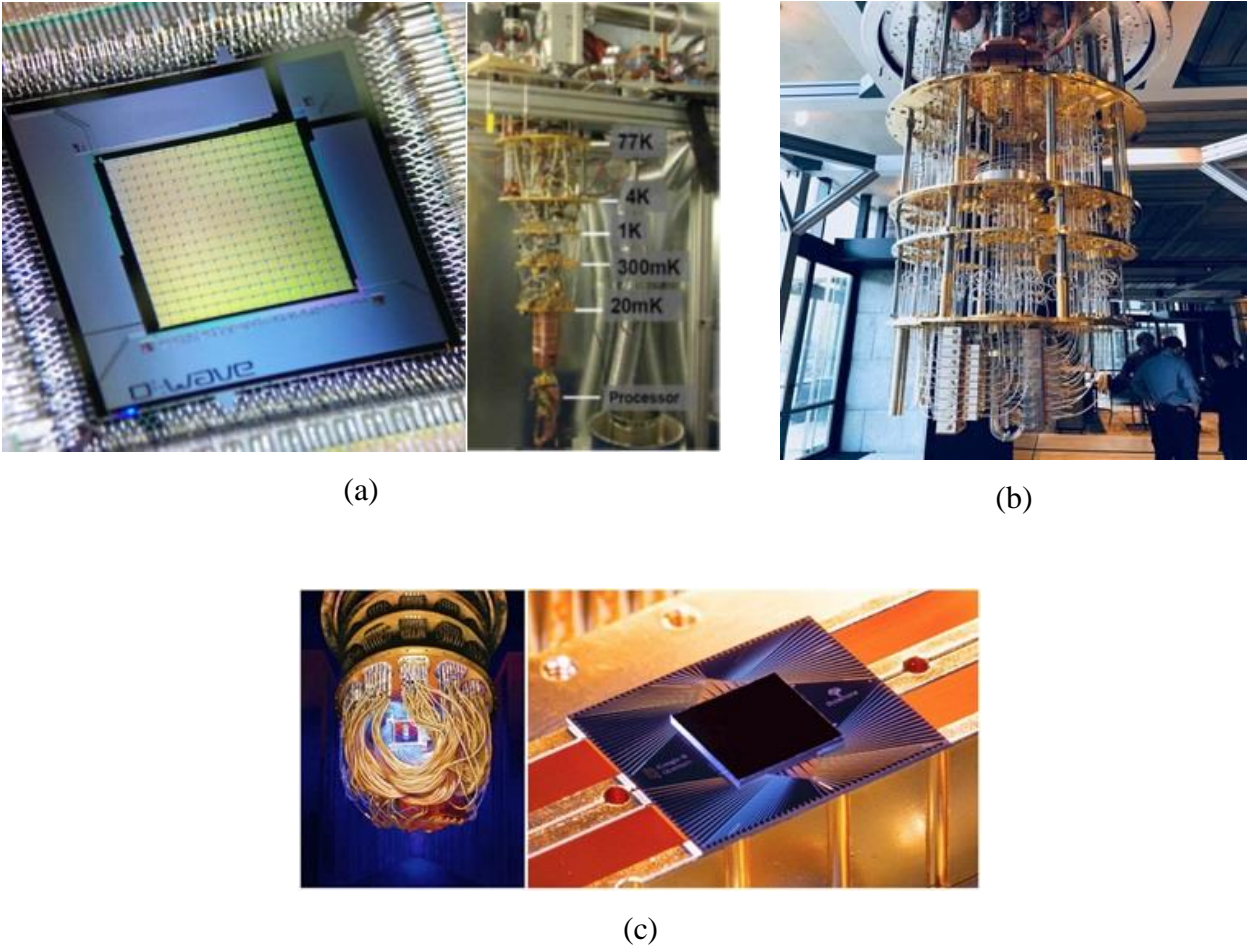
Figure 9 (a) Dwave Systems' 2000Q [37]. (b) IBM's 20-qubit Q System One [38]. (c) Google's 53 qubits Sycamore [39].

1.5   Room Operable QCA

As far as the next generation of computing goes, the holy grail would be a practical demonstration of quantum computing at room temperature. By nature, these QCA elements would have to be extremely robust in weathering thermal fluctuations that could cause decoherence. The quantum effect responsible would have to have much larger ranges than those of the low temperature regime. And the elimination of cooling systems would make any quantum computer based on these economical

viable, not least extremely lucrative. At present, practical demonstrations of these do not exist although there are promising candidates in organic molecules, or thin film magnetic materials.

1.5.1 Molecular QCA

In molecular QCA (MOQCA), bistability is based on charge occupying molecular orbitals. Candidate molecules localize charge to form "dots" in redox centers with connecting ligands acting as the tunneling barrier between. The tunneling of charge from one dot to another on the same molecule facilitates switching between states. In a conceptual two-dot model molecule, the dots are allyl groups on the end of alkane chains. Like EQCA, a clocked model can include a reset state as in Figure 10 where a local perpendicular field switches the molecule. Coulomb interaction allows for coupling between molecules. Figure 11 shows a representation of molecular QCA where two molecules are used to form a cell and the quadrupole moment of one cell switches that of another [19,42]. Again, like EQCA, MOQCA arranged in a linear fashion such as this can be used to realize a wire or a logical NOT gate.

This form of QCA poses several advantages in addition to room temperature operation. Being molecules, uniform fabrication through chemical synthesis is possible and their dimension are within the range of 1 nm. Together with their extremely low power dissipation, this means they can be synthesized in large densities [43]. The tunneling barrier can also be varied meaning charge transfer from one end of a dot to the other can occur on the order of femtoseconds [19]. However, being molecules, anchoring them to the surface of a carrier substrate is necessary, not least for practicality and placing contacts for measurements. Cell size being very close to the dimension individual atoms (~0.3 nm) proves to be a double- edged sword as reliable measurement of switching would require

extremely sensitive device readouts. Self-assembly of the molecules will be necessary as no current lithographic technique is capable of assembling them into the required QCA configuration.

(a)

"0"   "null"   "1"

(b)
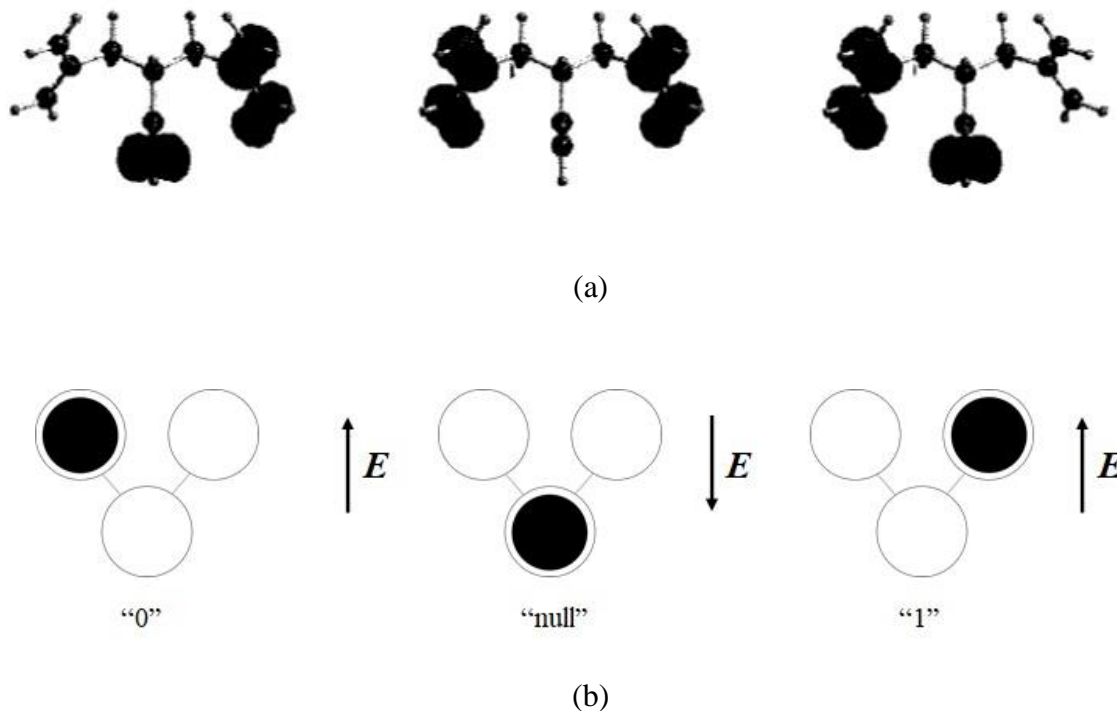
Figure 10 (a) Candidate molecule for MQCA where states are defined by the charge occupancy in different sections. (b) Showing clocked model with null state.

Though no sufficiently explored prototypes exist, suitable candidate molecules have been studied. These include, diallyl-butane where the dots are allyl groups bridged by a butane ligand, and decatriene composed of three ethylene groups in Figure 12 [44]. A practical QCA example was demonstrated using a mixed-valence compound of ruthenium and a ferrocene group by Li et al with

switching behavior of the molecule confirmed via capacitance measurements of the dots. The mixed-valence chemical species offer the advantage of covalent bonding to the usual silicon substrate but come with added counterions that act to maintain charge neutrality of the molecule [45,46]. Using a molecule with localized mobile charges, known as zwitterionic mixed-valence complexes, and incorporating a doping species within it has been proposed as a way to eliminate counterion effects in MOQCA [47].
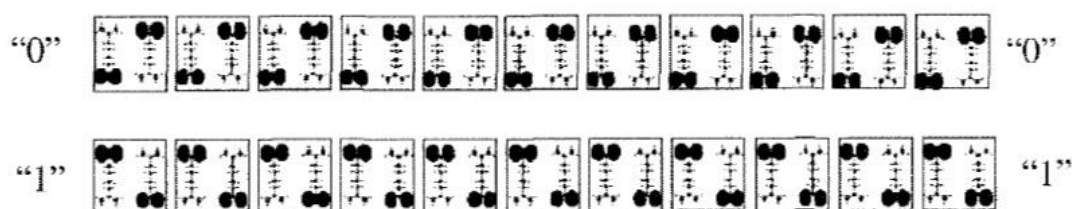
Figure 11 Binary wire based on MOQCA

(a)   (b)
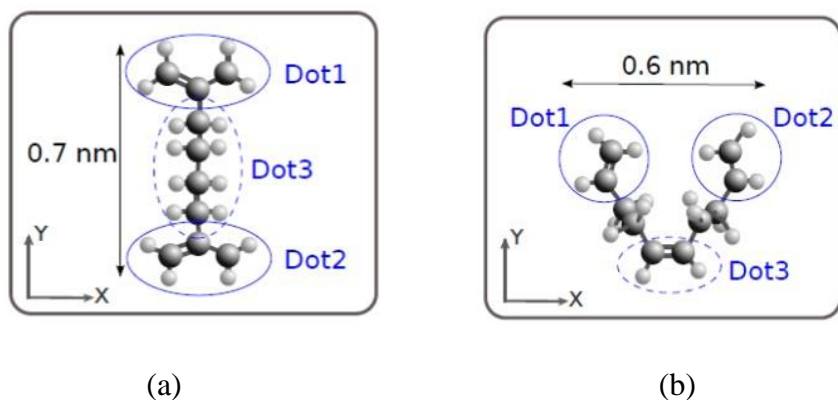
Figure 12 Candidate MOQCAs. (a) Diallyl-butane. Dots are allyl groups with a butane bridge. (b) Decatriene comprising of three ethylene groups *[44]*.

1.5.2   Magnetic QCA (MQCA)

A more promising avenue toward room operable temperature QCAs nanomagnets. Magnetic materials have long since been used as memory storage elements and hard disks [48,49]. As QCAs, magnets are desirable for many reasons. Their small size means they can withstand thermal fluctuations and maintain magnetization for extended periods of time and like MOQCA, power dissipation is extremely low meaning high packing density with operational frequencies in the THz range [19,50]. For this type of QCA, bistability is based on the direction of the collective magnetic moments in the material and is strongly influenced by geometry. These moments align themselves preferentially along the axis that minimizes the magnetostatic energy. For the elongated magnet in Figure 13, this is the 'easy axis' along the y-direction. The x-axis is known as the 'hard-axis', and it is the direction of maximum energy.

(a)   (b)
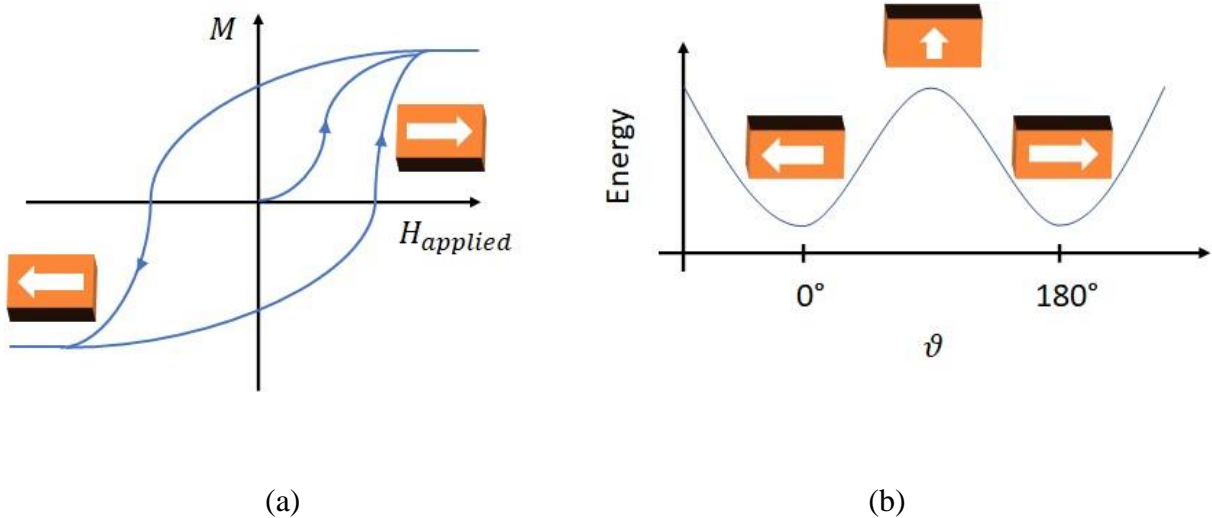
Figure 13 (a) A hysteresis curve of an elongated nanomagnet. (b) Angular dependence of remanent magnetization. Two remanent states are separated by an energy barrier.

Coupling in a series of nanomagnets is due to dipole-dipole interaction. The closure of magnetic flux lines outside the magnets produce stray fields that can interact with one another [50]. The nanomagnets are taken to be single domain meaning the magnetic moments coalesce into a single magnetic domain. They are usually < 1um in size and are chosen to be anisotropic so that they exhibit bistability with the internal field pointing in either of two directions at remanence (zero external field) as shown in Figure 13A [51]. The application of an external field can be used to change the magnetization of one magnet and subsequently, its neighbors. Field-coupled nanomagnets can then be forced into ferromagnetic (all magnetic moments are in parallel) or anti-ferromagnetic (alternating magnetic moments) alignment. These coupled states can remain as such indefinitely since the barrier between the two stable ground states is very high. A representation of a magnetic QCA wire is depicted in Figure 14A, 14B. By fixing the magnetization of the input magnet, a signal can be propagated either by F or AF – coupling down a series of magnets with the limiting factor as to the length of the wire being the short range of the exchange force [48]. Similarly, a majority gate, shown in Figure 14C, is made with an arrangement of magnets such that the output of the system is based on majority magnetization.

(a) Anti-ferromagnetically coupled wire

(b) Ferromagnetically coupled wire
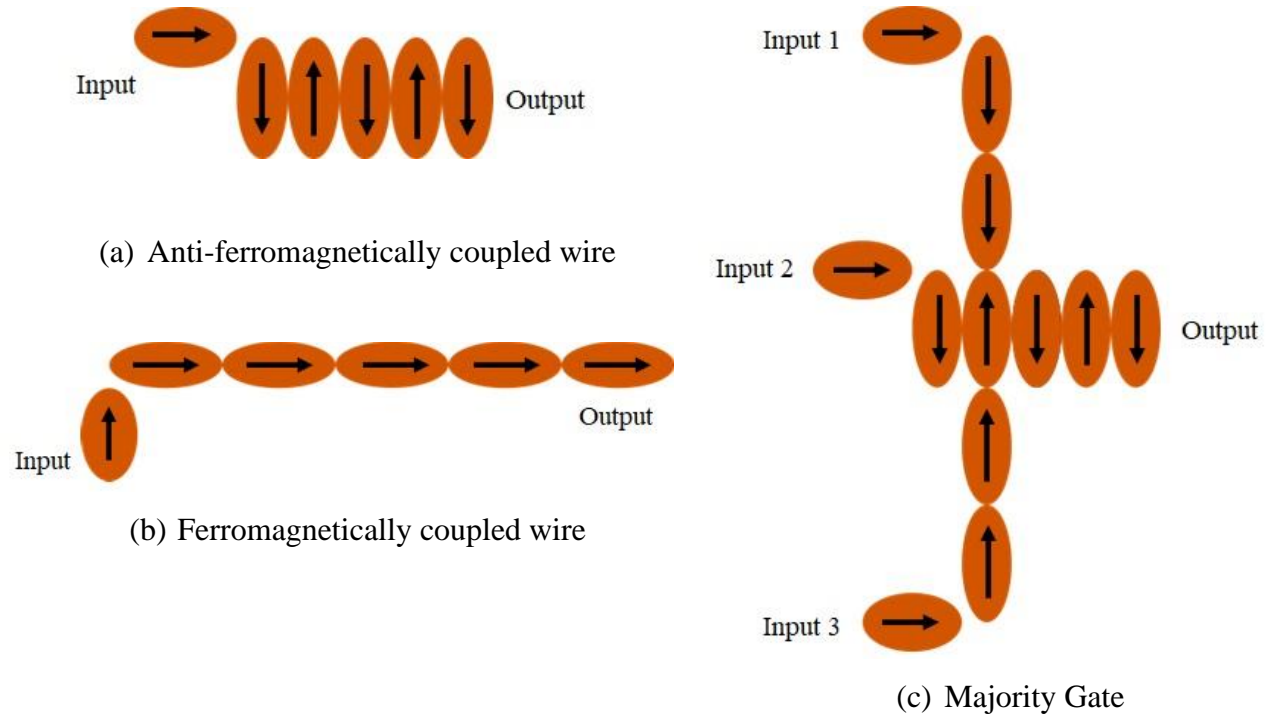
(c) Majority Gate

Figure 14 (a) Antiferromagnetically (AF)-coupled wire, (b) ferromagnetically (F)-coupled wire, and (c) a Majority gate where inputs #1 and #3, are F-coupled and input #2 is AF-coupled.

Other MQCA variants have been proposed. An interesting example was demonstrated by Allwood et al. [52]. In their work, they exploit the magnetic domains within planar nanowires of Permalloy to perform logic operations. By growing the wire to include forks and twists, domains can split/merge, or change direction along the wire. Picking outputs at particular locations give results of the desired logic function. Another is the use of multi-layer magnets as in Figure 15A [53]. A 'reference' or 'fixed layer' by virtue of its parameters during fabrication is made to have magnetization that does not change easily. It is separated from a 'free layer' by a non-magnetic material or tunnel junction. The free layer is so named because its magnetization can freely switch. The fixed layer transfers angular momentum to the free layer through the spins of tunneling electrons in what is known as spin-torque

transfer (STT) [53,54]. The passing of current through adjacent metal contacts serves to switch the magnetization of the fixed layer and by extension the free layer. Neighbor interactions between cells is then used to for computation. This current is no large enough to change magnetization of the fixed layer. This STT method is suitable for reducing the power dissipation because the current required is less than that needed to generate the fields for switching in nanomagnets.

Thin film nanomagnetic disks, circular rings, and square rings have been also been studied and demonstrated [55,56,57,58,59,60]. In these, bistability is represented by the direction of rotation of the magnetization at remanence. A logical '1' can be represented by clockwise chirality while a logical '0', by counter-clockwise chirality with reset being the superposition of the bi-stable states. As a result of flux closure, the magnetization in these geometries form closed loop vortices that rotate in-plane. Coupling can be achieved through the interaction of the out-of-plane component of the magnetization or by putting the elements in close contact and allowing the local quantum exchange force to align neighbor magnetic spins. The focus of this work will be on circular magnetic disks and rings.

(a)

(b)
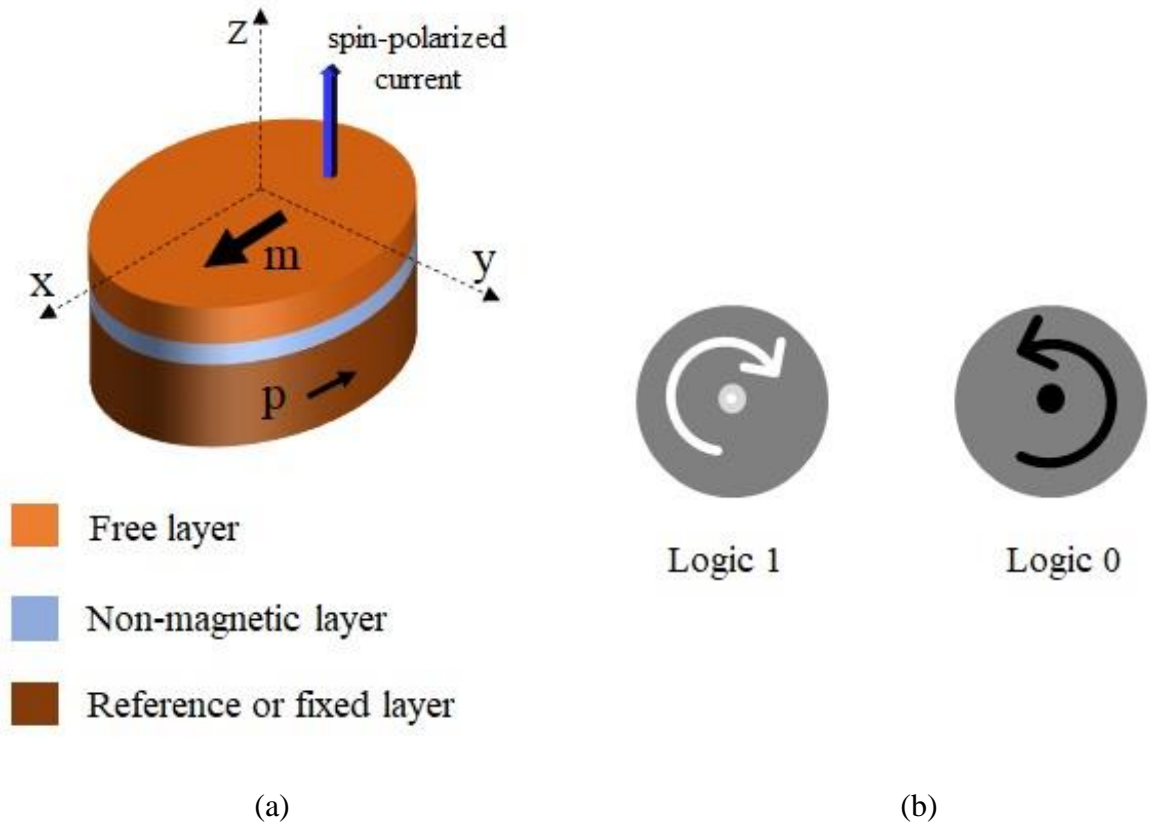
Figure 15 (a) Tri-layer structure employing spin transfer torque. (b) Nanomagnetic disks. The white and black dots in the middle of the disks are the out-of-plane component of the magnetization.

II.   The Micro-magnetic Model

The open source Object Oriented Micro-Magnetic Framework (OOMMF) from the National Institute of Standards and Technology (NIST), an entity of the U.S. Department of Commerce, was used to simulate the elements in this work [61]. The fundamental principles used in the simulation solver are based on the Landau-Lifshitz-Gilbert equation (LLG).

2.1   Landau-Lifshitz-Gilbert Equation

In 1935, Lev Landau and Evgeniy Lifshitz introduced a semiclassical model to describe the precessional motion of magnetic moments within ferromagnetic media [62]. The time dependent partial differential equation in (2.1) models the magnetization which is assumed to be a continuous vector field whose state depends on internal interactions as well as interaction with an applied field. The parameter γ_{LL}, is the Landau-Lifshitz gyromagnetic ratio of magnetic moments to the spin angular momentum while H_{eff} is the effective field, α, the damping factor, and M and M_s, the magnetization and saturation magnetization respectively.

$$\frac{dM}{dt} = -\gamma_{LL}M \times H_{eff} - \frac{\gamma_{LL}\alpha}{M_s}M \times (M \times H_{eff}) \tag{2.1}$$

Thomas Gilbert's contribution in 1955, a was to include a better description of the damping mechanisms which lead to energy losses within microscopic ferromagnetic media [63,64,65]. In (2.2), this is seen as the inclusion of γ_G which is the Gilbert gyromagnetic ratio that is given by (2.3).

$$\frac{dM}{dt} = -\frac{\gamma_G}{(1+\alpha^2)}M \times H_{eff} - \frac{\gamma_G\alpha}{M_s(1+\alpha^2)}M \times (M \times H_{eff}) \tag{2.2}$$

28

$$\gamma_G = (1 + \alpha^2) \times \gamma_{LL} \qquad\qquad (2.3)$$
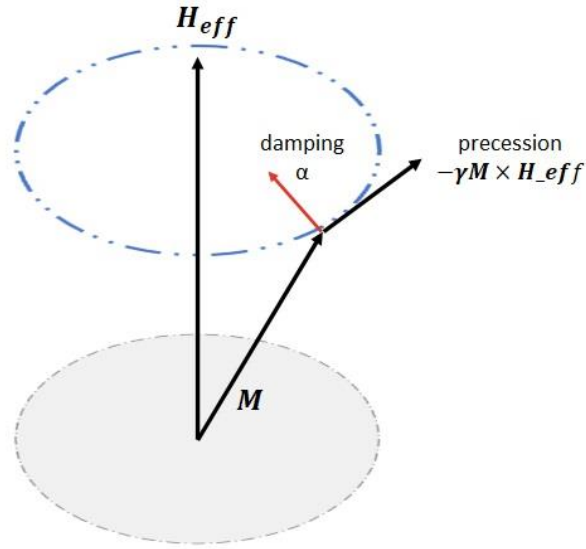
Figure 16 Gyromagnetic precession with damping action.

Mathematically, both (3.1) and (3.2) are identical provided (3.3). However, this addition by Gilbert says that $dM/dt \rightarrow 0$ as the damping factor, $\alpha \rightarrow \infty$. It is in contrast to the Landau-Lifshitz version which says the $dM/dt \rightarrow \infty$ for the same condition for α. As a dimensionless factor, α, models the dissipative forces the magnetic moments experience as they precess about the effective field. It is primarily responsible for transfer of angular momentum to the crystal lattice [65]. The Gilbert addition therefore makes physical sense since a large damping factor should eventually cause a system's magnetic moments line up along H_{eff} as it tends to equilibrium as in Figure 16. Experimentally, α, has been determined to be $\ll 1$ [66,67,68].

2.2   Micro-magnetic Free energy

The effective field, H_{eff}, is the summation of the contributions of five domain energy terms that determine magnetization within ferromagnetic media. These are the quantum exchange, anisotropy, the magnetostatic or demagnetization energy, the Zeeman energy, and the magnetoelastic energy [68,69].

2.2.1   Quantum Exchange Energy

The quantum exchange energy describes the interaction between neighboring spins in a crystal lattice [69]. It is heavily involved in the formation of magnetic domains within a ferromagnetic body and is given by

$$E_E = -J \sum_{\langle i,j \rangle} \vec{S_\iota} \vec{S_J} \tag{2.4}$$

where the $\vec{S_\iota} \vec{S_J}$ denote the spins of nearest neighbors and J is the exchange integral between them. Since electrons with the same spin cannot occupy the same quantum state by the Pauli Exclusion principle, exchange interactions between them must give the same energy density, meaning their wavefunctions, $\psi_1(\vec{r})$ and $\psi_2(\vec{r})$ must be antisymmetric [70]. These Heisenberg interactions occur over the volume of the media in play and is represented the Hamiltonian operator in the

$$J = \int \psi_1^*(\vec{r}) \psi_2^*(\vec{r}) H(\vec{r}) \psi_1(\vec{r}) \psi_2(\vec{r}) \, dr^3 d^3r \tag{2.5}$$

integral. For $J > 0$, ferromagnetic interactions occur with spins in parallel while $J < 0$ indicates antiferromagnetic interaction with antiparallel spins.

In the micromagnetic model, the exchange is introduced as the interactions over an isotropic lattice and is given by a gradient of the reduced magnetization, $m = M/M_s$, in (3.6). The exchange

constant, A, expressed by (2.7), depends on S^2, the spin magnitude, Z_c, the number of atoms per unit cell, and a_0, the lattice constant. In this work, we will consider the exchange interactions to be of uniform distribution.

$$E_E = A \int \left[\left(\frac{\partial \, m}{\partial x} \right)^2 + \left(\frac{\partial \, m}{\partial y} \right)^2 + \left(\frac{\partial \, m}{\partial z} \right)^2 \right] dV \tag{2.6}$$

$$A = \frac{JS^2 Z_c}{a_0} \tag{2.7}$$

2.2.2   Magneto-crystalline Anisotropy

The easy axis mentioned in 1.4.2 manifests itself in ferromagnetic materials because of the anisotropic effects that can come from the lattice structure [70]. In most materials, one can see this as a principal axis (es) that is energetically favorable in-situ material synthesis or ex-situ conditions. Taking the anisotropy energy density in a volume and integrating with help of spherical coordinates, we have

$$F_{an}(m) = \int_{\Omega} f_{an}(m) \, dV. \tag{2.8}$$

A profile of this density can be seen in Figure 13B. The minima and maxima of the energy profile correspond respectively to the easy and hard axes of the elongated nanomagnet in the absence of an external field. In Permalloy, this translates to uniaxial anisotropy, the existence of only one easy axis [71]. If we take this axis as the out-of-plane z axis, the uniaxial anisotropy can be, in truncated form, written as

$$f_{an}(m) = K_0 + K_1 \sin^2 \theta \tag{2.9}$$

where K_0 and K_1 refer to anisotropy constants which units of J/m^3. In this work, most elements simulated were symmetric, so uniaxial anisotropy was considered to be negligible and was set to zero in the simulation code in the appendix [57].

2.2.3 Magnetostatic Energy

This expresses the non-local interactions of the magnetic moments over the ferromagnetic volume [67]. In thin film magnets, this mostly represented by the out-of-plane component of the magnetization. By Maxwell's equations for magnetized bodies, we know

$$
\left\{
\begin{array}{ll}
\nabla \cdot H_m = -\nabla \cdot M & \text{in } \Omega \\
\nabla \cdot H_m = 0 & elsewhere \\
\nabla \times H_m = 0 &
\end{array}
\right. \tag{2.10}
$$

for

$$
H_m = \frac{B_m}{\mu_0} - M \tag{2.11}
$$

where H_m, is the magnetostatic field which depends on contribution from all magnetic moments and B_m, the magnetostatic flux density. The energy density of H_m can be written as in (2.12). Substituting (2.11) into (2.12) leads to (2.13).

$$
U_m = \frac{1}{2} \int_\Omega \mu_0 H_m^2 \, dV \tag{2.12}
$$

$$
F_m = -\frac{1}{2} \int_\Omega \mu_0 H_m \cdot \left(\frac{B_m}{\mu_0} - M \right) dV. \tag{2.13}
$$

Owing to the orthogonality of H_m and B_m over the integral space, we can discard the first part of (2.13) and write the magnetostatic energy as

$$F_m = -\frac{1}{2} \int_\Omega \mu_0 M \cdot H_m \ dV \tag{2.14}$$

2.2.4 Zeeman Energy

The Zeeman energy is the contribution of the applied magnetic field to the magnetization over a volume [66,67]. It includes the magnetic permeability, μ_0, and H_{app}, the applied field.

$$E_z = - \int \mu_0 M H_{app} \ dV \tag{2.15}$$

2.2.5 Magnetoelastic Energy

This energy term comes from stresses that build up in response to mechanical deformation of ferromagnets [67]. For the thickness of 25 nm of Permalloy used in our simulations, it is reasonable to consider the contributions of magnetoelasticity to be negligible.

2.2.6 Free Energy Functional

The summation of the energy terms from (2.6), (2.9), (2.14), and (2.15) gives the micro-magnetic free energy functional in its normalized form in (2.16) [67].

$$E\left(M, H_{app}\right) = \int_\Omega \left[A(\nabla m)^2 + f_{ani} - \frac{1}{2}\mu_0 M \cdot H_m - \mu_0 M \cdot H_{app} \right] dV \tag{2.16}$$

2.2.7 Effectiveness of Micro-magnetics

Micro-magnetic simulations can often result in complex equations that become intractable; hence its applicability is only to length-scales of hundreds of nanometers to several micrometers. The former being a lower bound imposed by the non-idealities of real materials, the latter, an upper bound

imposed by the availability of computing memory. In fact, it is not uncommon for OOMMF simulation time to run into several days, or to encounter errors as a result of insufficient memory. The simulations featured in this work were performed subject to the computational capacity at hand at the time.

For the benefits that micro-magnetics offer, it is not without its limitations. For instance, the micro-magnetic solver used in this work does not account for temperature effects [61]. In other words, the solver operates based on the assumption that temperature is at $0°$ K. To account for realistic applications this would need to be considered, though our results show reasonable agreement with already published experimental data [57,72]. Secondly, the elements simulated were uniform in shape which is not always possible with available deposition techniques. A slightly off-axis deposition in an electron-beam evaporator, for example is enough to introduce size disparities, and that is not considering the difficulty of lift-off methods used for the thicknesses in question. Lastly, it is difficult to account for thin film defects that could possibly leads to different magnetization dynamics [73,74].

III.   Magnetic Domain Theory

In ferromagnetic media, magnetic moments tend to align themselves into regions of uniform magnetization known as domains in Figure 17A. The boundary of these domains known as domain walls and they tend to be few nanometers thick. For macroscale magnets where long range crystalline order is not present, these domains tend to align along a locally preferred axis that can be influenced by structural defects or macroscopic grains. These are known as multi-domain or '*hard*' magnets. The formation and ordering of domains in these magnets come from balancing the short-range quantum exchange energy and anisotropy energy. Here, magnetization reversal happens through the motion of domain walls. Interactions can occur between walls coming together and forming a larger wall. Walls can be pinned at defect sites due to the anisotropy introduce there. They can also form around these pinning sites and go on to dominate the domain structure of the specimen. The '*coercivity*' is the deviation from zero field along the x-axis of the hysteresis loop of Figure 13A. It is essentially a memory of the previous magnetization order. In the presence of a high enough field, the magnetic moments all align along the direction of the field but return to their locally preferred order once it is removed [70].

As the size of the magnet shrinks, the thermal energy, which is proportional to the magnet's volume, competes with the quantum exchange energy and long-range demagnetization energy causing the coercivity to decrease, as fewer domains form [49,51,66,75]. Commonly observed in thin film, or 'soft' magnets, exchange effectively tries to force the magnetization out-of-plane to reduce its energy, while demagnetization tries to force it in-plane to reduce surface charges. The decrease in coercivity would enable switching to happen easily since only a few magnetic moments have to be flipped. However, it is being suggested that coercivity can actually increase below a critical size as the magnet

approaches what is known as '*single-domain*' status in Figure 17B. As the name suggests, this is where

no domain wall exists, and magnetization reversal occurs through uniform rotation of parallel spins at

zero field or in the presence of an applied field. This critical size varies for different materials but was

found to be ~ 1 µm for spherical iron oxide particles [51,76,77].

(a)   (b)
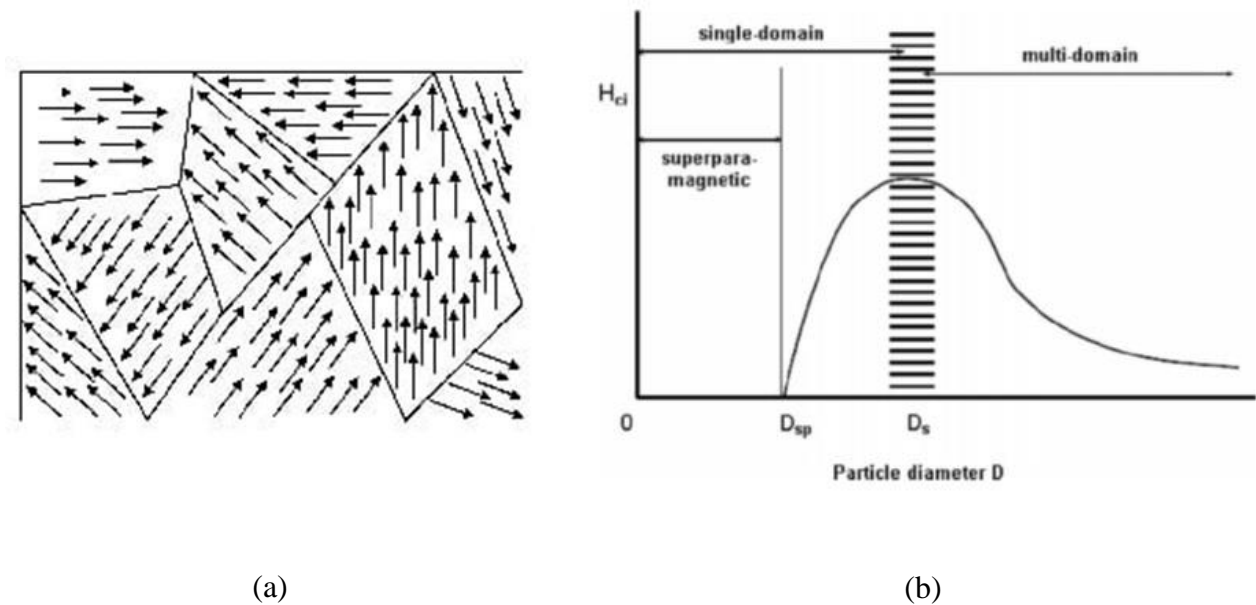
Figure 17 (a) Multi-domain magnet. (b) Intrinsic coercivity vs particle size [51].

3.1   Bloch Wall

Domains of various types form in magnetic media. One simple variation the 180° Bloch wall,

named for the German physicist, Felix Bloch. In this case, the sample's magnetization rotates in the

plane of the wall. In Figure 18 and Figure 19, as the magnetization rotates, no demagnetizing field

exists within the wall since $\nabla \cdot \boldsymbol{M} = 0$. Also, there is no magnetization component pointing along the x-axis and the spins in the y-z plane are in parallel to one another [70].
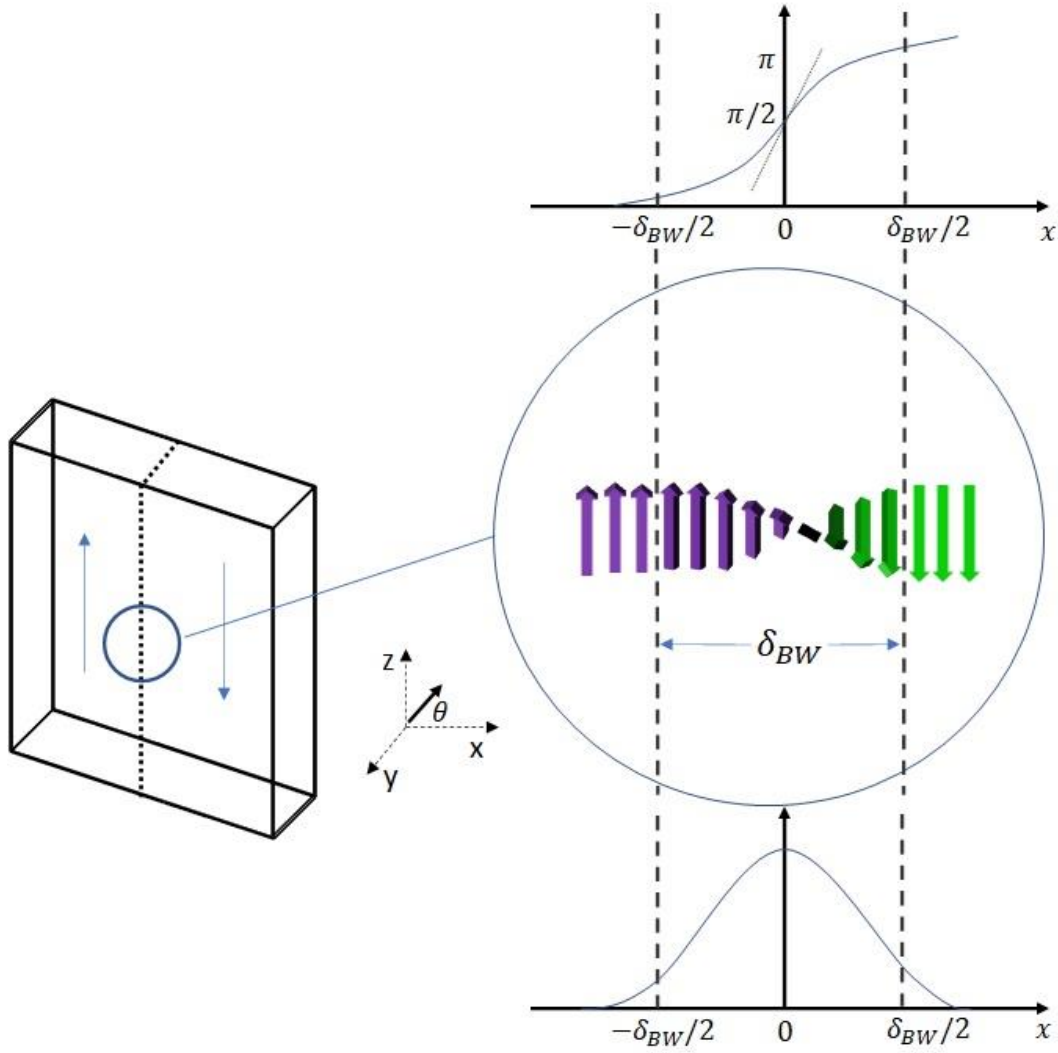
Figure 18 Detailed representation of a 180° Bloch Wall.
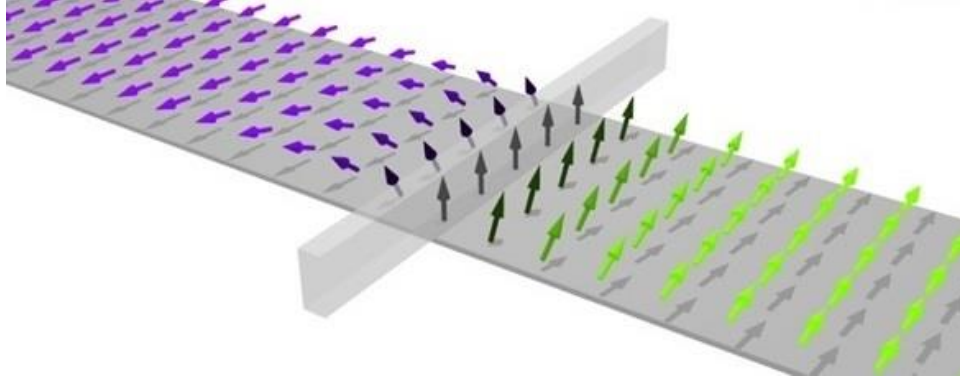
Figure 19 A conceptual visualization showing rotation in the wall plane *[66]*.

Finding an expression for the Bloch wall involves neglecting the demagnetizing energy at the surface and considering only the exchange energy in the x-direction and the second term of the anisotropy energy in (2.6) and (2.9) respectively. With this, it is clear that Bloch walls are prevalent in magnets with sufficient thickness that surface conditions can be neglected. If we consider the wall diameter to be from where rotation of moments begins to where it ends, we have

$$E_{Bloch} = E_{E_x} + E_{ani} = \int A \left(\frac{\partial \theta}{\partial x} \right)^2 + K_u \sin^2 \theta \ dx \qquad (3.1)$$

Here K_u, is the positive uniaxial anisotropy constant, leading to $\theta = 0$, and $\theta = \pi$ being equivalent rotational axes along which θ changes. Thanks to Euler, we have the property:

$$\int F[x, \theta(x), \theta'(x)] \, dx = \frac{\partial F}{\partial \theta} - \frac{\partial F}{\partial \theta'} \left(\frac{d}{dx} \right) = 0 \qquad (3.2)$$

And provided that $\theta' = d\theta/dx$, this reduces 3.1 to:

$$\frac{\partial (K_u \sin^2 \theta)}{\partial \theta} - \frac{2A \partial^2 \theta}{\partial x^2} = 0 \qquad (3.3)$$

The anisotropy term can be written to equal the product of the exchange constant and the square partial derivate of θ with respect to x giving (3.4) and (3.5)

$$K_u \sin^2 \theta = A \left(\frac{\partial \theta}{\partial x}\right)^2 \tag{3.4}$$

$$\frac{\partial \theta}{\partial x} = \sqrt{\frac{K_u}{A}} (\sin \theta) \tag{3.5}$$

While domain wall width, δ_{BW}, is not a precisely defined parameter because magnetization asymptotically approaches $\theta = 0$, or $\theta = \pi$, it can be extrapolated by a tangent at the origin where the wall center is located at $\theta = \pi/2$. The domain wall equation itself can then be expressed as (3.6), leading to the width being expressed as (3.7) [70].

$$x = \sqrt{\frac{A}{K_u}} \ln\left[\tan\frac{\theta}{2}\right] \tag{3.6}$$

$$\delta_{BW} = \pi \sqrt{\frac{A}{K_u}} \tag{3.7}$$

It is important to note that other definitions of δ_{BW} exist and they can result in slightly different derivations of (3.6) and (3.7). Also, had K_u been taken to be negative, the domain wall width would be infinite since the wall would lie in the $\theta = \pi/2$ plane. Hence, it is necessary to consider K_u as a non-negative parameter in order to ensure a realistic finite wall width.

3.2 Néel Wall

Another type of domain wall is the Néel wall, named for the French physicist, Louis Néel. These are common in soft magnets where the competition is primarily between the exchange energy

and the demagnetization energy. Practically, Néel walls are made of stripes of Néel lines, which are stable surface defects between Bloch wall segments where rotation is in the plane of the domain magnetization. In other words, here, the sample's magnetization rotates perpendicular to the plane of the wall as in Figure 20 and Figure 21. Néel walls have higher energy than their Bloch counterparts because $\nabla \cdot \boldsymbol{M} \neq 0$, meaning there is demagnetizing field present [66,70,75]. A similar derivation as above for the Néel wall width leads to

$$\delta_{NW} = 3\sqrt{\frac{A}{K_d}} \tag{3.8}$$

where $K_d = (\mu_0/2)M_s^2$ [78]. The thickness at which the type of wall crosses from being of Bloch to Néel is estimated to be about 60 nm in Permalloy, the material studied in this work.
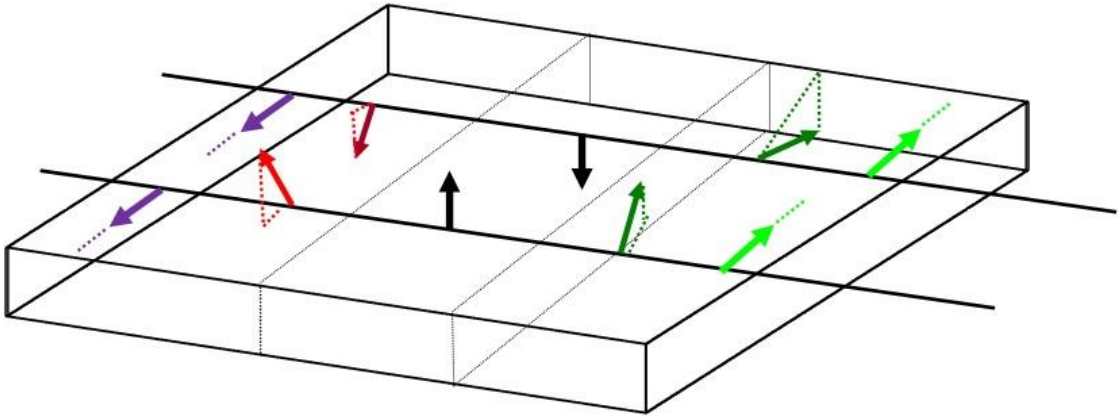
Figure 20 Detailed representation of a 180° Néel Wall.
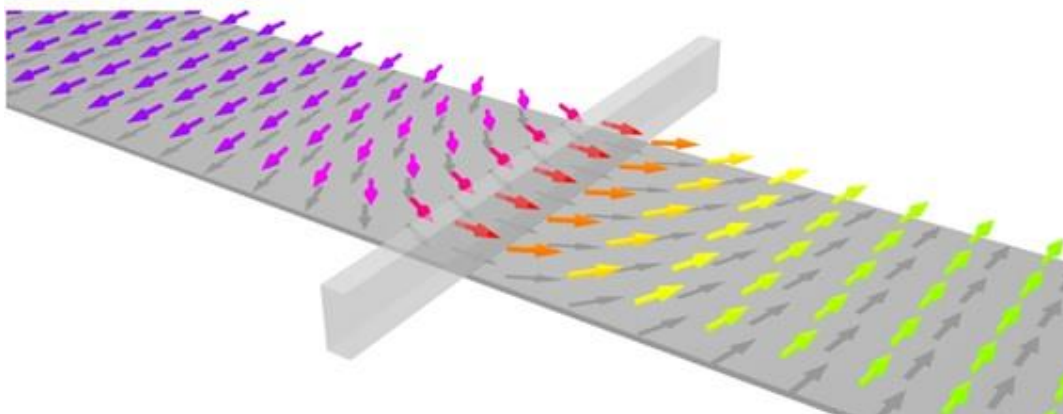
Figure 21 A conceptual Néel wall visualization showing rotation perpendicular to the plane of the wall *[66]*.

Two variants of a Néel wall are shown in Figure 22 [54,56,74,77]. The first in Figure 22A is known as a transverse wall where magnetic moments orient themselves in either head-to-head or tail-to-tail fashion. In this case, the thermal energy of the sample dominates the magnetization process, usually because the sample's volume is reduced. The second variant in Figure 22B is known as the vortex wall, where reversal occurs through an intermediate state called a '*vortex state*.' In this '*curling mode*', the magnetization vectors curl in a bid to minimize the demagnetizing field, at the expense of the exchange energy. Spins are not always parallel to one another during the reversal process [75].

Factors such as geometry, size, and thickness, amongst others play a role in deciding which of these modes dominates [72,79,80]. The vortex is the lowest energy state, meaning it is energetically favorable to form one provided the sample is larger than the coherence radius for transverse walls. Practically speaking, a thin-film magnet that is large enough will see magnetization reversal through the vortex state, while one straddling the border between the few and single-domain regimes will see a

mixture of transverse and vortex domains walls. Once in the single-domain regime, transverse walls only form, increasing coercivity [51]. This was observed in our simulations.
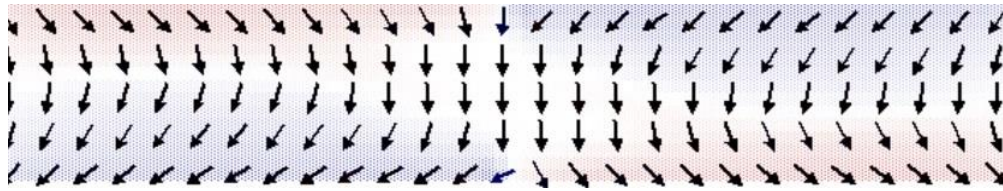
(a)
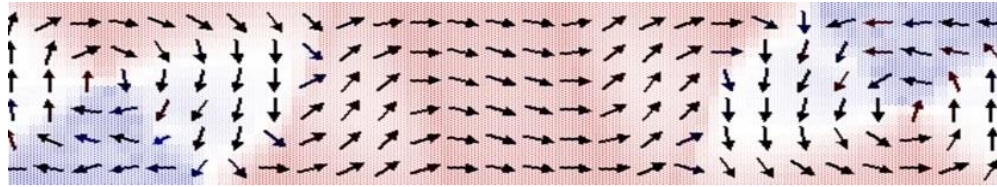
(b)

Figure 22 (a) Transverse type domain wall. (b) Vortex type domain wall.

3.3   Domain Wall Motion

In magnetic media, domain wall motion is the primary phenomenon responsible for magnetization reversal. Commonly, external magnetic fields produced by applied currents are used to enable this process in applications were magnetic recording media are present. Another way is the use of spin-polarized currents as discussed in section 1.5.2. In this scope of this work, the motion, and annihilation of vortex domain walls is the dominant process by which reversal happens [67].

For soft magnets such the ones studied herein, an off-axis field imparts a torque that induces precession of the magnetic moments, eventually pushing the magnetization out of the plane of the sample. The result is a demagnetizing field [70,75]. As this applied field is removed, vortex domain walls form, move perpendicular to the direction of the applied, and annihilate after coming together. The dissipative forces modeled by the damping factor, α, from the LLG equation plays a role in this secondary stage as the magnetic moments approach a minimum in the free energy functional of (2.16). To repeat the reversal process, the only way is to drive the vortex core in the sample to saturation.

IV. Simulation Dynamics

(Partially published as Durowade, T. and Metlushko, V., (2020) Micro-magnetic simulations of correlated switching in touching circular nano-magnetic elements', AIP Adv., vol. 10, no. 3.)

Currently, common measurements techniques like Magnetic Force Microscopy or Scanning Hall Probe Microscopy are capable of imaging magnetic samples but they are limited to zero field measurements. In the case of MFM, the tip-sample interaction can potentially change the magnetization state of the sample itself [81]. An in-field technique like Lorentz Microscopy is not ideal either since repeatable measurements are difficult to obtain due to the shifting electron beam. These methods also only offer spatial resolution analysis. They do not possess the temporal resolution necessary to capture the dynamics of magnetization reversal on the order of picoseconds. On the other hand, temporal techniques like the Magneto-optic Kerr Effect lack the necessary spatial resolution. Hence, simulations are done to bridge the gap by providing an understanding on the formation, motion, and annihilation of the domain walls that enable the switching processes itself [82].

Elements simulated in OOMMF were of diameter and thickness 400 nm and 25 nm, respectively. A mesh discretization was imposed, determined by the magneto-static exchange length, l_{ex}, given in (4.1). The exchange length is a metric of the how strongly the exchange and demagnetizing energies interact. It effectively determines the width of transition between magnetic domains [78]. The mesh needs to be smaller than l_{ex} to capture the intricate details of the switching process. The exchange constant, and the saturation magnetization were chosen as $A = 13 \times 10^{-12} \, J/m$, and $M_s = 860 \times 10^3 \, A/m$, respectively based on literature values for Permalloy, leading to $l_{ex} = 5.28 \, nm$ [83]. Due to memory constraints, and to reduce demand on available computing capabilities, individual and two-elements simulations were at {5 nm, 5 nm, 25 nm} mesh. All others were at {5 nm, 5 nm, 5 nm}

mesh. We do not believe this change in the z-axis mesh affected the results of the smaller simulations for reasons discussed in section 2.3.

$$l_{ex} = \sqrt{\frac{2A}{\mu_0 M_s^2}}$$

(4.1)

4.1   Disks

A symmetric disk, 400 nm in diameter was simulated by initially driving it to saturation with an off-axis field of 2°. This field is off-axis as per the recommendation of the OOMMF creators, to avoid the simulation getting trapped in symmetry induced saddle-points that could result numerical instabilities (Donahue, 2019, personal communication). Depicted in Figure 23A, 23C, as the field is reduced to zero, two domain walls form at the edges and migrate toward one another. They migrate perpendicular to the direction of the applied field with one eventually swallowing the other and leaving behind a vortex core at the center of the disk. The disk settles into this symmetric vortex state at remanence due to flux closure, as the rotating field lines aligning themselves to form a closed loop within the material to minimize the demagnetization energy. The probability of a clockwise or anti-clockwise chirality at remanence is equal [83,84]. The stray out-of-plane component of the vortex core, also known as the demagnetizing field, then rotates in-plane until it finally settles in the disk center at the geometric center as in Figure 23E. As seen in the hysteresis loop of Figure 23F, the vortex forms at zero field, meaning switching is adiabatic. The reversal process from Figure 23C, 23D happens by increasing the field, corresponding to the part of the hysteresis along the x-axis near zero, as the vortex core moves toward the edge of the disk and is pinned there [85]. Further increasing the field beyond saturation, the vortex annihilates resulting the second jump in the hysteresis which is annotated in Figure 23F.

(a)

(b)

(c)

(d)

(e)

(f)
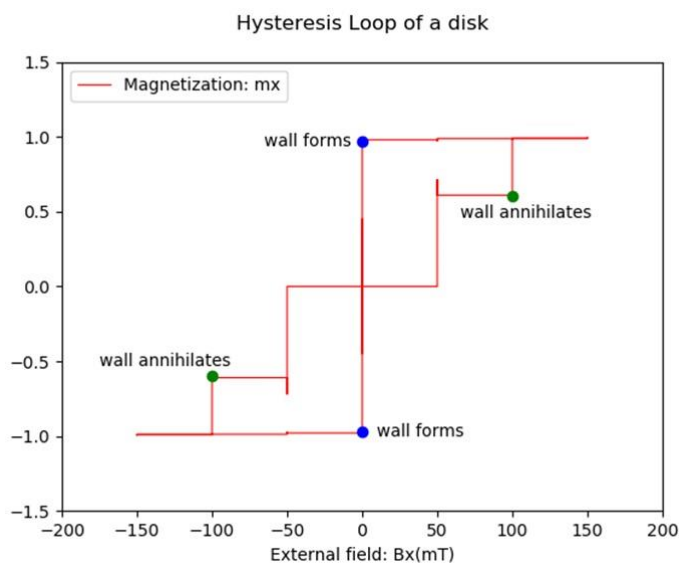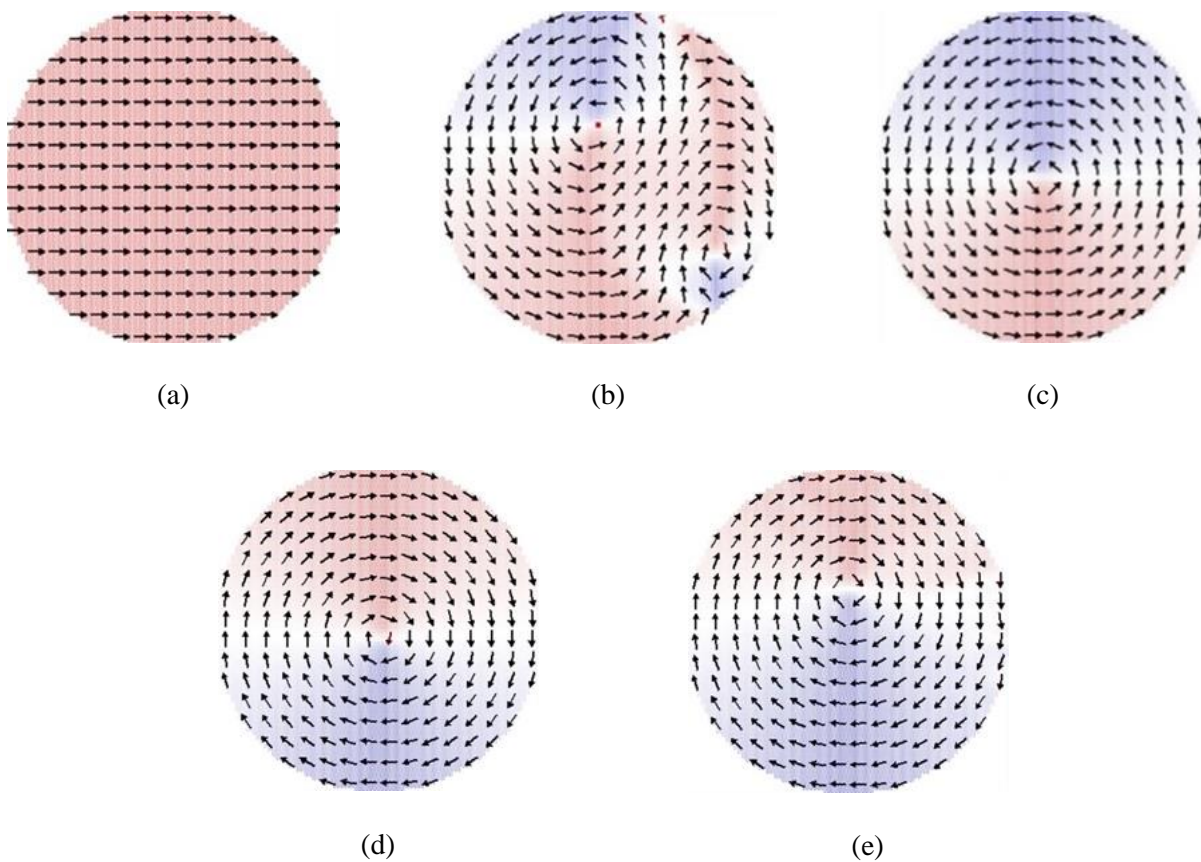
Figure 23 (a) Saturation, (b) domain walls, (c-d) vortex states (e) residual rotation of the vortex core. (f) Hysteresis loop of symmetric 400nm disk. Extra steps from wall annihilation at saturation [85].

(a)   (b)
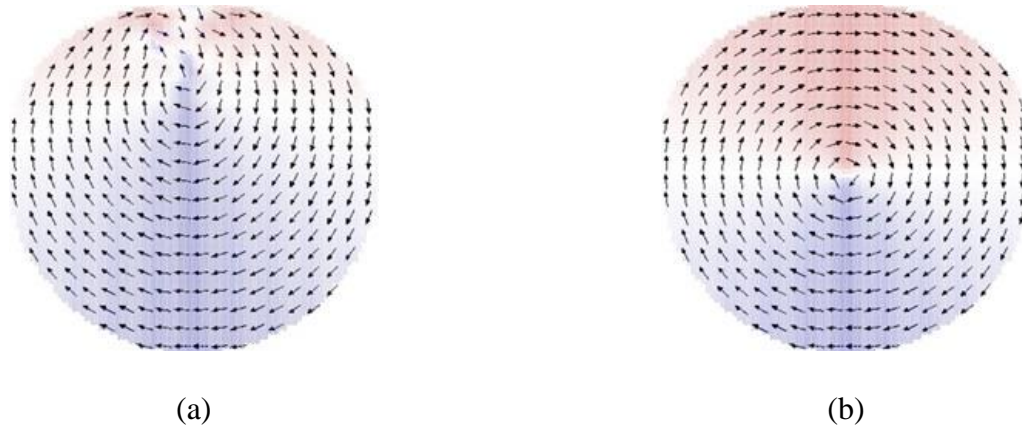
Figure 24 (a) Domain wall and (b) vortex state of a of deformed disk. The deformation is a slightly flattening of the top of the disk

The introduction of asymmetry in the form a 30 nm flattening of a portion of the disk as in Figure 24A results in a completely different switching process from that of the symmetric disk. In this case, the vortex evolves through the formation of a single domain wall at the disk edge in contrast to the pac-man style annihilation of two domain in its symmetric counterpart. As discussed in Section 3, non-uniformities in the specimen can trigger or lead to different reversal processes and true to form, the deformation in the disk resulted in a different switching processes though the resulting remanent magnetization is the same with. This is a crucial benefit of micro-magnetic simulations as observing these switching dynamics with conventional measurement techniques would not be possible.

4.2   Circular Rings

In disks, the demagnetizing field is prone to flipping direction in the plane normal to the rotational magnetization plane at remanence as the size of the disk shrinks. And if the size is small enough, magnetization reversal would not occur through curling but through uniform rotation as a single domain magnet as discussed in chapter 3. Shown in Figure 25A, the demagnetizing field is seen

to rotate out plane at saturation then propagate inward as remanence begins to take shape. It precess about the disk center and then settles. Though its magnitude is not very large, its precession could cause it to flip direction in the z-axis as the disk shrinks in size. This is because the exchange energy becomes increasingly dominant over the demagnetizing energy. Zhu et al., showed that vortex type magnetization becomes harder to maintain as disk diameter shrinks to 100 ~ 200 nm, near the single-domain regime [55].

(a)   (b)
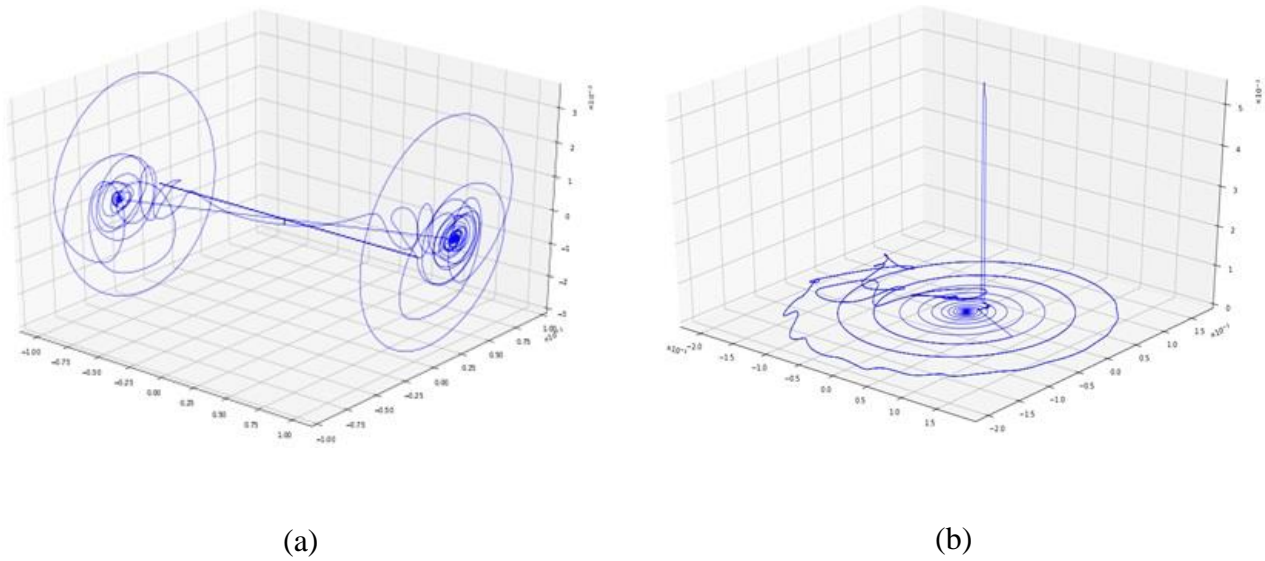
Figure 25 (a) Demagnetizing field at saturation and at (b) remanence.

To remedy this, they proposed using ring elements which essentially remove the unstable vortex core at the disk center. This effectively introduces a third state known as an 'onion' or reset state that is a superposition of the two rotational states. It occurs as the domains form after the ring's

magnetization is driven to saturation by an external field. A 400 nm ring with a 40 nm hole (aspect ratio of 10) at the center in Figure 26A showed this 'onion state'. The two domain walls then migrate and annihilate to form a vortex. Residual rotation of the demagnetizing field at the center of the ring is still present in Figure 26B, indicating the hole is not large enough to completely remove the energetic core. Another ring with a 100 nm hole (aspect ratio of 4) in Figure 27 did not show this residual behavior. It is also worth noting that this ring took significantly longer in simulation time to form domain walls and begin the switching process with the damping factor in the micro-magnetic solver being 0.011. For comparison, the damping factor for a disk and the ring with a 40 nm hole, was 0.0312. The smaller volume of this ring results in a significant reduction in the influence of the vortex core [85].

Larger holes that pushed the aspect ratio below 4 did not settle into remanence at zero field. At aspect ratios of 2.6 and 2 – 150 nm and 200 nm holes – the domain walls formed were a mix of vortex and transverse walls as shown in Figure 28A. At an aspect ratio of 1.33 – a 300 nm hole – in Figure 28B, the domains walls are entirely transverse since there is less space for a vortex wall to form as the hole size increases. Also, the demagnetizing energy of transverse walls is higher than that of vortex walls, so annihilation of all domains within the ring does not take place. A non-zero coercivity is therefore seen in the hysteresis of Figure 28C indicating the ring was not fully demagnetized at remanence. The hysteresis for these smaller aspect ratio rings all showed non-zero coercivity.

(a)   (b)   (c)
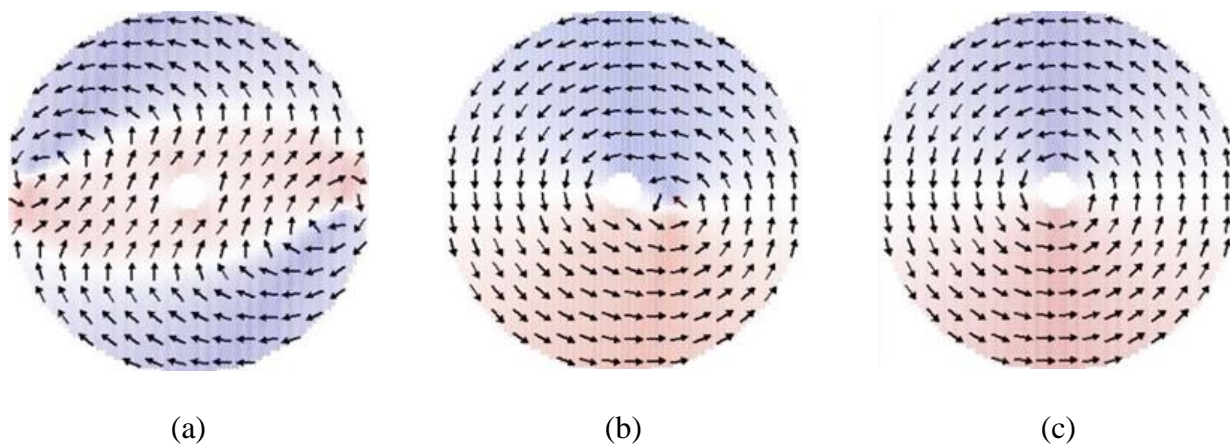
Figure 26 (a) Domain wall formation in ring with 40nm hole. (b) The rotation of the out plane of component of the magnetization. (c) Vortex state of a ring [85].

(a)   (b)
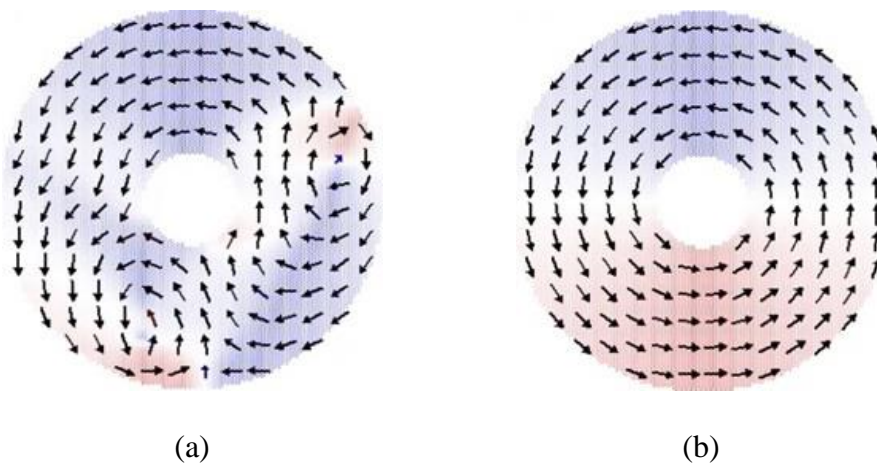
Figure 27 (a) Domain wall formation and (b) vortex state of a ring with 100nm hole. No rotation of the out plane of component of the magnetization can be seen, indicating its minimization [85].
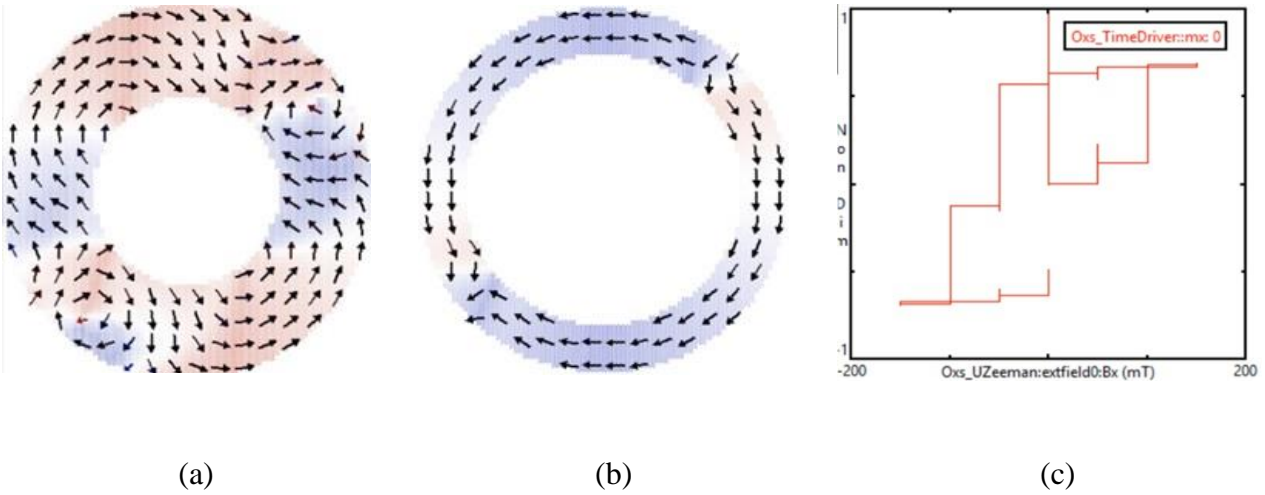
Figure 28 (a) Domain walls formed in ring with a 200nm hole (aspect ratio - 2). (b) Domain wall in ring with 300nm hole (aspect ratio – 1.33). Neither settled into remanent vortex states at zero field (c) Hysteresis of rings of aspect ratios 2.6 and below.

4.3   Correlated Disks

As with all QCA types, an important aspect to consider is the coherent chain length. For circular nanomagnets this is a major challenge since it is dependent on uniformity and geometry of the nanomagnets. Magneto-optical measurements by Welland *et al.,* showed signal propagation for up to 69 spherical single-domain nanomagnets [56]. Similarly, Bernstein *et al.,* studied the effect of coercivity on the signal coherence for different shapes of nanomagnets [51]. Figure 29 shows the shapes and respective lengths of coherent chains. They found that for non-spherical magnets, an average size of 300 nm on the easy axis needed to be maintained to preserve the single-domain nature of the nanomagnets. This is in line with the findings on individual rings whose holes were larger than 100nm. Those rings did not settle into remanence as they were now bordering the single-domain regime. They also found that uniform spherical magnets can switch much more easily since anisotropic effects on

domain wall formation and motion would be minimal. So, elements with spherical edges would be suitable to extending coherent chain length because they can switch much more easily, but they would have to be within the multi or few-domain regime in order to maintain the intermediate vortex state at remanence.
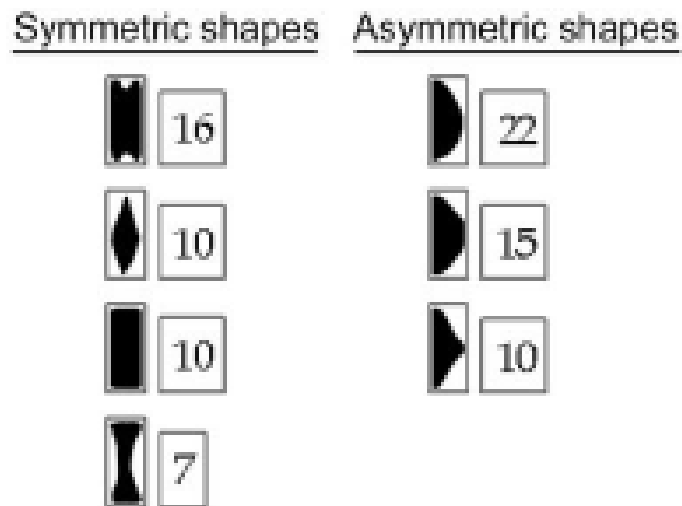
Figure 29 Result of statistical analysis by Bernstein et al., of the average coherent chain lengths of antiferromagnetically coupled magnets *[51]*.

Introducing physical contact as an entanglement mechanism between elements could therefore be useful in further extending coherence. This can be thought of in terms of interlocked mechanical gears of Figure 30. The direction of rotation of each gear is analogous to chirality of the magnetization within each ring. Switching is edge triggered with alternating chirality in adjacent elements since the

quantum exchange force, limited in range by the magnetic exchange length, will align neighboring spins in parallel to one another. In principle, the strength of interaction between elements can be tuned depending on how close they are to one another, i.e. slightly apart, or just touching at the edges. This satisfies the important requirement of tunability in QCA [85].
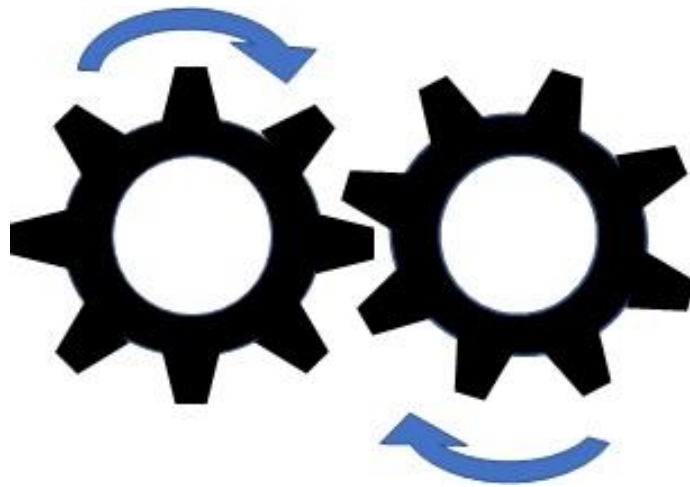
Figure 30 Touching gears rotating in opposite directions.

A pair of disks put together show this edge driven correlated switching. The applied field was at 2° off-axis. In each disk in Figure 31, one vortex type domain forms simultaneously at the free edges. There are no boundary conditions imposed on the free edges of the disks, so magnetic moments there can curl freely. The formation of domains and eventual reversal of the system therefore begins there. Each domain then migrates to the center of each disk much like their individual counterparts. The

migration of the domains is also reflected in the out-of-plane demagnetizing field of the disks in Figure 32. The touching disks end in opposite rotations at remanence.

(a)   (b)

(c)
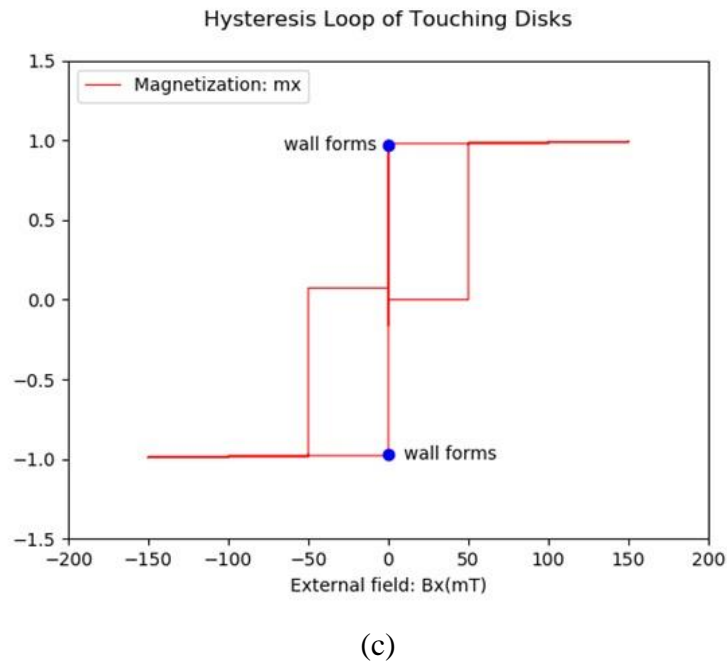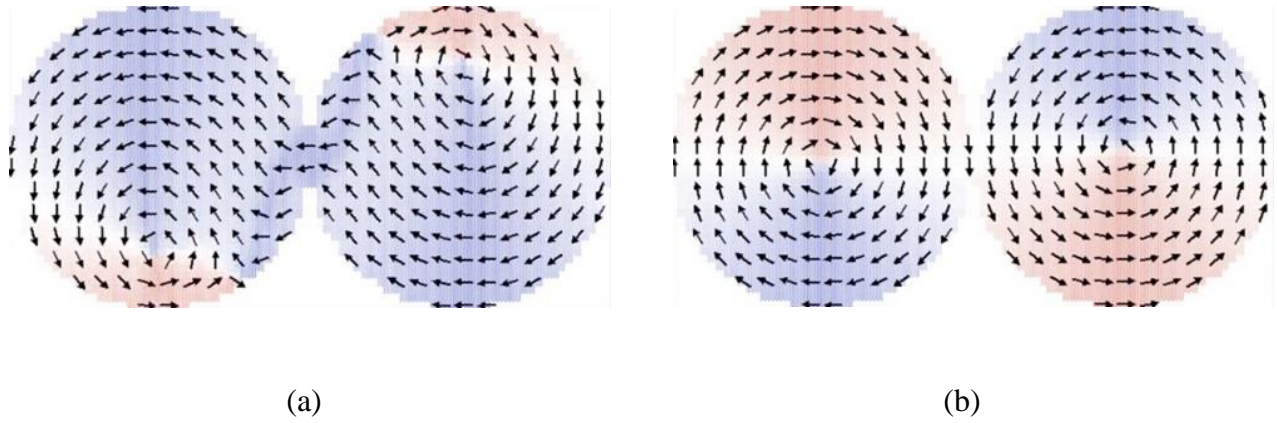
Figure 31 (a) Two touching 400 nm disks as domain walls form. (b) The correlated end state of the two disks. (c) Hysteresis loop of the touching disks [85].
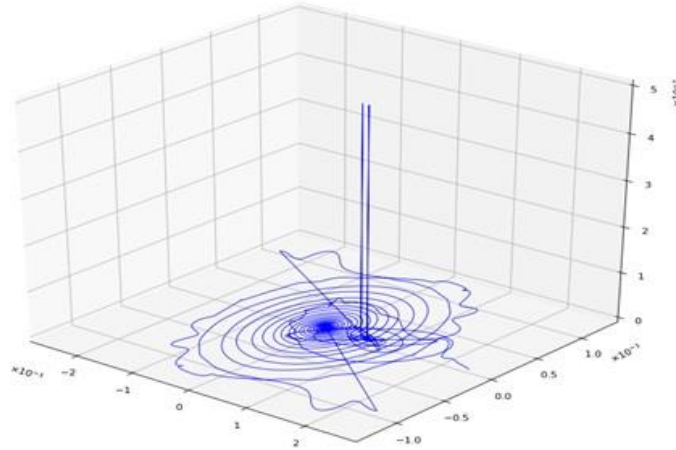
Figure 32 Demagnetizing field of touching disks. Migration begins at the edges of both disks and eventual end up near the center.

The bidirectional nature of the switching seen with two disks becomes problematic when three or more elements are in play. In a three-disk chain, the two outermost disks begin to switch with one vortex type wall each at their free edges while the central disk's magnetization is pinned at both of its edges. The outer disks resolve into their remanent vortex states while the central disk's magnetization is left in a superposition of two competing chiralities as in Figure 33A, 33B. The addition of an elongated biasing element to the three-disk chain as shown in Figure 34A imposes a unidirectional order on the switching process. Like disks, switching in elongated elements starts from the edges but magnetization reversal does not occur happen through a vortex since the magnetic moments prefer to be aligned along the easy axis. A higher magnitude switching field is therefore required to force the magnetic moments to flip direction. A disk in contact with a biasing element would see its magnetization pinned and its reversal delayed, until the switching field of the biasing element is reached, allowing unidirectional switching [50,51,72,85].

The biasing element used here was a diamond 400 nm X 100 nm. The applied field was at 87° along the y-axis, the easy axis of the diamond. This angle was chosen to ensure magnetization was not pinned along the biasing element's hard axis. Also, a field in this direction would allow domain walls to form in the central disk as they cannot form at the points of contact with neighbors. In Figure 34A, the rightmost disk begins switching with the nucleation of one domain wall. It resolves itself into its remanent vortex state first with the precession of the vortex core still present. The leftmost and middle disks on the other hand, form two domain walls before resolving their remanent states themselves simultaneously. The system ends with the correlated magnetization of the disks in Figure 34B, 34C. The direction of the biasing element also ends up in similar fashion. A correlated disk chain could therefore be used as a magnetically coupled wire.

(a)

(b)
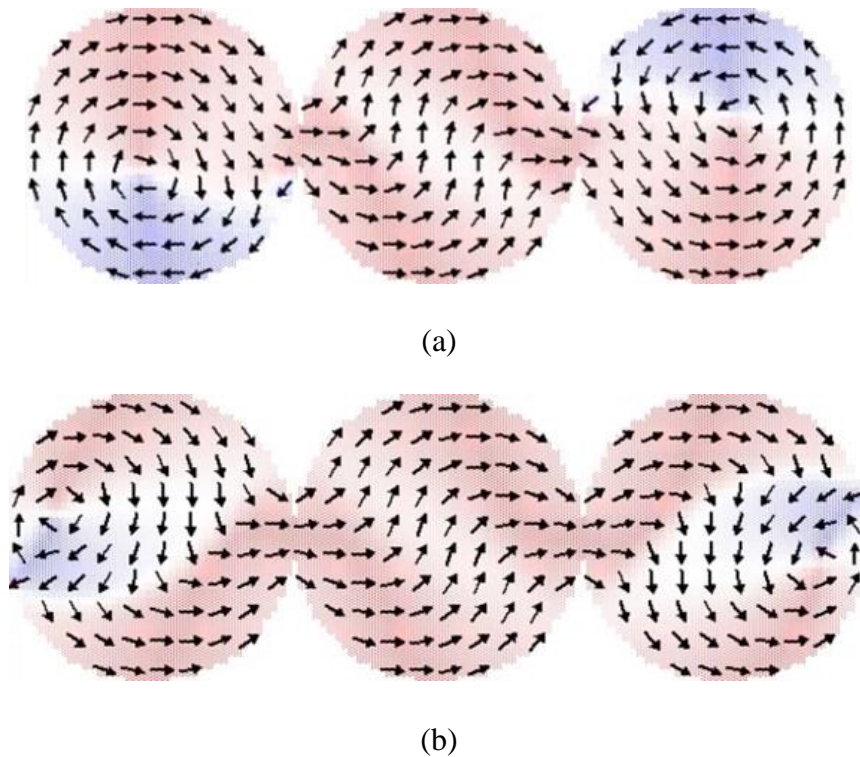
Figure 33 (a) A three-disk chain. System simultaneously begins switching at the free edges of the two outer disks. (b) The central disk ends in a superposition of competing chiralities [85].

(a)

(b)

(c)
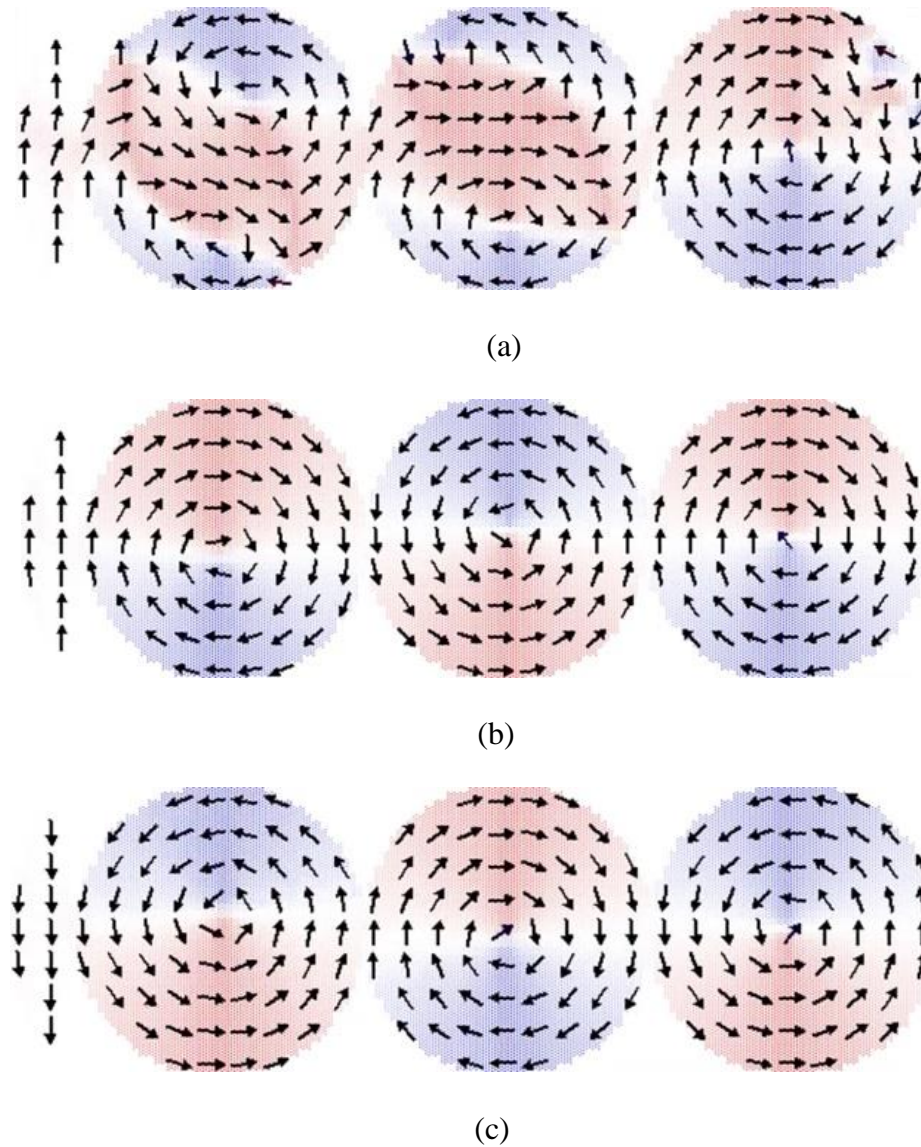
Figure 34 (a) A three-disk chain with a biasing element. The rightmost disk forms one domain wall and settles into a vortex first. The other two disks form two domain walls, with their switching delayed by the interaction with the biasing element. (b-c) The correlated end states from positive and negative saturation [85].

Unfortunately, this method for imposing unidirectional switching does not work for larger chains of disks. In the four-disk chain of Figure 35, the magnetizations of the leftmost disk and the biasing element did not end up in the same direction although all the disks are correlated, and the switching, unidirectional. The switching dynamics of this chain is very similar to its three-disk

counterpart. The only difference being that disks 1, 2, and 3 resolve their remanent states at the same time. In Figure 36, the unidirectional benefit of the biasing element is lost as the disks seem to switch without regard for their neighbors. This can be seen even more clearly in Figure 37 which shows a six-disk chain where the switching happens in pairs. Overall correlation is not present, although it can be seen at two locations in the chain.

(a)

(b)
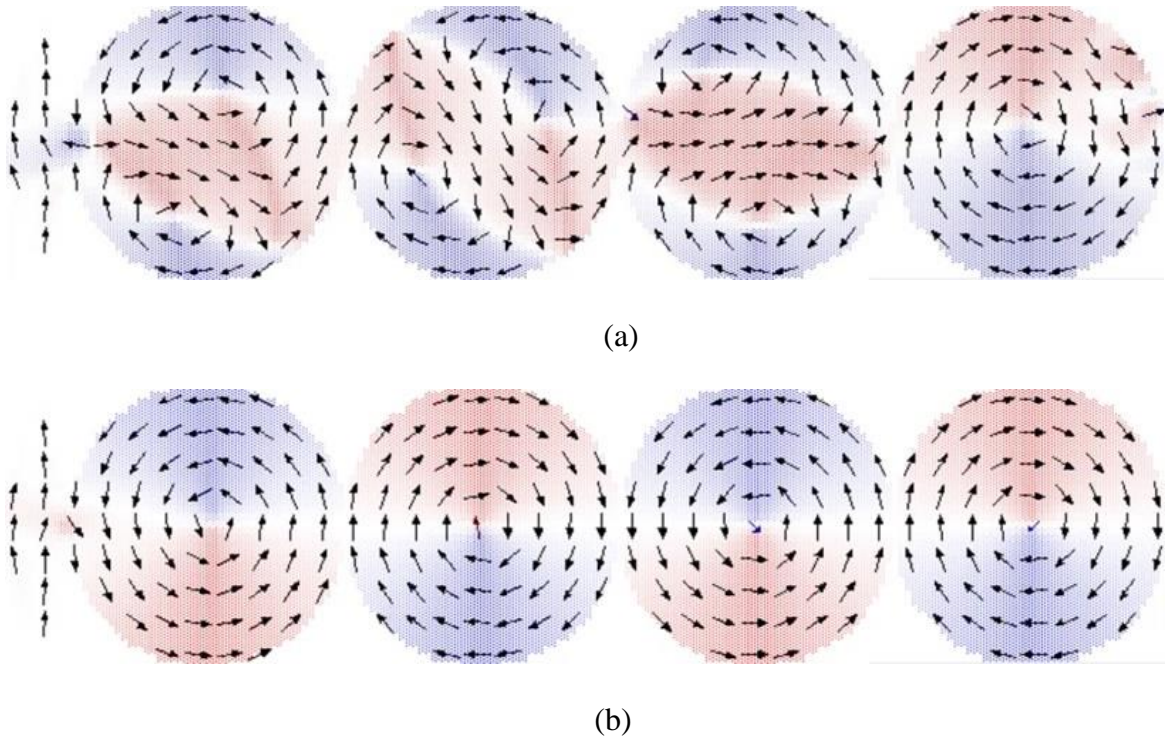
Figure 35 (a) A four-disk chain with biasing element during the switching process. (b) Although the disks end in a correlated state, the leftmost disk is not correlated with the biasing element, suggesting correlated volume is limited to 4 elements [85].

This suggests that the correlated volume, the maximum number of elements that can remain magnetically coupled in this system is four [85,86]. It should be noted that reducing the simulation mesh below the magneto-static exchange length of 5 nm did not change these results.

(a)

(b)
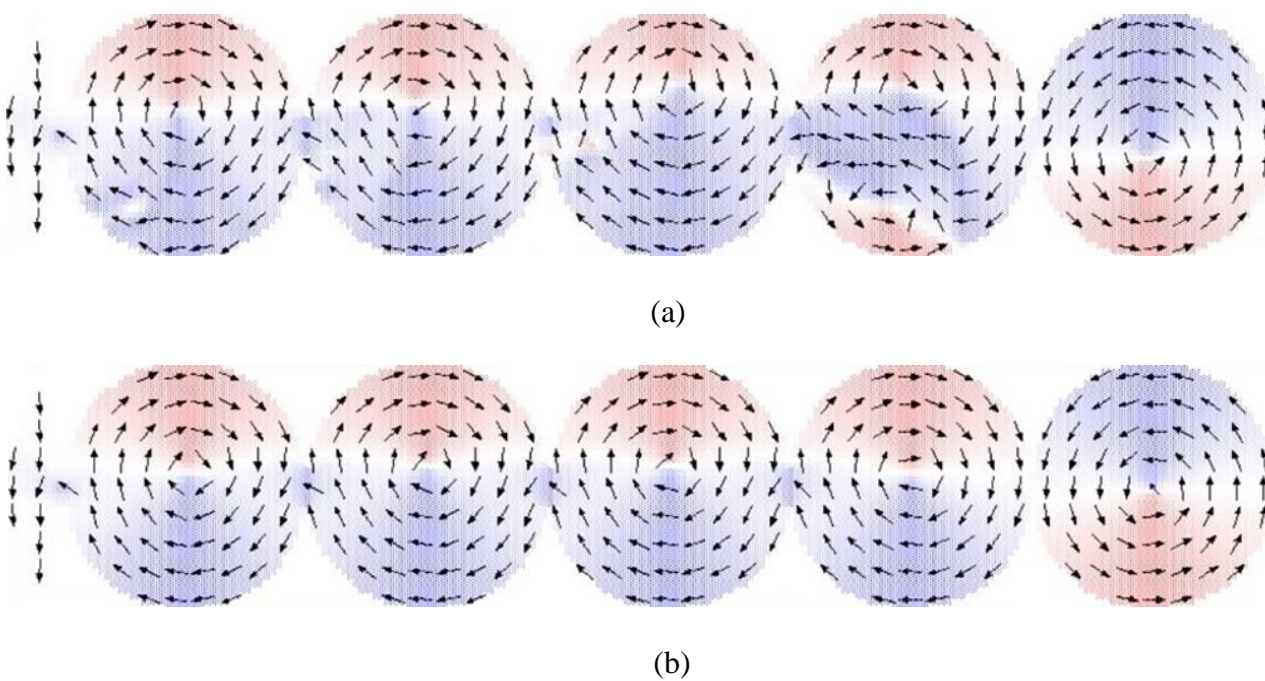
Figure 36 (a) A five-disk chain with biasing element where unidirectional aspect of switching has been lost. (b) End state does not show overall correlation of disks.

(a)

(b)
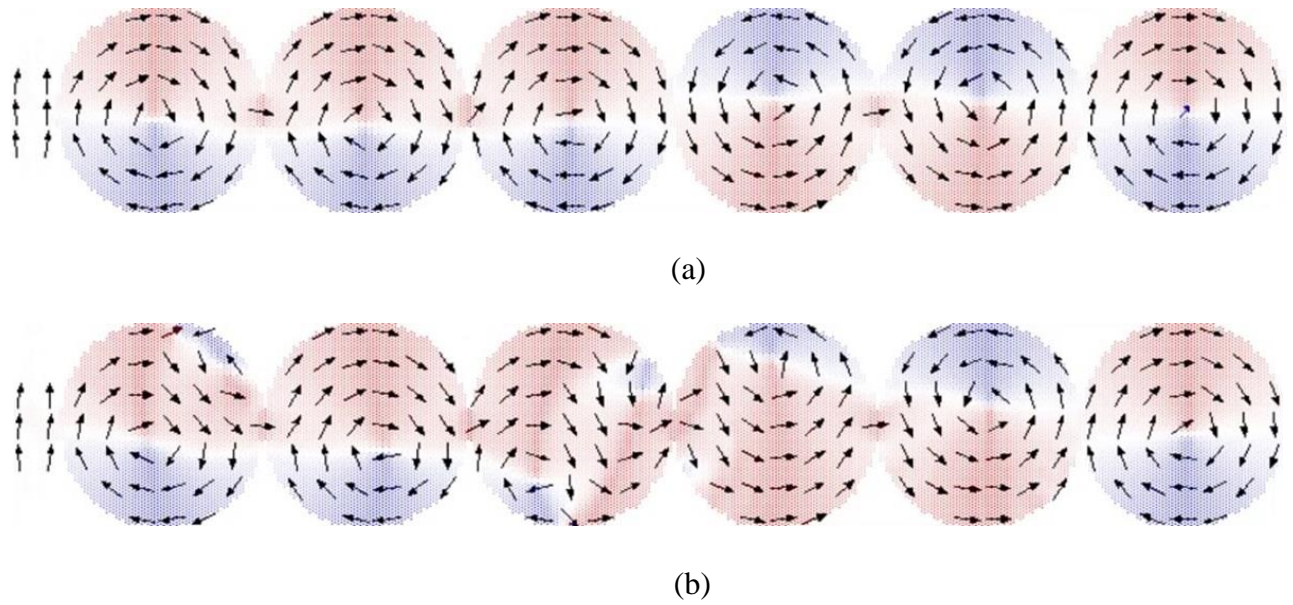
Figure 37 A six-disk chain with biasing element. (a) Interaction is pairwise as both the leftmost and rightmost pairs of disks enter vortex, although not necessarily correlated. They are followed by the two innermost disks. (b) End state of chain. Correlation is present in two locations.

4.4   Correlated Circular Rings

Like their disk counterparts, touching rings showed similar reversal mechanics. For an 87° off-axis applied field, only one domain wall forms per ring at their free edges. The domains walls once again move perpendicular to the direction of the applied field. Figure 38 shows pairs of 400 nm rings with 40 nm and 100nm in remanence along with hysteresis loops that are symmetric like those of individual rings. Again, residual rotation of the vortex core was present in the former but not in the latter.

There were two significant differences observed between the case of touching disks and touching rings. The first was that only even numbered chains of rings ended in correct correlation. Odd numbered chains simply ended with the central ring in a superposition of competing chiralities. For three and five-ring chains, in Figure 39A, 39B, this was the case. One thing to note is that, in touching

disks, the interaction of the demagnetizing fields in each disk helps to strongly couple the disks in addition to the quantum exchange force at the point of contact [86]. In rings however, removing the influence of the demagnetizing field, leaves only the exchange interactions at the contact point between rings as the coupling mechanism. This leads to strong preference to switch in pairs. In the odd numbered chains, the central ring formed two domain walls that migrate in response to the chiralities of its neighbors on each side. However, one chirality cannot dominate over the other thanks to the symmetry of the system, the central ring therefore remains in a superposition state of the two competing chiralities as the domain walls do not move. In the four-chain of Figure 40, the process begins with the two outer most disks forming one vortex type wall each and then resolving their vortex states. The two innermost disks then follow suit but with two vortex type domain walls each. The difference here being that from the perspective of one of the inner rings, the domain walls in its fellow inner ring neighbor are able to move, hence its domains are able to move as well, and it's not restricted from vortex. The entire process is certainly not unidirectional, and in contrast to their disk cousins, a biasing element was not needed since the influence of the demagnetizing field on the switching process is significantly reduced [85].

(a)

(b)

(c)
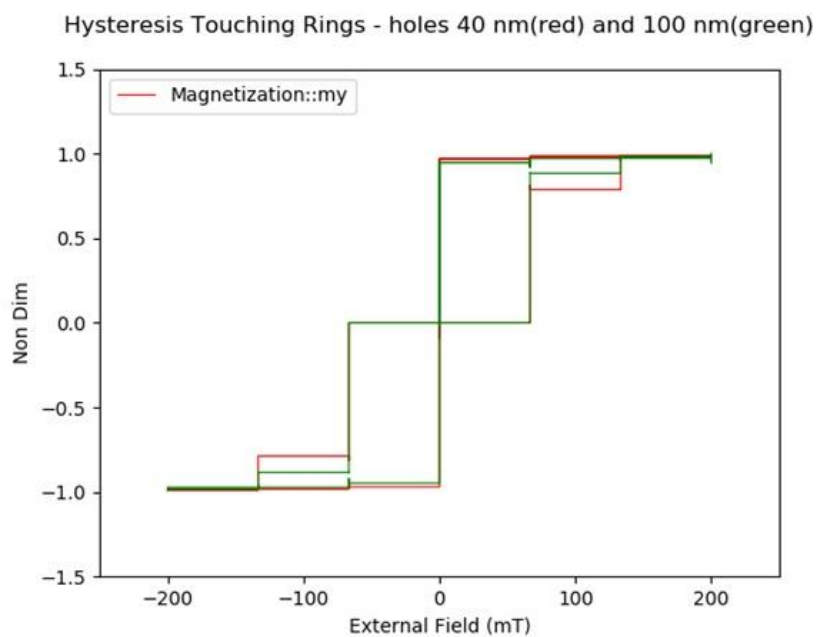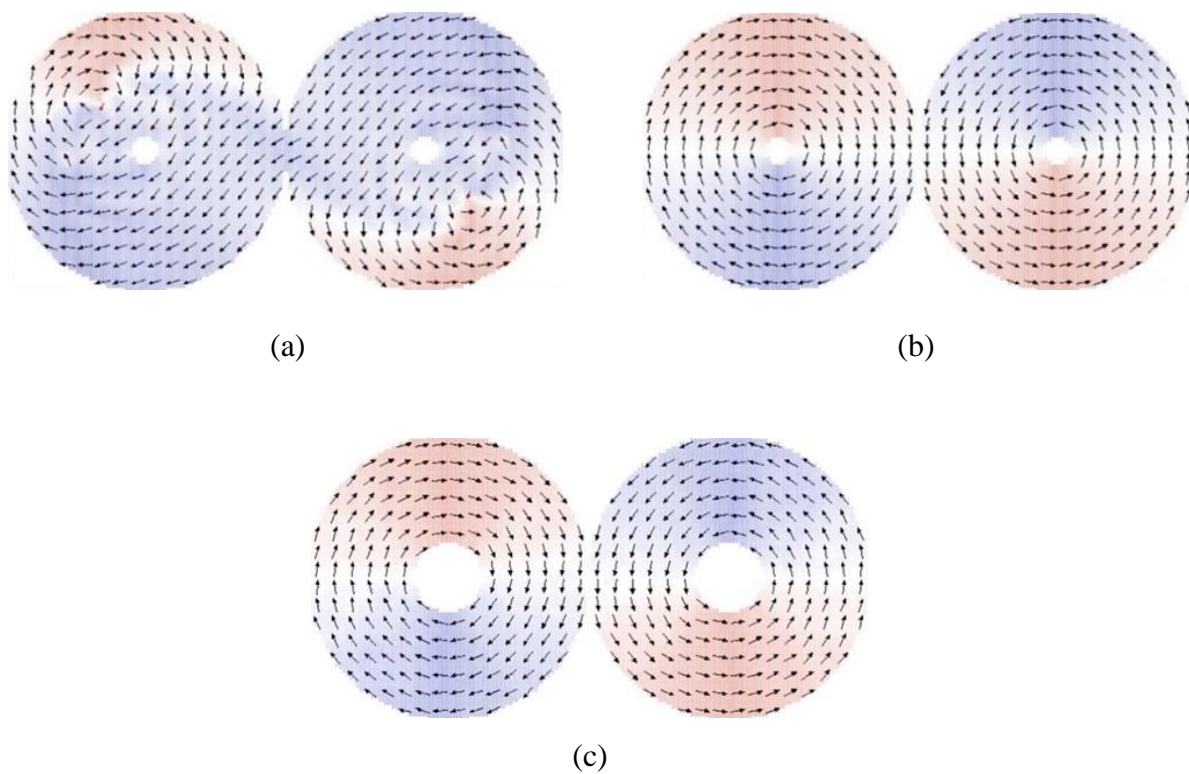
(f)

Figure 38 (a) Domain walls in touching rings. (b-c) Correlated switching in touching rings with 40nm and 100nm holes. (d) Comparison of hysteresis loops of touching rings [85].

(a)

(b)
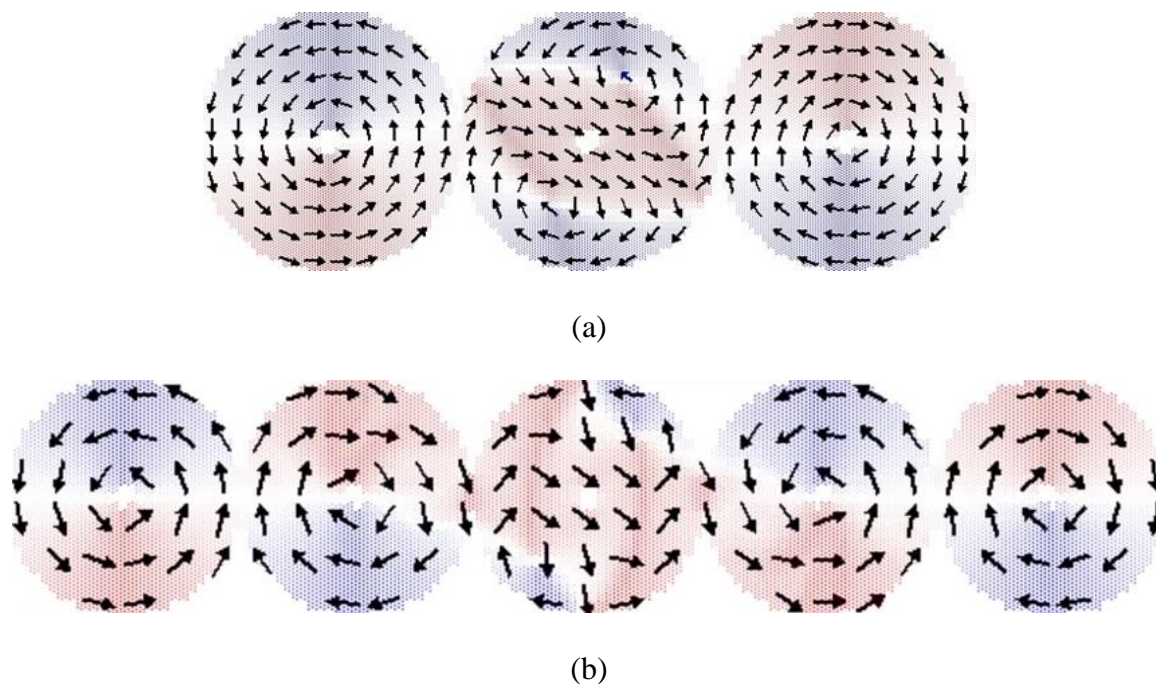
Figure 39 (a) Odd numbered chains of three and (b) five rings with 40 nm holes. The central ring is stuck in a superposition of chiralities like their three-disk counterpart.

(a)

(b)
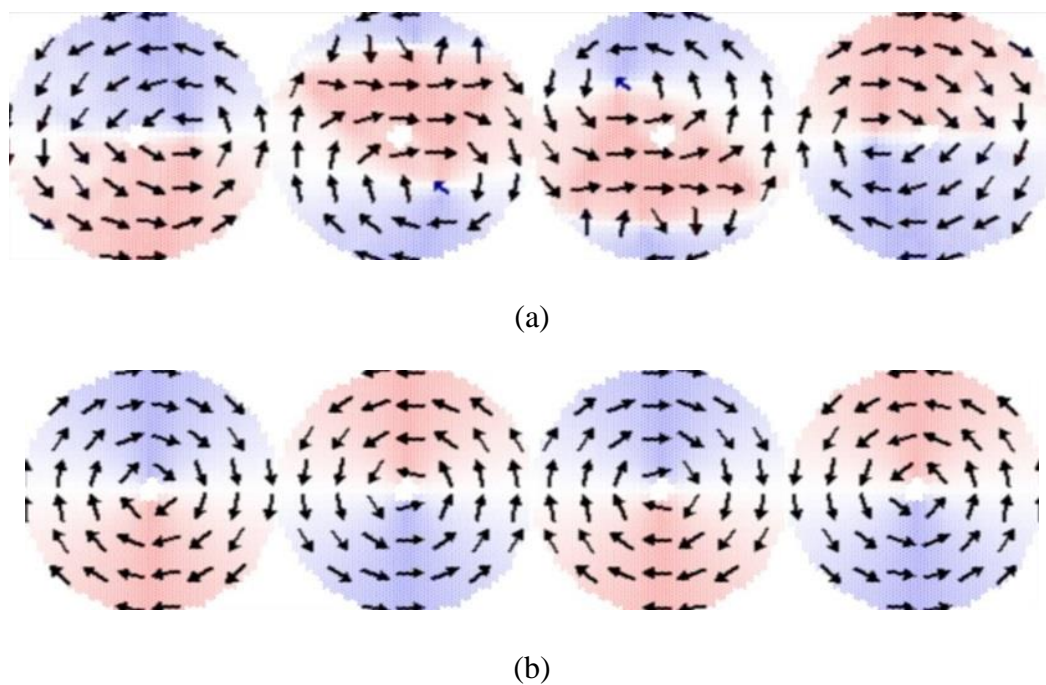
Figure 40 A four-element chain of rings with 40 nm holes. (a) Switching begins with the two outermost rings. They are followed by the two inner rings. (b) Correlated state of the linear chain of rings [85].

Pair-wise switching has been observed in chains of rings where the field was applied perpendicular to the direction of the chain as is the case here [57,72]. This preference for switching in pairs is seen rather more clearly in Figure 41. In this six-ring chain, the two outermost rings once again resolve themselves first with a single vortex type wall each. They are followed by the inner rings broken into pairs of rings 2,3 and rings 4,5 as seen in Figure 40. The point between rings 3 and 4 does not see much activity as the magnetic moments are already in the same direction. Hence the interactions are taking place at the points between rings 2,3 and rings 4,5.

(a)

(b)

(c)
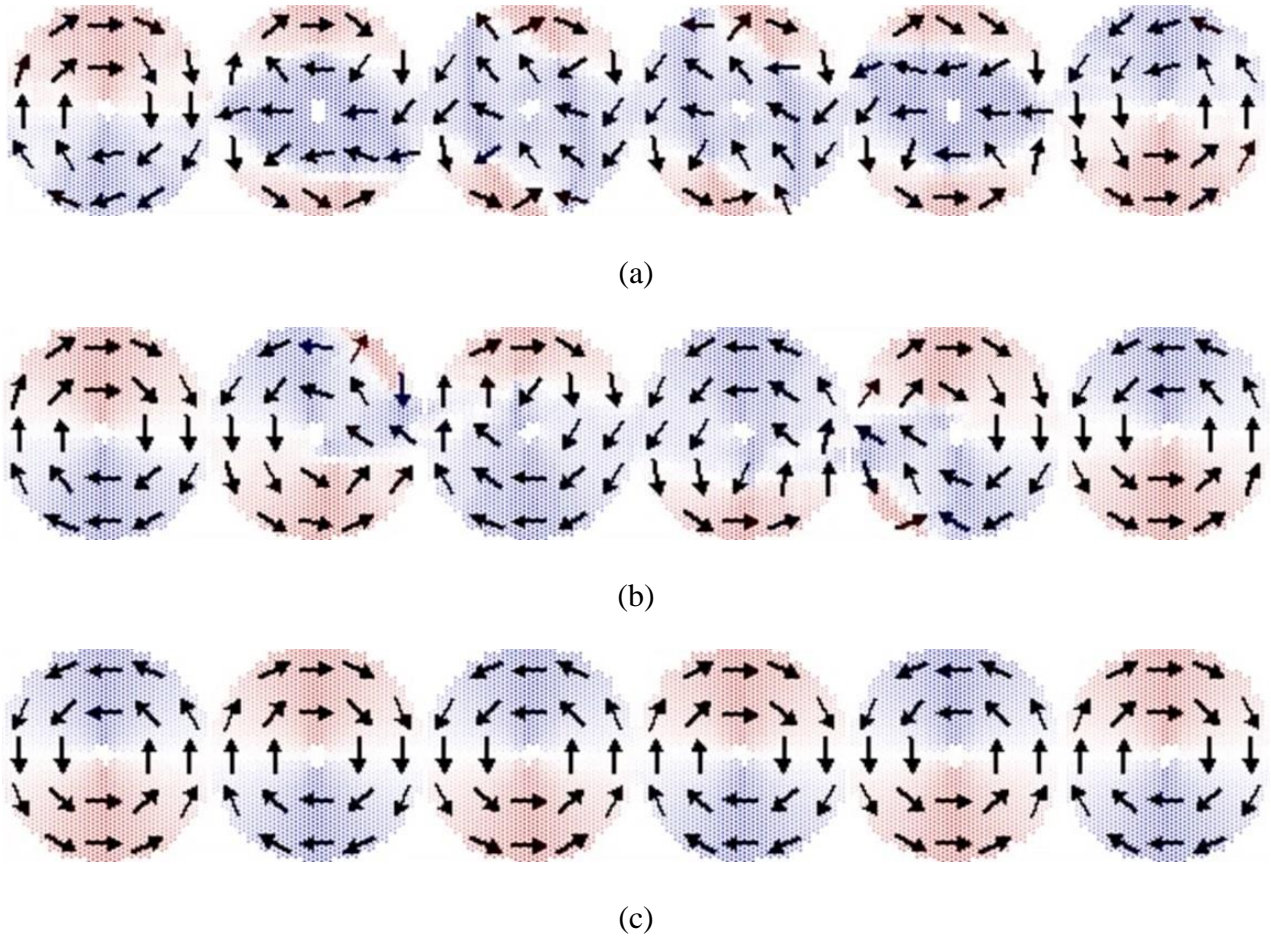
Figure 41 Chain of six-rings with 40 nm holes. (a) Domain wall formation in the inner rings after the two outermost rings resolve their vortex states. (b) Pairwise interaction between rings 2,3 and 4,5. (c) Correlated state of the linear chains of rings [85].

The second significant difference observed was a change in the direction of switching. The four-ring chain with 100 nm holes of Figure 42 depicts this directional change [85]. The two inner rings first settled into their correlated vortex states through two vortex types domains each. They are followed by the outer rings, in this case also spotting two vortex domains each as well. Given the elements in this case were symmetric, we can neglect non-idealities that could arise from shape anisotropy leading us to conclude that the aspect ratio plays a significant role in the switching process for a linear chain or rings.
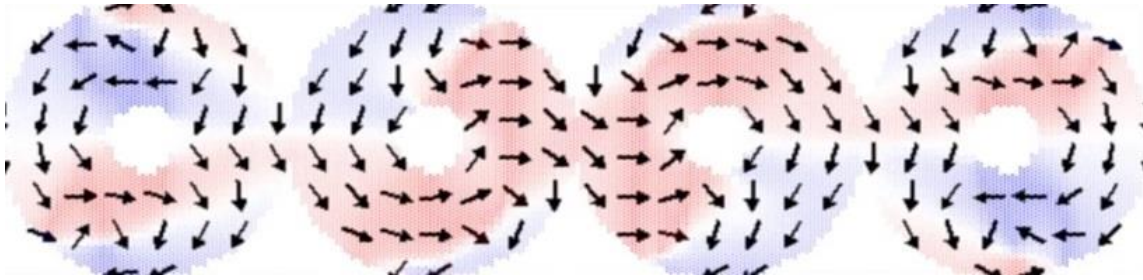
(a)
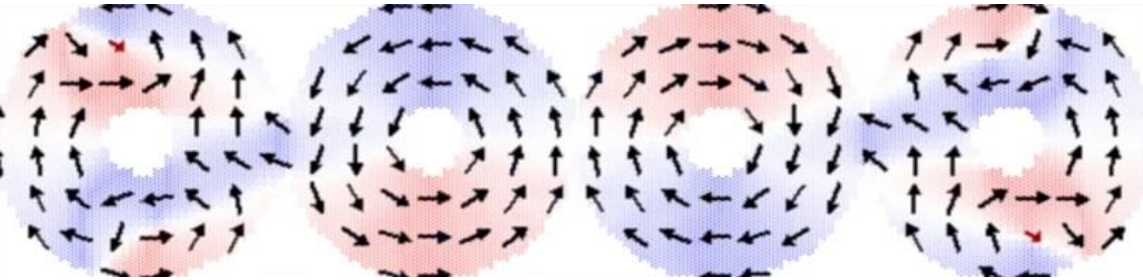
(b)
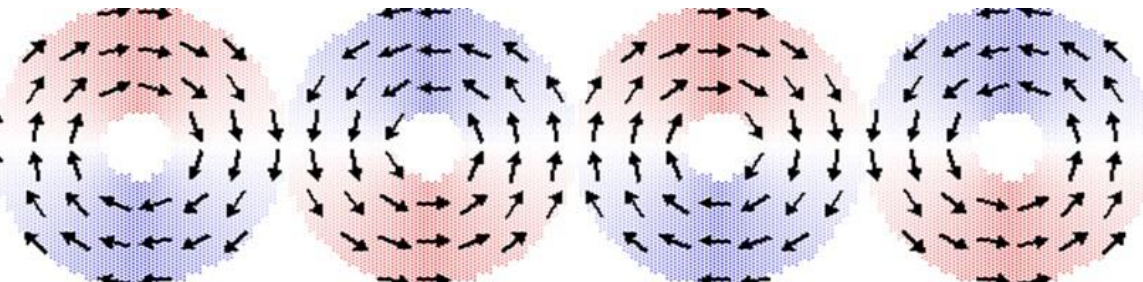
(c)

Figure 42 (a) Domain wall formation in a chain of four-rings with 100 nm holes. (b) Change in direction of switching is observed with inner rings settle into their vortex states first followed the two outermost disks. (c) Correlated state of the linear chains of rings [85].

This then raises a very interesting question. What aspect ratio marks the transition where the bidirectional switching of outward → inward reverses to inward → outward? Simulations of rings with aspect ratios of 8 (50 nm hole), ~ 6.06 (66 nm hole), and 5 (80 nm hole) were thus performed.

(a)

(b)
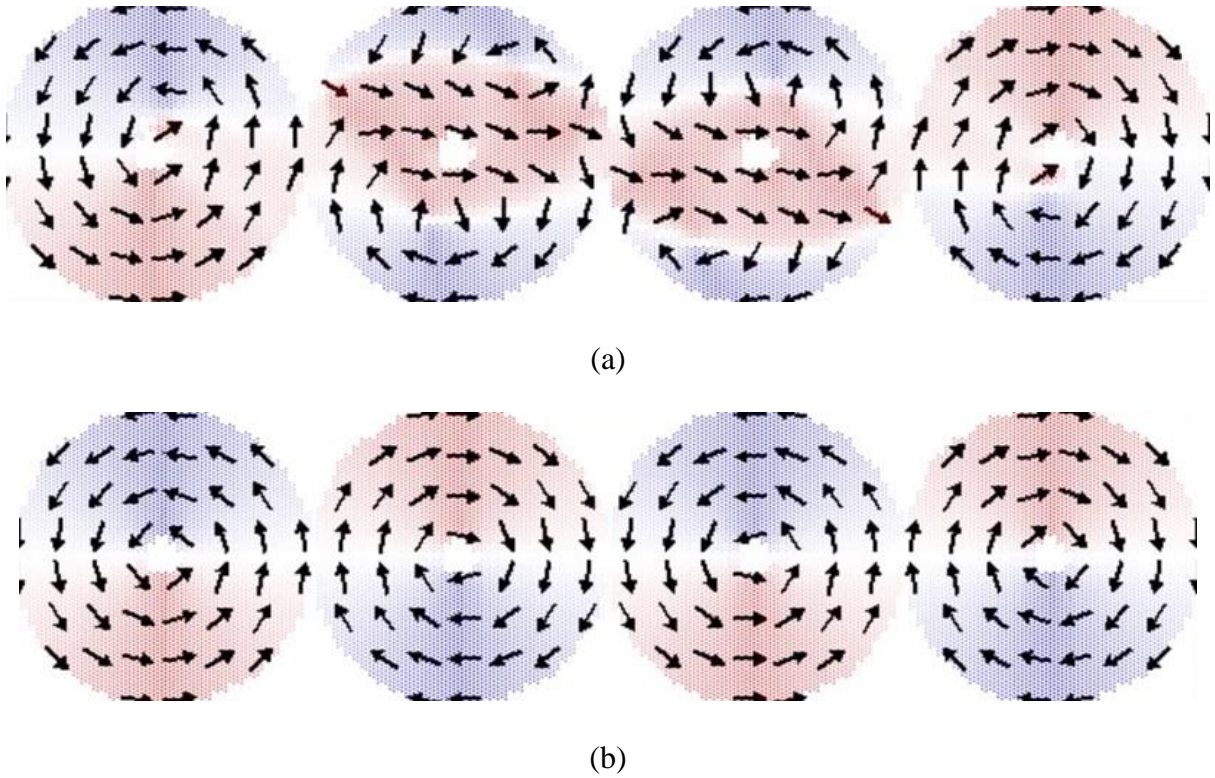
Figure 43 (a) Rings with 50 nm holes – aspect ratio of 8 – during the reversal process. The process looks practically identical to their cousins with 40 nm holes – aspect ratio of 10. (b) Correlated end states of the rings.

For the rings of aspect ratio 8, the reversal process looked practically identical to rings of aspect ratio 10 (40 nm holes). The process in Figure 43A, 43B outward → inward switching. For the aspect ratio system of 5 (80 nm hole), the reversal process again was outward → inward as seen in Fig 44A. However, the rings did not end in the correct correlation even though they all settled into vortex states. Correlation can only be seen at one point in the chain in Fig 44B, between the inner rings. Going by this result, this suggests only rings with even aspect ratio can achieve correct correlation. This would not be out of the realm of possibility given the pair-wise nature of switching was observed in both disks and rings. Similarly, the odd numbered ring chains of Figure 39 did not end in correct correlation either as there was nothing in the system to break the superposition induced by the symmetry of its neighbors.

In the aspect ratio system of ~ 6.06 (66 nm hole), the same reversal process starting with edge elements followed by inner elements is seen. Curiously though, the rings did not end in the correct correlation even though the aspect ratio here is approximately even. The only point where correlation is present is again at the point between the inner rings. This further suggests that in addition to needing an even number of elements with even aspect ratios, said aspect ratios should be even integers. However, one possibility for this result may be due to the mesh discretization in the simulation code. OOMMF requires the entire simulation dimensions to be integer multiples of the mesh discretization. It is possible that non-integer aspect ratios introduce numerical instabilities that affect stepwise rendering of the elements in the simulation.

(a)

(b)
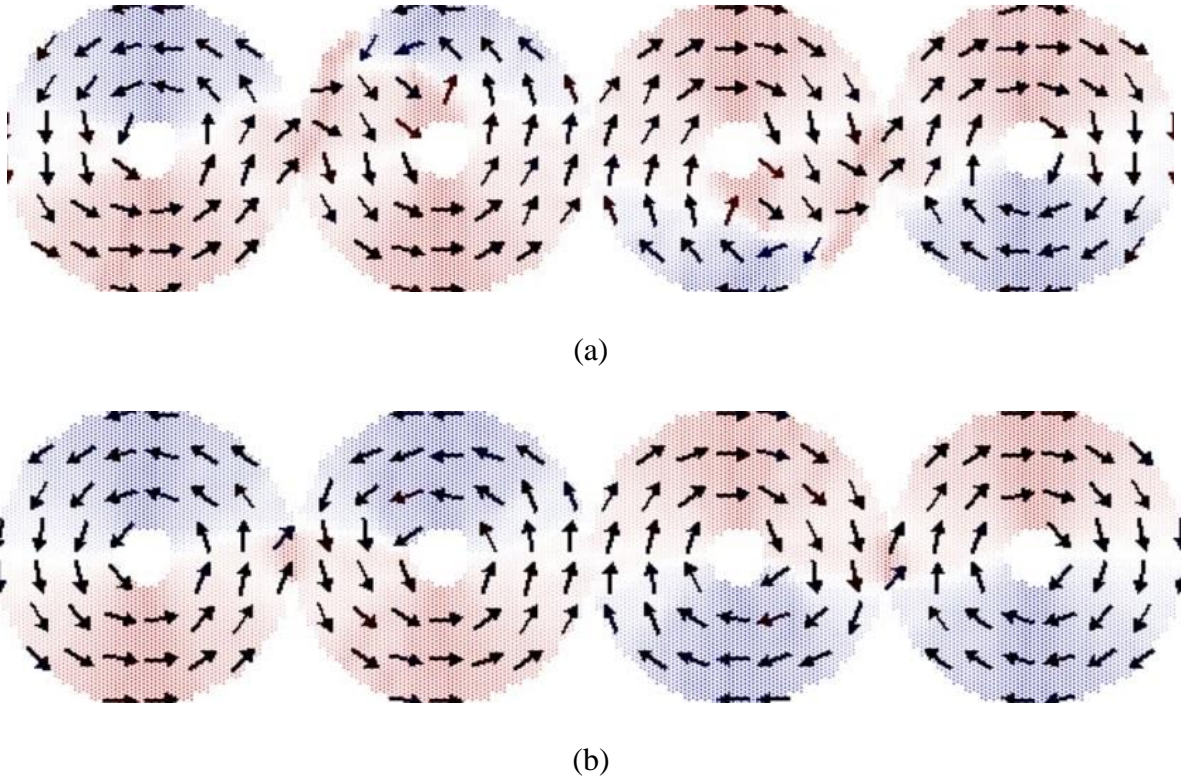
Figure 44 (a.) Rings with 80 nm holes – aspect ratio of 5 – during the reversal process. Reversal process is edge rings first, followed by inner rings. (b.) End states of the rings not in correlation.

(a)

(b)
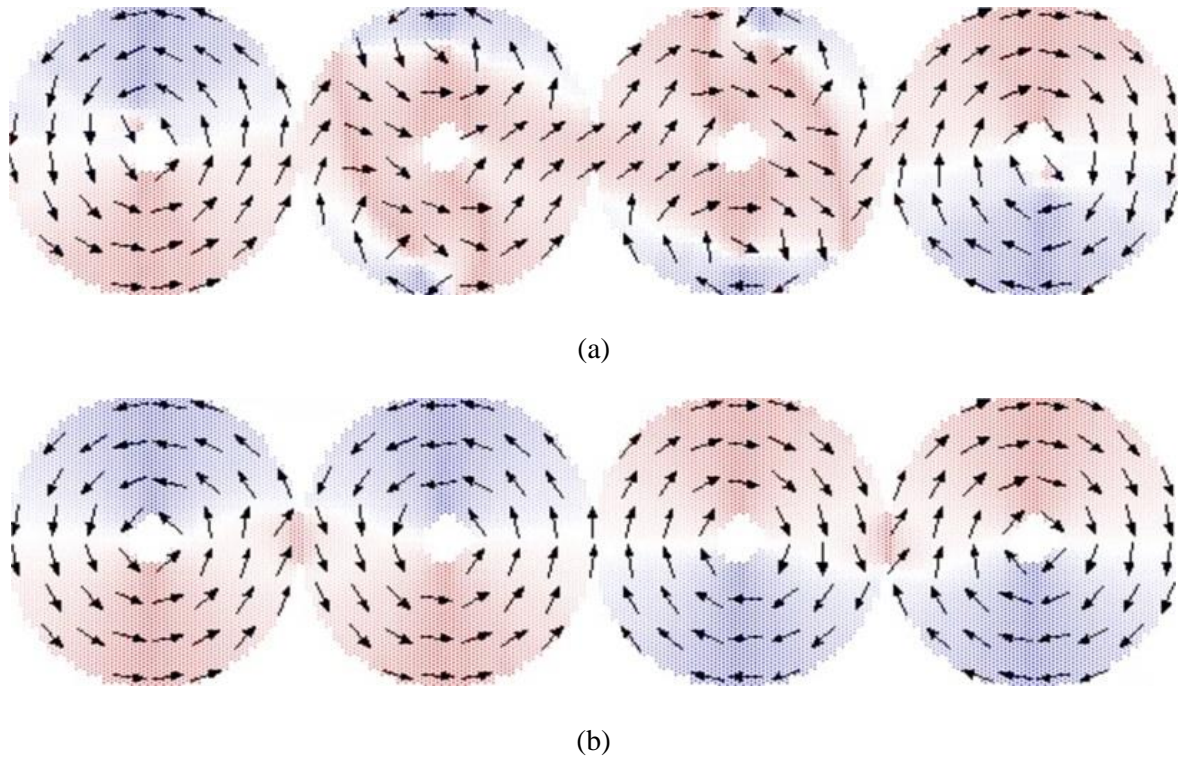
Figure 45 (a) Rings with 60 nm holes – aspect ratio of ~6.06 – during the reversal process. Reversal process is edge rings first, followed by inner rings. (b) End states of the rings not in correlation.

To put these two observations to the test, another simulation, this time with 420 nm rings, was done for aspect ratio of 6 (70 nm hole) and 7 (60 nm holes), and ~6.08 (69 nm hole). Immediately, we see in Figure 46 and Figure 47 that the first observation of requiring an even aspect ratio is produced similar results. Even, with the increased ring size, the system with aspect ratio of 6 ended in correct correlation while that with aspect ratio of 7 (60 nm hole) did not. The reversal process remains edge rings first followed by inner rings. For the ~6.08 aspect ratio in Figure 48, with the same reversal process present, we again see that this system did not end in the correct correlation.

Considering all these observations together, we can say the aspect ratio for circular rings is a very influential factor in addition to the known factors discussed in the previous chapter. This

sensitivity is made even more apparent in the fact that for the elements and aspect ratios simulated, the transition from outward → inward to inward → outward switching was only seen once in the four-ring chain of aspect ratio 4 (100 nm holes) in Figure 42. A likely reason being, with the larger hole, the width of the magnetically active area is reduced to 300 nm, and the nano-magnets are now getting closer to the multi/single-domain transition border of Figure 17B [51,55].

(a)

(b)
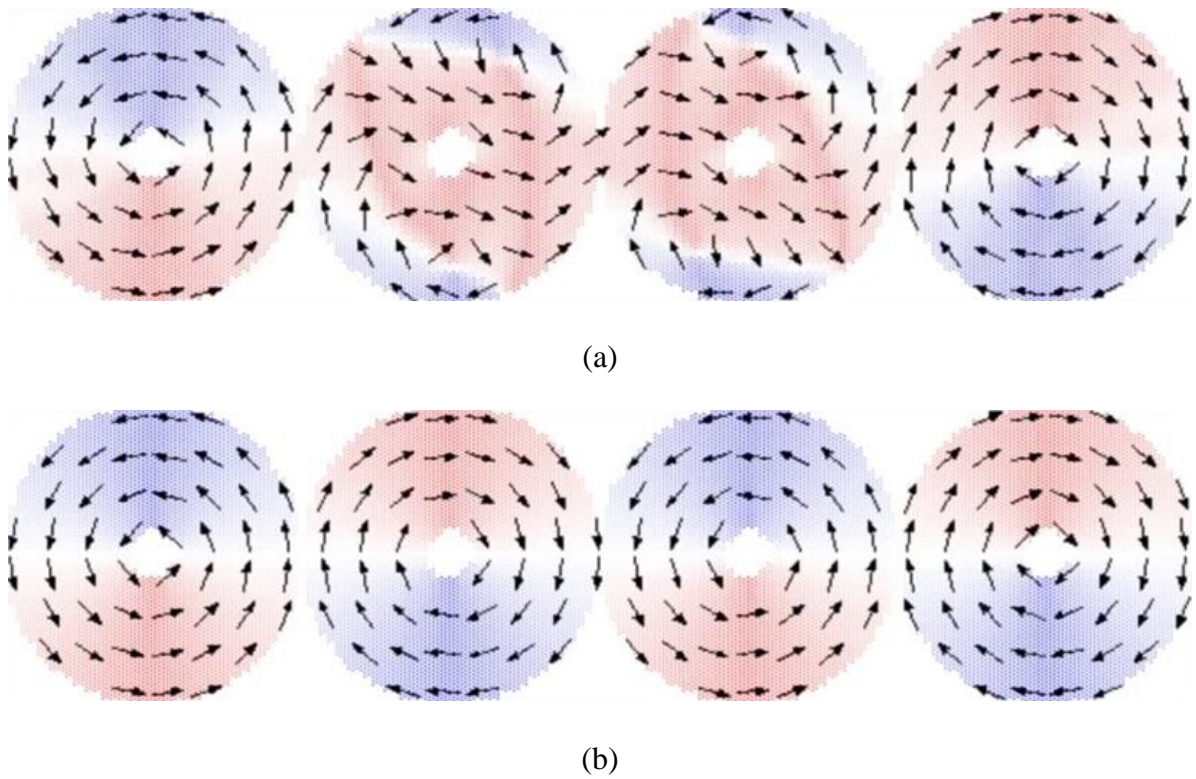
Figure 46 (a) 420 nm rings with 70 nm holes – aspect ratio of 6 – during the reversal process. (b) Correlated end states of the rings.

(a)

(b)
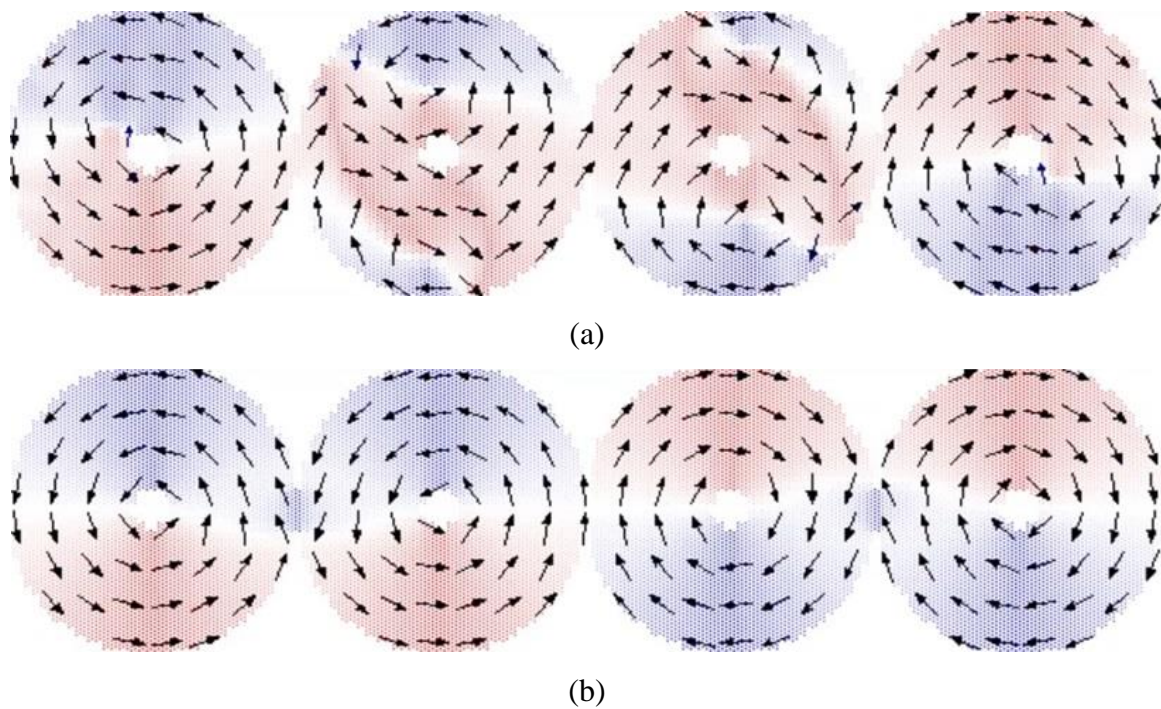
Figure 47 (a) 420 nm rings with 60 nm holes – aspect ratio of 7 – during the reversal process. (b) End states of the rings not in correlation.

(a)

(b)
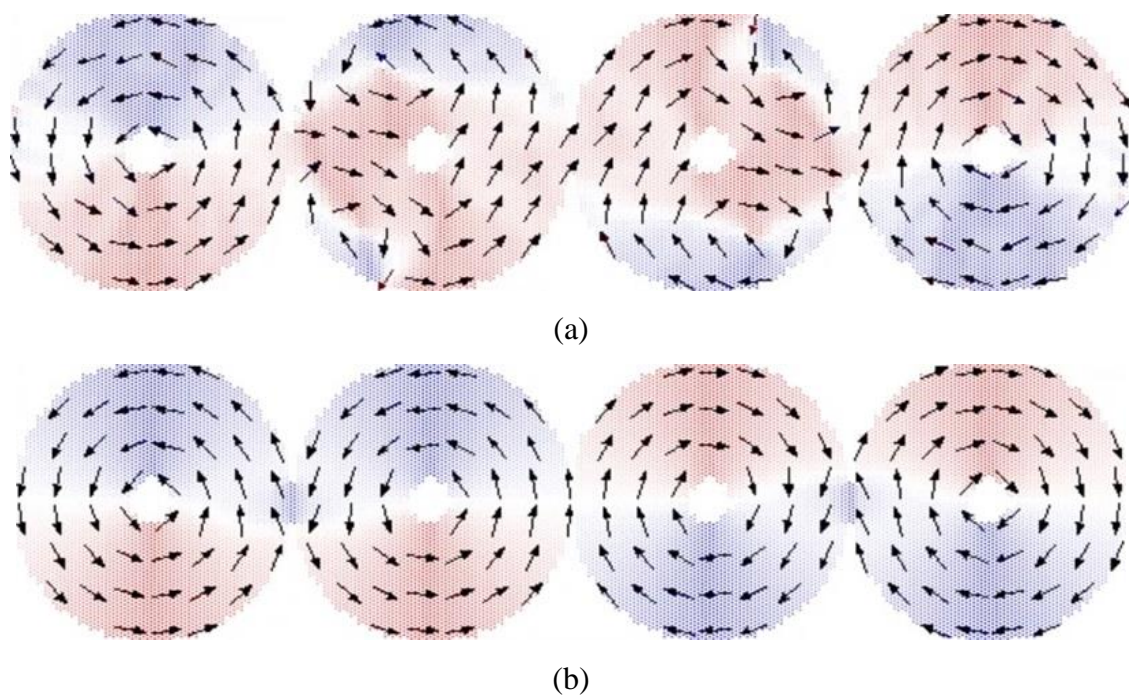
Figure 48 (a) 420 nm rings with 69 nm holes – aspect ratio of ~6.08 – during the reversal process. (b) End states of the rings not in correlation.

4.5   Unidirectional Correlated Rings

Keeping in mind the change to inward → outward switching for the four-chain rings of aspect ratio 4, (100 nm holes), another hypothesis can be made – unidirectional switching of mixed elements is possible. The switching in disks happens much faster than in rings as evidenced by the larger damping factor for disks and rings of large aspect ratio. Also, as discussed earlier, as the holes in the rings get larger, the thermal energy starts to compete with both the exchange and demagnetization energies, meaning the domains take longer to form in rings of small aspect ratio. So, a chain of rings interrupted by disks, should allow for the propagation of switching in one direction.

Figure 49A, 49B shows this mix of elements. It consists of four elements, elements 1 and 3 being disks, while elements 2 and 4 are rings with 40 nm and 100 nm holes, respectively. The first disk resolves its vortex state first. It is then followed by elements 2 and 3. These settle into their vortex states almost simultaneously. This is because element 2, the ring with 40 nm hole, is not much different from a disk as the hole size is not large enough to remove the whole vortex core. Element 4 then follows by resolving its vortex. The end state of the system is the correlated mixed chain shown in Figure 49C.
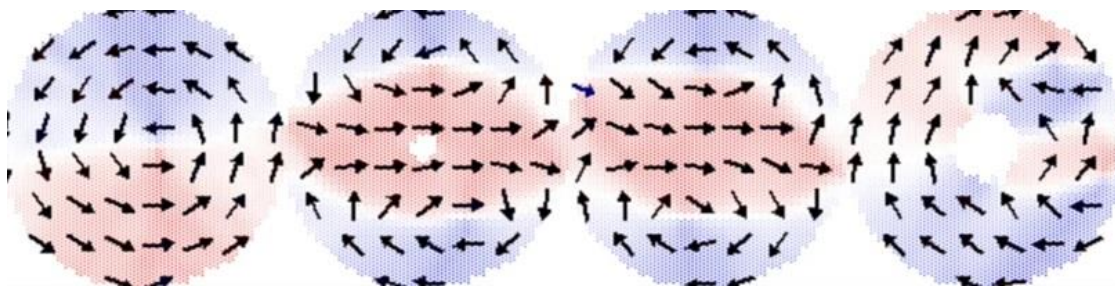
(a)
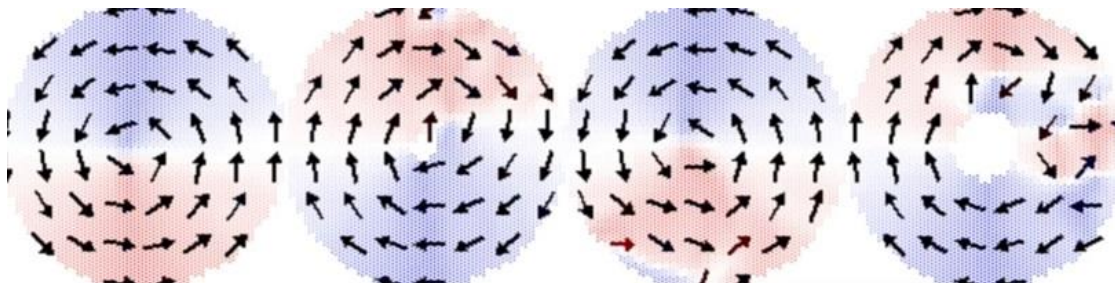
(b)
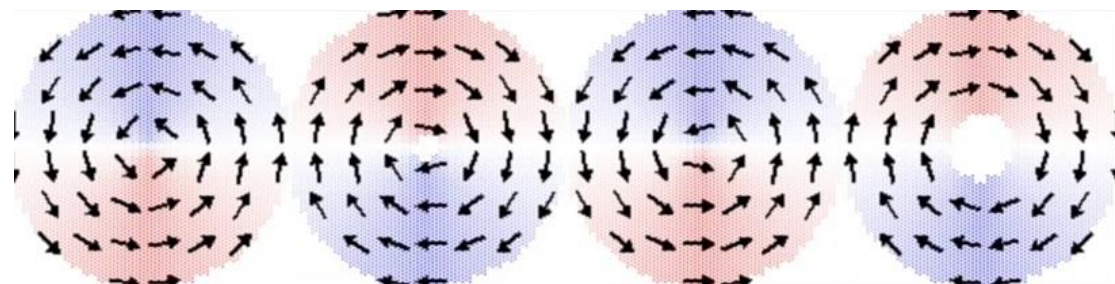
(c)

Figure 49 Mixed chain of disks and rings showing unidirectional switching. (a) Element 1 – a disk – settles into vortex first while the other elements still have domain walls. (b) Element 2 – ring with 40 nm hole – and element 3, another disk, follow suit. (c) Element 4 – ring with 100 nm hole – is the last to settle.

V.   Complex Logic Gate

In any computing regime, the need for devices that can perform complex logic is paramount. By the observations made in the previous chapter, it is possible to look at options for realizing said complex logic with a mix of elements. A majority gate, like the one discussed in Figure 14C comes to mind. Here, the elements of the gate are based on circular nanomagnets. We now look at two aspects that determine the viability of such a gate – stable, reliable inputs, and robust and repeatable outputs.

5.1   The Challenge of Inputs

To use the elements discussed in this work as inputs to a gate would require deterministic control of the chirality. As discussed earlier in section 4.1, the probability of either chirality in symmetric elements is 50%, regardless of the direction of the applied field, so they would not be suitable as standalone inputs. Devices like magnetic tunnel junctions used in magnetic random-access memory to read and write data based by passing current through adjacent contacts are one option in realizing inputs. Another is to use spin-polarized current as in the STT method discussed in section 1.5.2. Symmetric rings could be used as inputs in this case. These two methods would not be adiabatic however, since energy would have to be expended to force the desired chirality in the magnetic element being used, introducing power dissipation into system. So, using these methods in complex gate configurations would not necessarily yield the system's lowest energy state.

Another method is the introduction of asymmetry to control the chirality of the input element. Subramani et al., reported this chirality control in individual rings by altering the shape and size of the holes [87]. The point of interest in our case, is to use the rings with the fastest switching time to establish inputs. Figure 50 shows rings with holes of 40 nm, offset 70 nm from the center of their respective

rings along the x-axis. For the same off-axis 2° field, depicted by direction of the arrow in the figure, the resulting chirality is shown. The reversal mechanics are similar to the case of individual disks, where two domain walls forms at both edges of with one swallowing the other in pac-man fashion. We see that location of the hole determines the chirality of the magnetization with a left justified hole producing an anti-clockwise chirality, and a right justified hole producing a clockwise chirality. Likewise, Figure 51 shows similar rings with holes offset 70 nm from the center along the y-axis. For of an off-axis 87° field, a top justified hole produces an anti-clockwise chirality, and a bottom justified hole produces a clockwise chirality.
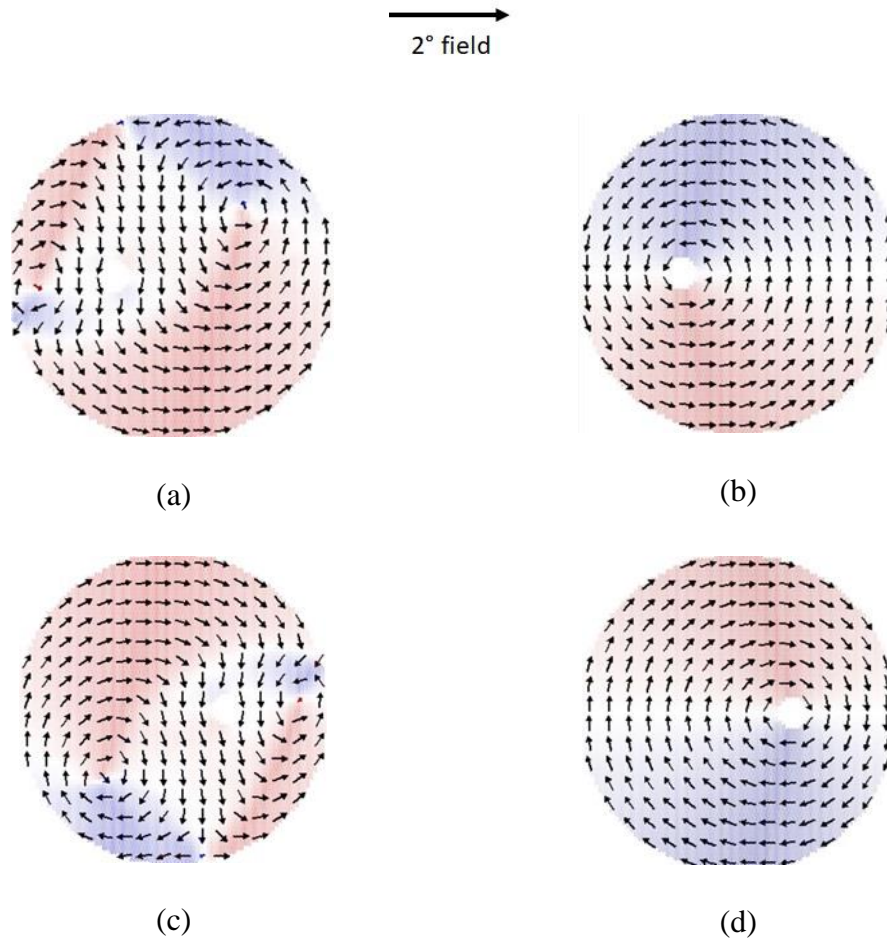
Figure 50 Reversal processes and remanence for rings with 40 nm holes offset by 70 nm along x-axis.

(a)

(b)

(c)

(d)
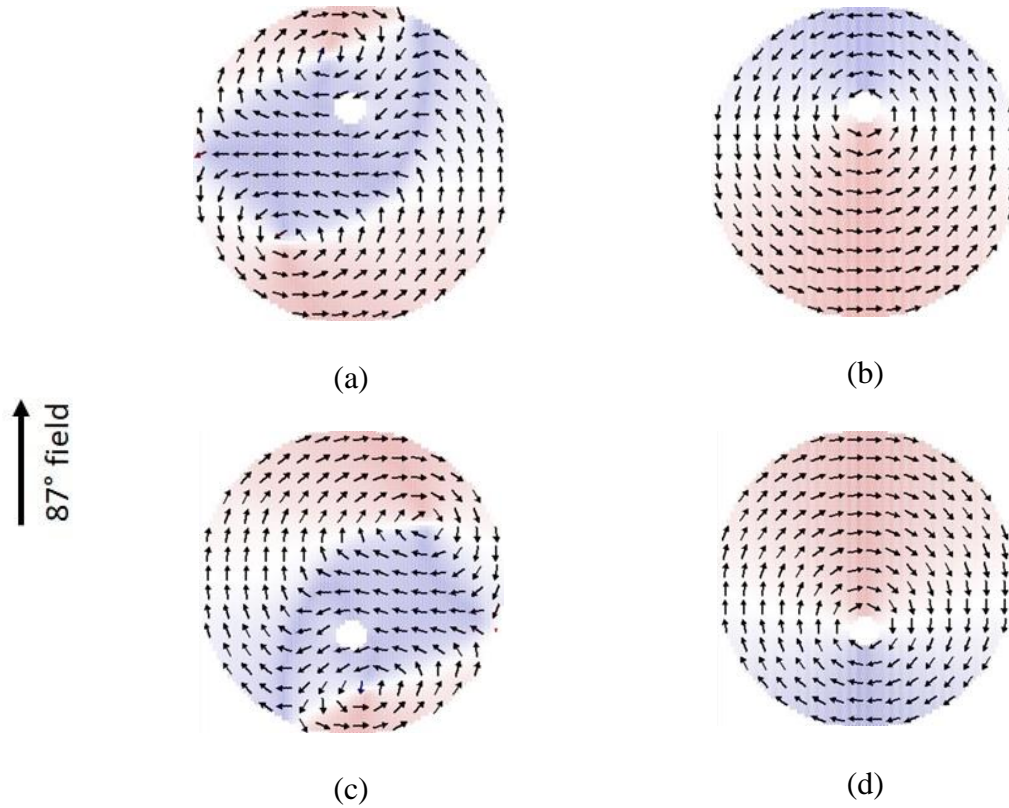
Figure 51 Reversal processes and remanence for rings with 40 nm holes offset by 70 nm along y-axis.

The applied field is in the axis of the hole offset; hence we see the resulting chirality of the ring for that particular field. It is important to note though, that since anisotropy has been intentionally introduced, the dynamics of the reversal process could be different when a field in a different axis from the offset is applied. This is because there is now a preferred direction for the magnetic moments to curl within the ring.

5.2   Asymmetric Majority Gates

Using asymmetric rings as inputs, a mixed element gate was simulated. Three 400 nm asymmetric rings with 40 nm holes were used as inputs, and a symmetric 400 nm ring with a 100 nm

hole was used as output. We see in Figure 52 that the inputs resolve themselves into their vortex states first before the output ring, resolves its own.

Input 2

2° field

Input 1

Input 3

(a)

Input 2

2° field

Input 1

Input 3

(b)
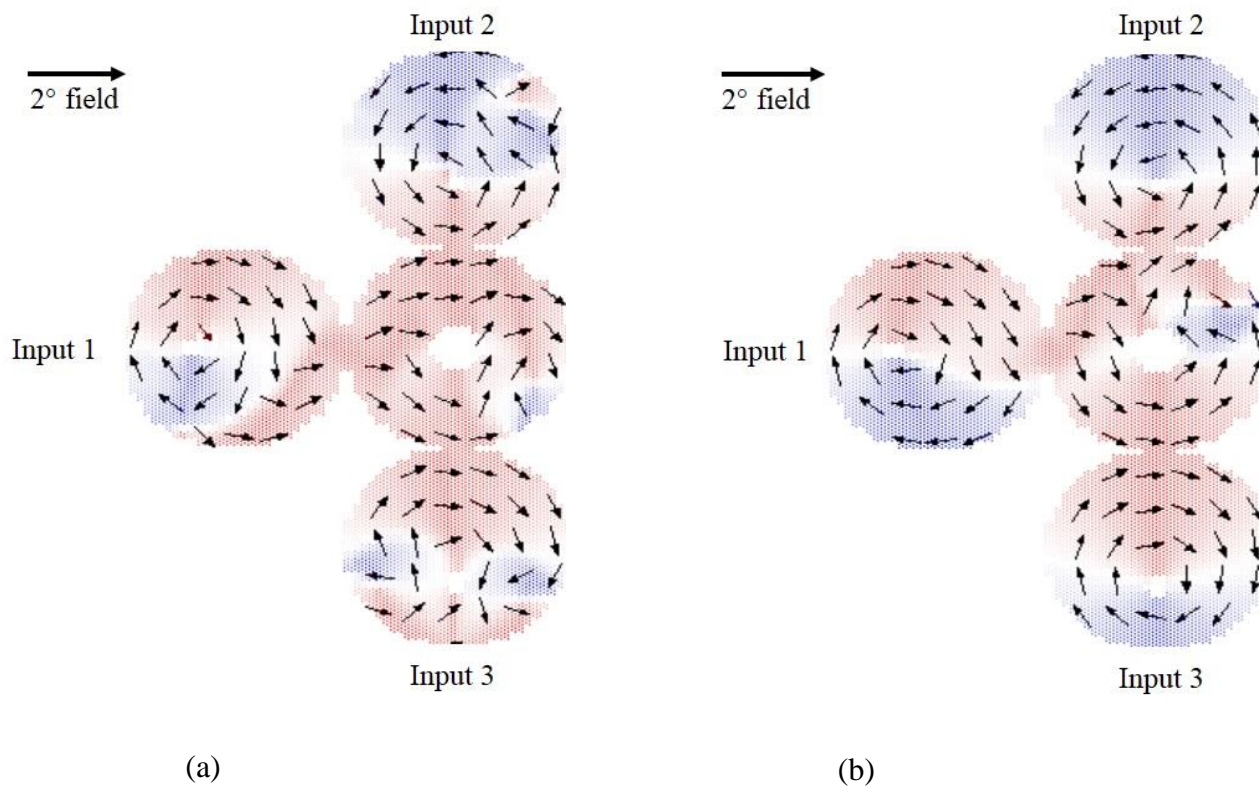
Figure 52 The reversal process for a majority gate. In (b), the inputs have already resolved their states before the domain of the output ring begins to migrate.

Immediately, we see that input 1's chirality is not the same as when it was individually undergoing the reversal process in Figure 49A, 49B. This shows that this form of asymmetry, while capable of introducing preferential chirality in individual rings, is not strong enough to dominate the ring's reversal mechanics when interaction with other elements is present. Nevertheless, in Figure 53A,

this mixed ring configuration does achieve its lowest energy state. Another gate configuration with different inputs was simulated and in Figure 53B. The holes of inputs 2 and 3 have been moved to the upper part of their respective rings, but still offset 70 nm from the center. The result is once again a system where the output ring is correlated with the majority magnetization of inputs 2 and 3. Additionally, one can see a vortex core present in input 1 in Figure 53B, likely due to large area available for a vortex to form and rotate away from the hole. Usually, the vortex should be centered around the hole as is the case in the symmetric and asymmetric rings previously discussed. However, here it is clearly offset from the hole and settled in the center of the ring.

(a)   (b)
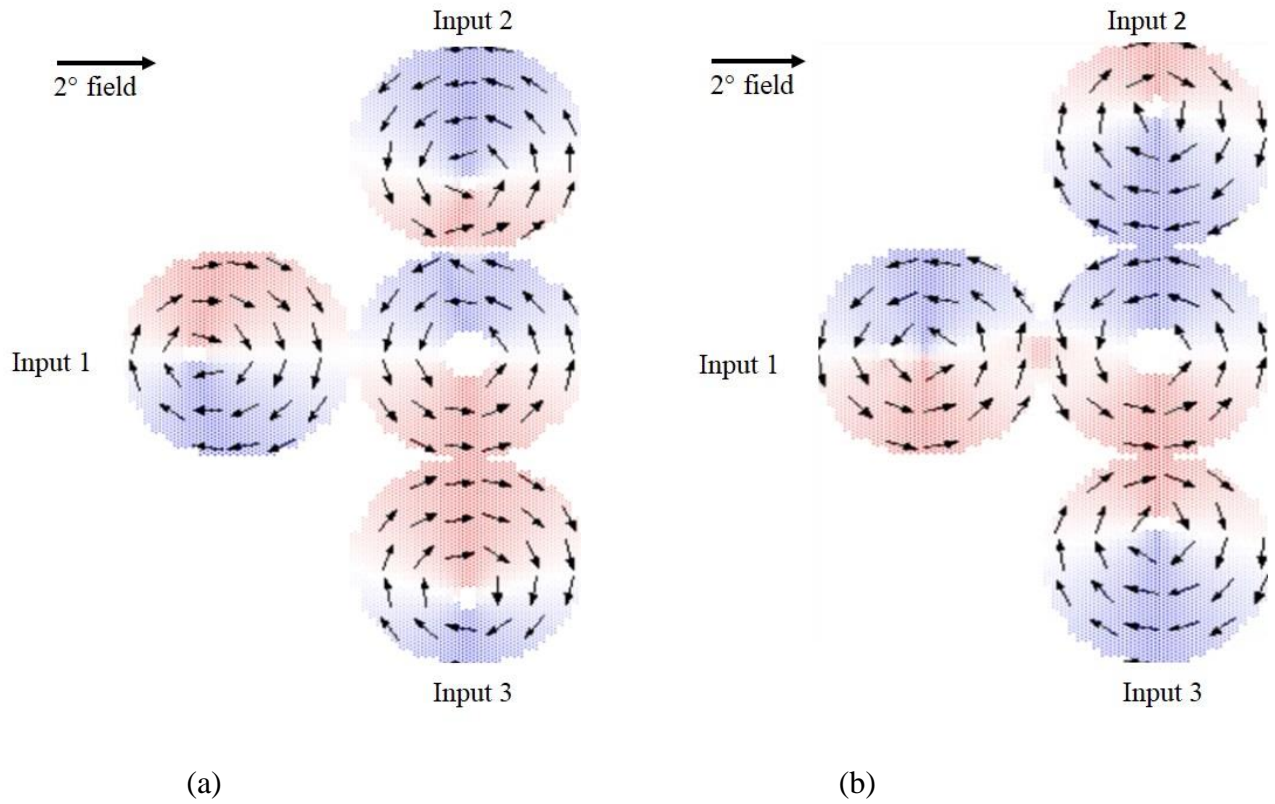
Figure 53 Gate end state for two different sets of inputs.

5.3   Gate Fan out

An essential aspect of any logic gate is its fan out. In this case, this is the number of rings that can be placed at the output ring and used to propagate the gate output signal down the line. The configuration shown in Figure 54 and Figure 55 successfully settled into its lowest energy state. It consists of a central disk, and an output chain of rings of aspect ratio 4 (100 nm holes). As a majority chirality is establishing itself at the inputs, the output rings begin switching. The resulting magnetization at the first output ring represents

$$Input\ 2 \cdot Input\ 3 = Logic\ '1',$$

the logical AND function, while the second output ring holding the opposite magnetization, represents the logical NAND function

$$\overline{(Input\ 2\ \cdot Input\ 3)} = Logic\ '0'$$
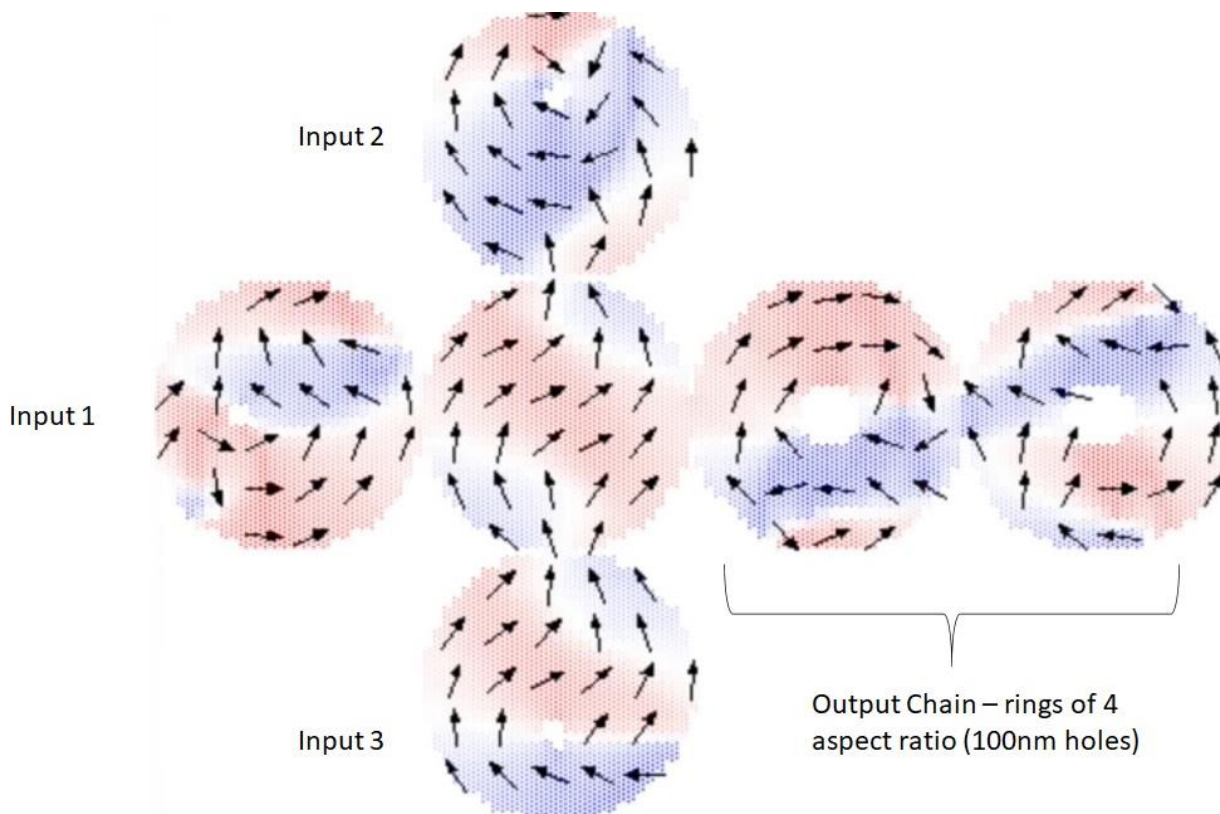
Figure 54 Majority gate during the magnetization reversal.

In this particular configuration, the central disk's demagnetizing field strongly interacts with the demagnetizing fields of the input rings. These rings are not too far from being disks themselves since their holes are not quite large enough to remove the entire vortex core. That being said, by the nature of the strong interactions of the demagnetizing fields, the disk takes a significant amount of simulation time to finally resolve its vortex with total simulation time for this configuration being in excess of 96 hours.
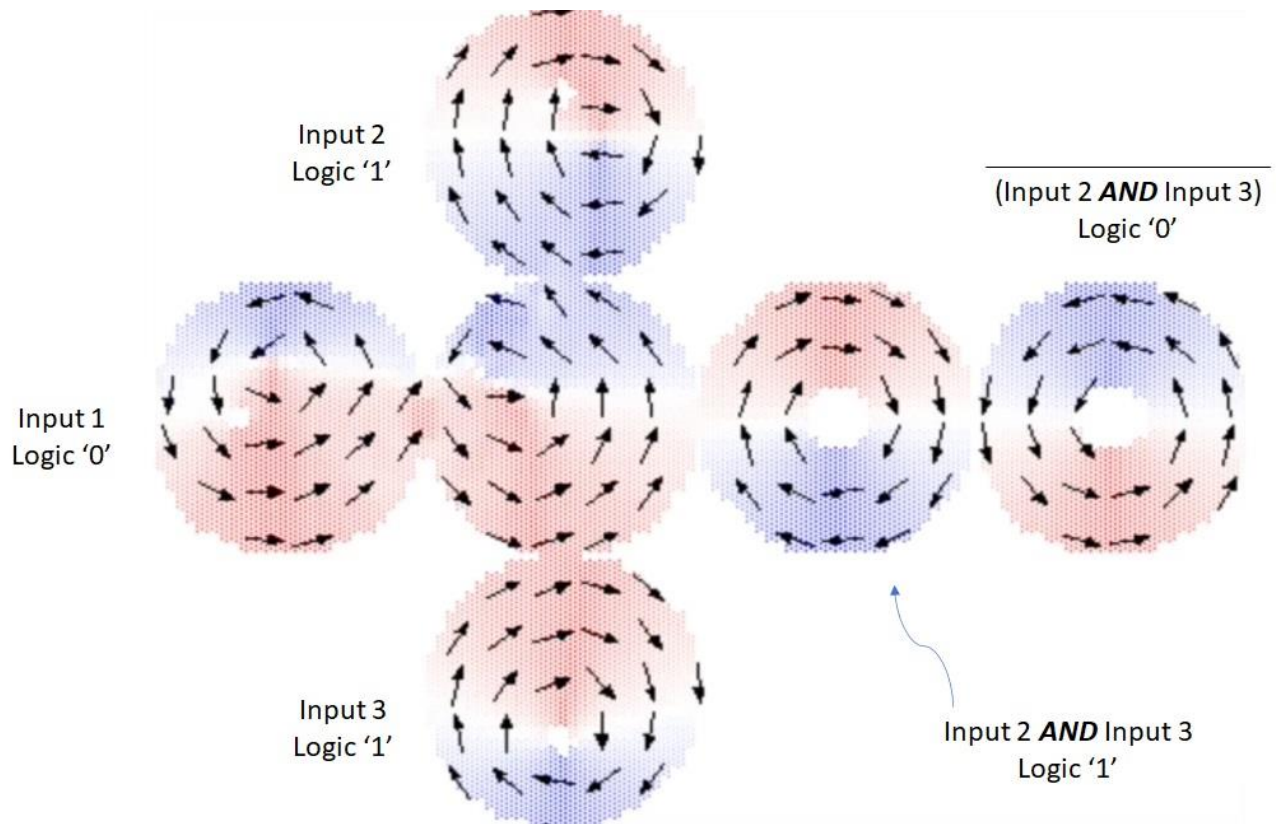
Figure 55 With inputs decided, the output chain resolve their vortex states. The central disk then follows.

It important to state that this is just one demonstration of a gate configuration settling into its lowest energy state for a given applied field. There are other possible configurations that could employ the same elements in different locations, and possibly result in different reversal processes as a function of the applied field.
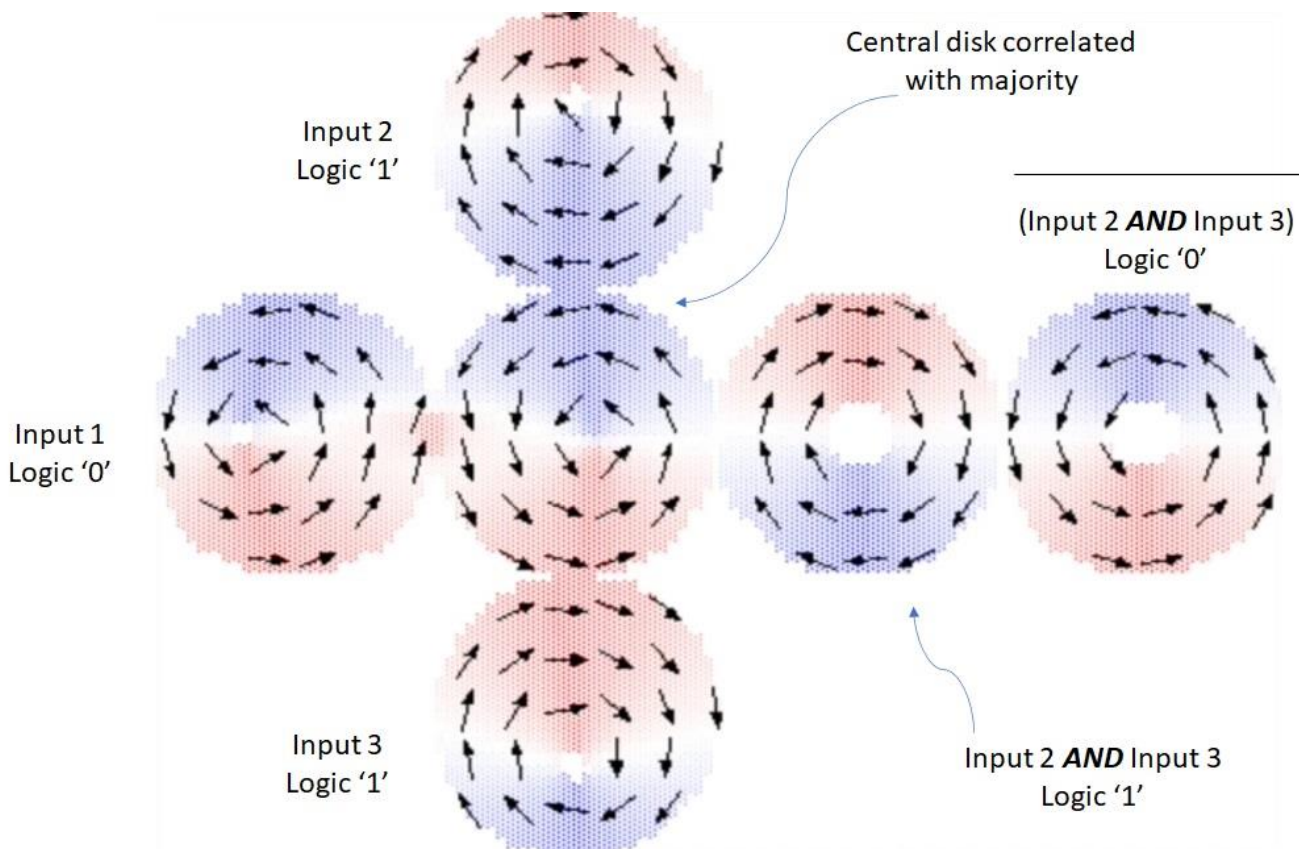
Figure 56 End states of the majority gate. The two rings the output chain is in correlation with the central disk, which is in correlation with the majority chirality of the inputs.

VI. Fabrication and Characterization of Circular Magnetic Elements

6.1   Fabrication Techniques

For the sizes being considered here, a suitable method of fabrication is needed. Conventional lithography is limited to feature sizes $< 2\ \mu m$ and Extreme Ultraviolet Lithography capabilities are few and far between [88]. The only viable fabrication method then is Electron-Beam Lithography (EBL).

6.2   Electron Beam Lithography

In this form of lithography, electrons emitted from a source are driven toward a sample to expose a sensitive polymer such as Poly-methyl-methacrylate (PMMA). The source emits electrons usually through one of two methods. The first is Thermionic emission (TE) which uses heat to excite electrons to higher energies by the Boltzmann relationship

$$E = K_B \cdot T$$

where K_B is the Boltzmann constant, 8.617×10^{-5} electron-volts per kelvin, and T is temperature. The emitted electrons can reach the vacuum energy which is the energy required to free them from the surface of the source. A common application employing this type of emission is Electron Beam Evaporation, where a tungsten wire emits a broad beam of electrons used to melt material in a crucible for deposition of thin film materials. This broadness of the beam though is detrimental in lithographic processes where a precise and narrow beam is required to exposed specific areas of a sample. The other method is Field emission (FE) which uses a large bias to excite electrons from a source, usually an ultra-sharp tungsten tip. The large electric field imparts enough energy to allow electrons near the tip surface to escape, although the process is not as stable as TE. FE is common in electron microscopy

which require narrow beams not at high temperature. The combination of these methods, however, is suitable for EBL as they can provide a focused electron source which can remain stable for extended periods of time since the heat ensures the source does not degraded in the presence of residual gases. The emitted beam is directed toward the sample surface with the help of beam deflectors located in a column under vacuum. These deflectors could be electrostatic or magnetic in nature and they serve to focus the beam through the aperture that is close to the sample surface. Figure 57 shows a schematic representation of a system combining the capabilities of Scanning Electron Microscopy (SEM) and EBL [89].
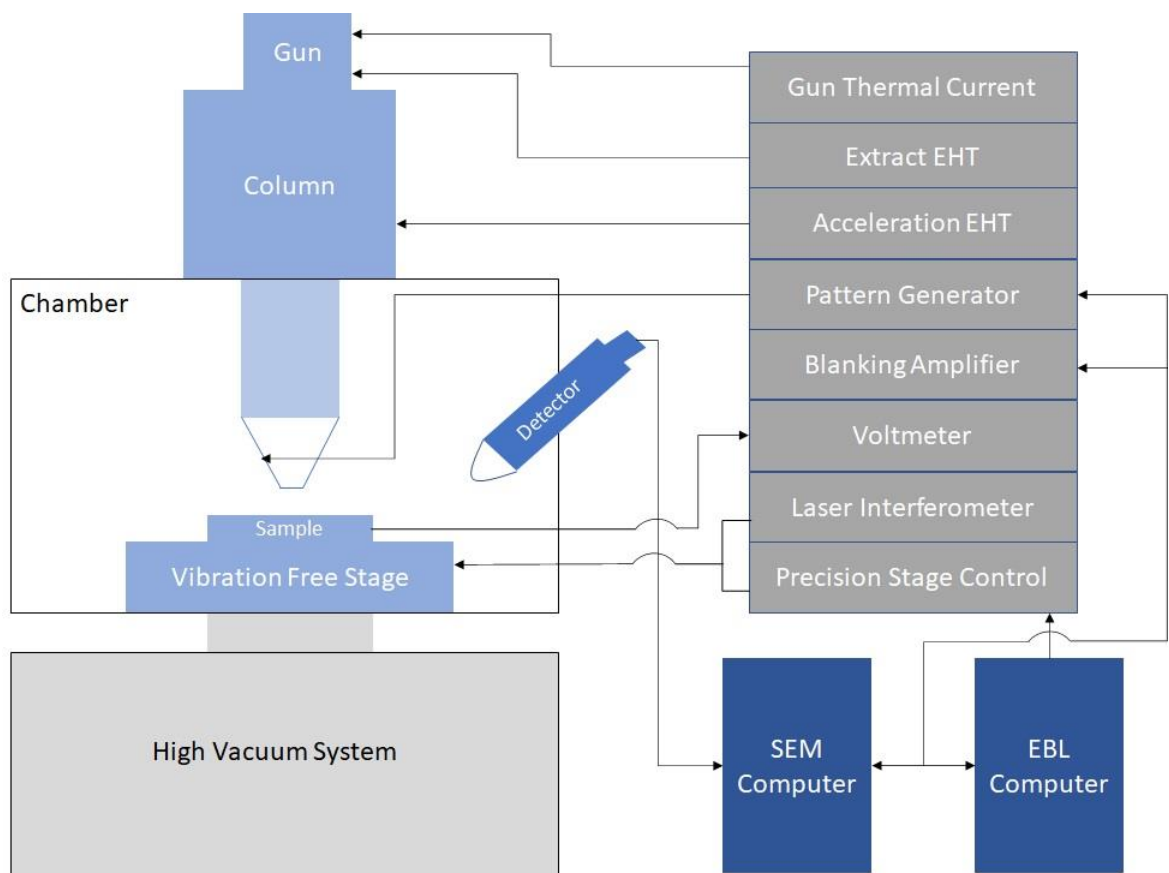
Figure 57 Schematic representation of EBL system.

6.1   Proximity Effect

When primary electron beams interact with PMMA, they also penetrate the substrate and backscatter into the resist, in essence, exposing the area of interest twice. This means features often overshoot their design dimensions as areas bordering the exposed regions also get exposed, since the scattering range of electrons is broad. The dose received by a feature is also affected by its proximity to other features in the design, which makes writing tightly packed features difficult. This is known as the 'proximity effect'. Additionally, primary electrons arriving at the resist surface also create secondary electrons which also expose the resist. However, their energy is low, and they only travel short distances making their contribution to the proximity effect small [89]. Figure 58 shows an attempt to write touching disks in single layer 495 PMMA C resist. The disks were ~394 nm in diameter and have blended together making any touching edges difficult to make out. The computer aided design file was in actuality scaled down to ~350 nm from the original 400 nm dimensions to compensate for the over-exposure.

In newer EBL systems, proximity correction algorithms assign varying dosages to different areas of the pattern to compensate for the over-exposure [90]. Also, double layered resist that produce an undercut pattern in the resist is used. This offers the advantage of easier lift-off of the deposited Permalloy. Figure 59 shows 1 µm Permalloy rings written in double-layer PMMA resist with proximity correction. While much reduced, the overlap of the rings is still present.
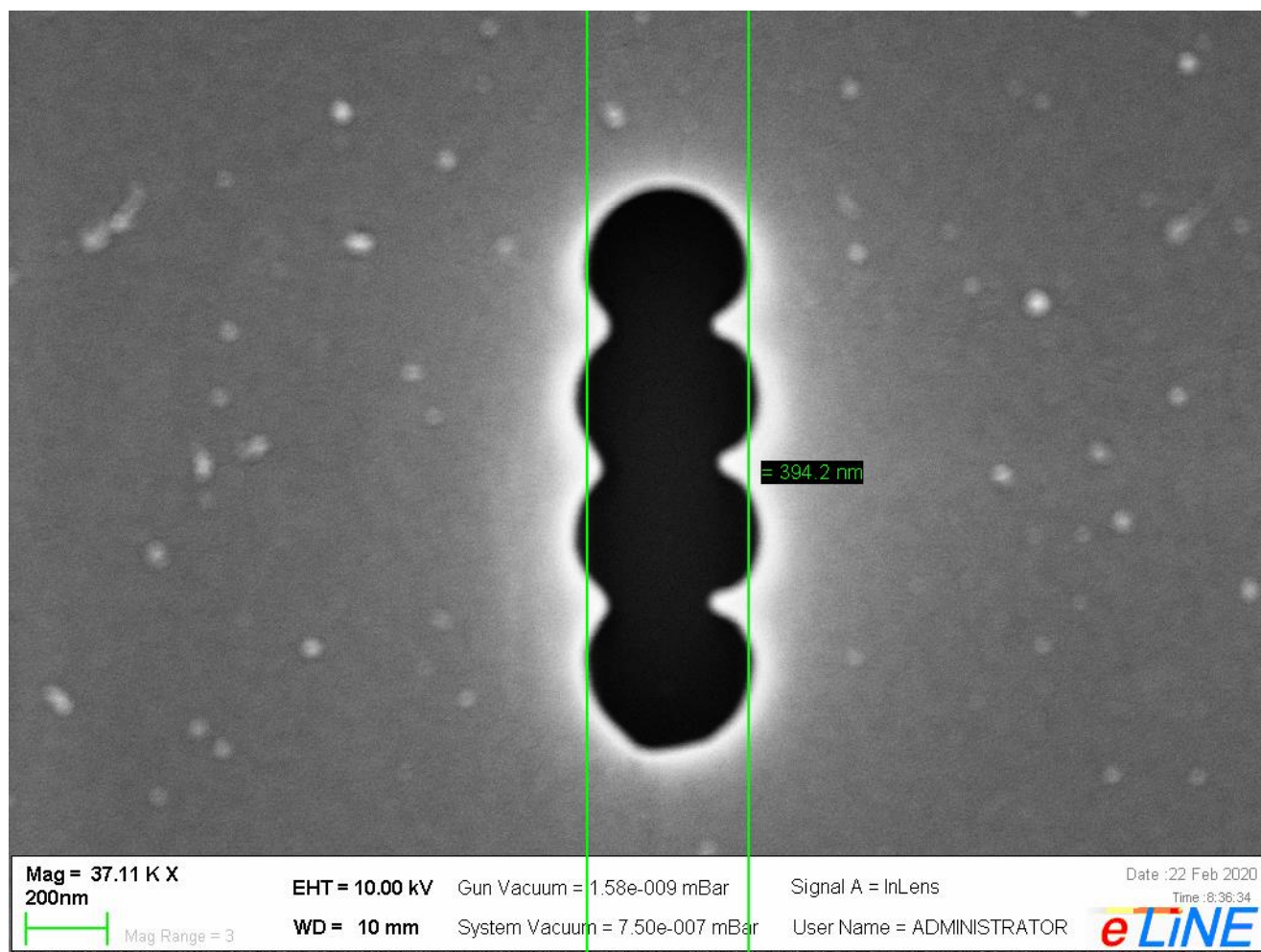
Figure 58 SEM image of disks written in single layer PMMA resist. Proximity effects cause overlapping. Target dimension was under designed for.
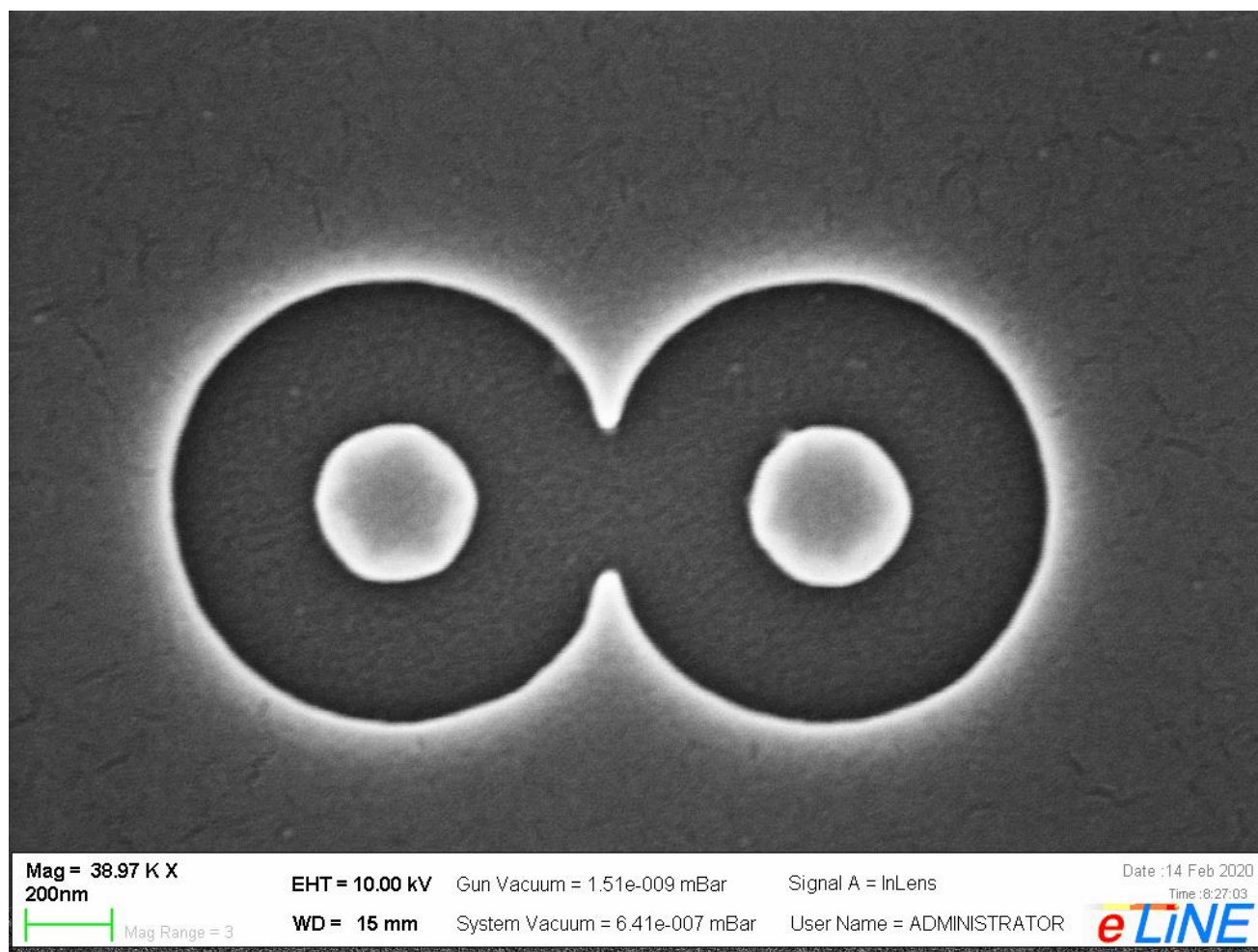
Figure 59 SEM image of rings written in double layer PMMA resist. Even with proximity correction, overlap is still present. Rings were 1 µm outer diameter, 400 nm inner diameter.

6.3   Challenges of Characterization

As discussed in chapter 4, simulations are crucial to understanding how the switching processes evolves in nanomagnets. Characterization techniques do offer useful information, however limited it is. The most viable method, Lorentz Microscopy is limited to static observations, but it is a non-invasive technique that shows domain structure [82,91]. The method involves using a Transmission Electron

Microscope (TEM) to scan a magnetic sample and determine the deflection electrons experience due to the Lorentz force given by

$$F = |e|(v \times \boldsymbol{B})$$

Here, $\boldsymbol{e}$ is the electron charge, $\boldsymbol{v}$, the electron velocity, and $\boldsymbol{B}$, the average of the magnetic induction along the electron beam. Magnetic contrast is present as the component of magnetic induction normal to the beam causes deflection of the electrons passing through the sample. The deflection angle is given as,

$$\beta_L = \frac{e\lambda t(\boldsymbol{B} \times \boldsymbol{n})}{h}$$

for λ, the electron wavelength, $\boldsymbol{t}$, the sample thickness, and $\boldsymbol{n}$, the unit vector parallel to the incident beam. Since it is proportional to the sample thickness, samples have to be fabricated on thin electron transparent membranes, usually ~100 nm of silicon nitride [82,92]. The angle's direction is also dependent on and perpendicular to the magnetization direction in the magnetic domain of interest.
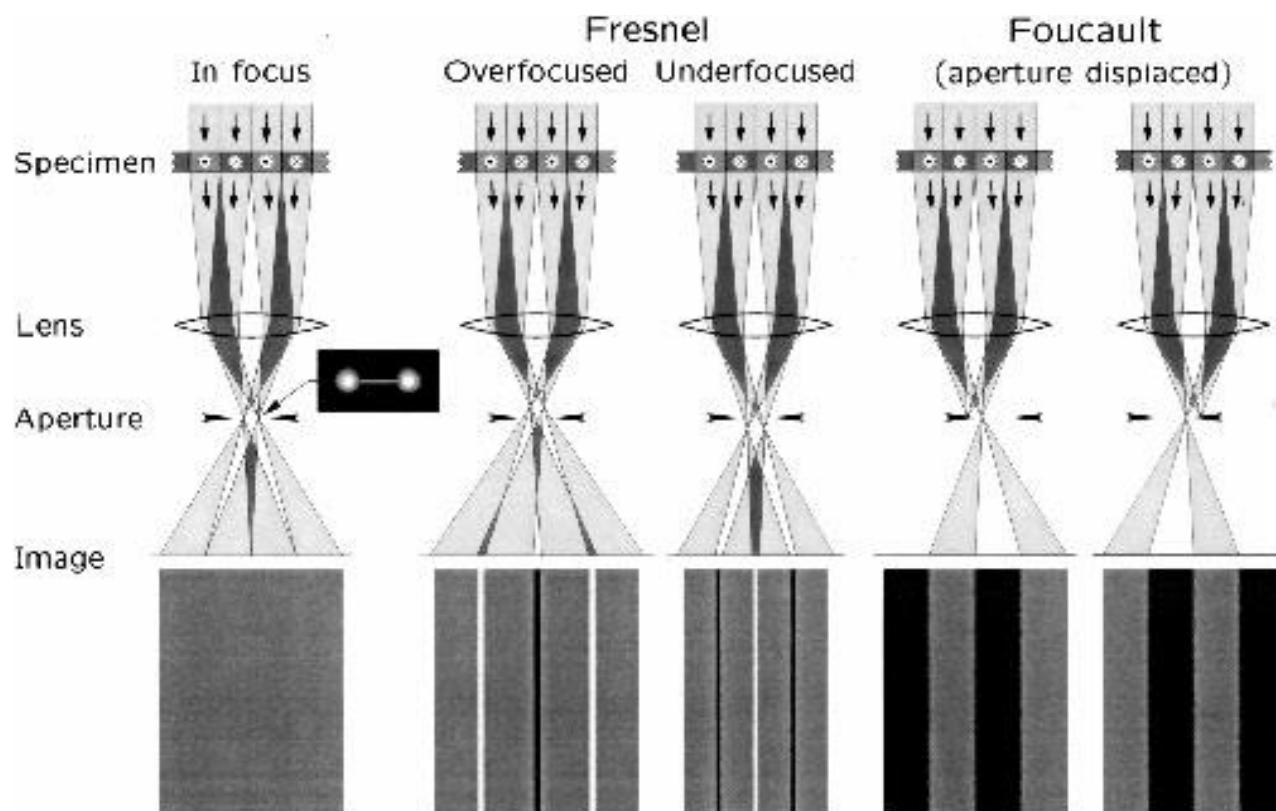
Figure 60 Schematic of ray diagram indicating the paths followed by electrons passing through a magnetic specimen, together with the contrast that would be seen in the image for the Fresnel and Foucault modes of L-TEM.

Figure 60 shows a schematic of two modes of Lorentz TEM. In Foucault mode, part of the diffraction pattern is blocked by an aperture being displaced in the same plane as the pattern. The magnetization is determined by the direction of electrons being deflected through the aperture or away from the it. The problem with this mode is that it depends on the position of the blocking aperture. Since the electron beam shifts in the presence of an applied field, it results in a shift from the location being imaged making in-situ magnetization analysis difficult. The addition of correction coils to shift the beam back to its original location can reduce this problem [82]. In the Fresnel mode, the sample can be over or under-focused to observe domain walls as alternating bright, dark, convergent, and

divergent lines, respectively. The Fresnel mode is mostly used for in-situ monitoring of magnetization reversal for a sample mounted on a magnetized stage and is limited to multi-domain structures. Figure 61 shows Fresnel mode images of 2 µm rings. Anti-clockwise chirality is interpreted as dark shading around the outer diameter and light shading around the inner diameter with rings of clockwise chirality follow the opposite shading.
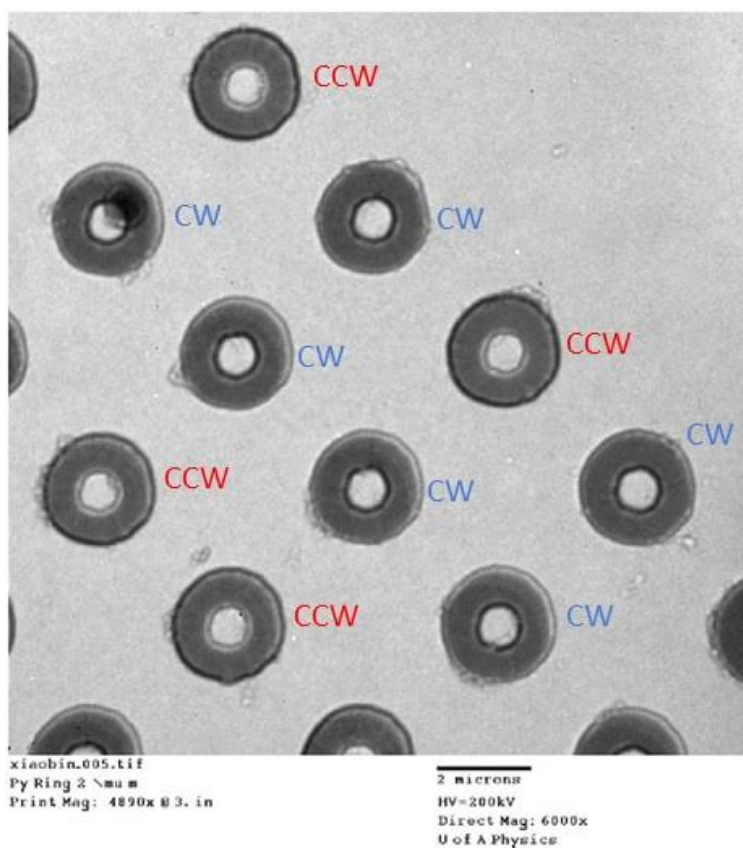
Figure 61 Image of anisotropic Permalloy rings. Counter-clockwise chirality is depicted as rings with dark shading around the outer circle and light shading around the inner circle. Rings of clockwise chirality follow the opposite shading. Courtesy of Xiaobin Zhu, University of Alberta, Canada

VII. Conclusion

The focus of this work has been to explore circular nanomagnets as candidates for room operable quantum cellular automata. The simulations done herein represent a first step into the exploration of these elements for the quantum computing regime. These elements exhibit stable ground states that can be used to represent logic and in the case of circular rings, an additional superposition state that can be used as a reset. We have shown that linear chains featuring touching elements undergo edge driven correlated switching and that they open up the possibility of realizing basic circuit elements such as a binary wire, or an elementary NOT gate. When in contact, these elements switch in pairs, the aspect ratio playing significant role in shaping their switching mechanics. Fine control of the direction of switching in linear chains with respect to outward → inward or inward → outward switching is still a point to be explored. However, unidirectionality of the switching process was shown to be possible given the right mix of elements.

Constructing a complex gate from the simulated elements was also shown to be possible, albeit much is left to be investigated. Introducing asymmetry into the system to implement inputs could be a possible path forward. The mixed aspect ratio elements used in the gate configuration all managed to resolve their vortex states. As there are a plethora of possible configurations employing varying elements and field clocking schemes, the opportunity to realize robust gates that can outperform the current state of the art is evident.

However, much remains to be done before a functional prototype can be conceived. The realization of stable inputs, efficient and robust enough to maintain their status without fluctuation is one to be solved. The limiting factor of the magnetic correlated volume also must be considered in the quest to construct complex gates with steady reproducibility. Synthesis and characterization of

elements using currently available techniques must also be optimized. Of course, it goes without saying that as more advanced systems are developed, problems such as the proximity effect can be mitigated to create high quality samples for prototyping. The avenue toward quantum computing is narrow, even more so for room operable quantum computing, not least because few options that fulfill all the required criteria exist. Magnetic QCA are one such option to explore as the impetus to move toward a new form of computing becomes ever more present.

CITED LITERATURE

1.   Schor, D. 'VLSI 2018: Samsung's 8nm 8LPP, A 10nm Extension,' *WikiChip Fuse*, 2018. [Online]. Available: https://fuse.wikichip.org/news/1443/vlsi-2018-samsungs-8nm-8lpp-a-10nm-extension/ [Accessed: 10-April-2020].

2.   Schor, D, 'TSMC Announces 6-Nanometer Process,' *WikiChip Fuse*, 2019. [Online]. Available: https://fuse.wikichip.org/news/2261/tsmc-announces-6-nanometer-process/ [Accessed: 10-April-2020].

3.   Tyson, M., 'Intel 10nm density is 2.7X improved over its 14nm node,' *Hexus,* 2018. [Online]. Available: https://hexus.net/tech/news/cpu/119699-intel-10nm-density-27x-improved-14nm-node [Accessed: 10-April-2020].

4.   ---. 'Process Integration Devices and Structures (PIDS)'. *International Technology Roadmap for Semiconductors*, 2011. [Online]. Available: http://www.itrs.net/Links/2011ITRS/Home2011.htm. [Accessed: 10-April-2020].

5.   Haron, N. Z., Hamdioui, S., "Why is CMOS scaling coming to an END?," 3rd Int. Design and Test Work. pp. 98–103, 2008.

6.   Cutress, I., Shilov, A., 'GlobalFoundries Stops All 7nm Development: Opts to Focus on Specialized Processes'. *AnandTech*, 2018. [Online] Available: https://www.anandtech.com/show/13277/globalfoundries-stops-all-7nm-development. [Accessed: 10-April-2020].

7.   Horowitz, M., Grumbling, E., Quantum computing: progress and prospects. Washington, DC: The National Academies Press, 2019.

8.   Copeland, R., Dahl, D., Ewald, B., 'An Introduction to Quantum Computing', Dwave Quantum Computing Lecture Series. Chicago, 4 Oct. 2018.

9.   Boixo, S., Isakov, S., Smelyanskiy, V., Babbush, R., Ding, N., Jiang, Z., Bremmer, J., Martinis, J., Neven, H., 'Characterizing quantum supremacy in near-term devices', *Nat. Phys.*, vol. 14, pp. 595-600, 2018.

10.   Bertsimas, D., Tsitsiklis, J., 'Simulated Annealing', *Stat. Sci.*, vol 8, no. 1, pp. 10–15, 1993.

11.   Roth, C. H., Fundamentals of Logic Design, 6th ed, Stamford: Cengage Learning 2020.

12.   Parsons, D. F., 'Possible Medical and Biomedical Uses of Quantum Computing' *Neuroquantology.*, vol. 9, no. 3, 2011.

CITED LITERATURE (continued)

13.   Solenov, D., Brieler, J., Scherrer, J., 'The Potential of Quantum Computing and Machine Learning to Advance Clinical Research and Change the Practice of Medicine' *Mo Med*, vol. 115, no. 5, pp. 463–467.

14.   Arute, F., Arya, K., Babbush, R., Bacon, D., Bardin, J., 'Quantum supremacy using a programmable superconducting processor', *Nature*, vol. 574, pp. 505–511, 2019.

15.   Pednault, E., Gunnels J. A., Nannicini, G., Horesh, L., Wisnieff, R., 'Leveraging Secondary Storage to Simulate Deep 54-qubit Sycamore Circuits. IBM T.J Watson Research Center, Yorktown, New York, 2019.

16.   Montecino, V., 'History of Computing', 2010. [Online]. Available: http://mason.gmu.edu/~montecin/computer-hist-web.htm. [Accessed: 10-Mar-2020].

17.   McFadden, C., 'The origin of the term computer bug', *Interesting Engineering*, 2018. [Online]. Available: https://interestingengineering.com/the-origin-of-the-term-computer-bug/ [Accessed: 10-Mar-2020].

18.   Lent, C. S., Tougaw, D., Porod, W., Bernstein, G. H., 'Quantum Cellular Automata', *Nanotechology., vol. 4*, pp. 49–57, 1993.

19.   Macucci, M., 'Quantum Cellular Automata: Theory, Experimentation and Prospects. The Concept of Quantum-Dot Cellular Automata, London: Imperial College Press. 2006.

20.   Bernstein, G. H., Bazan, G., Chen, M., Lent, C. S., Merz, J. L., Orlov, A., Porod, W., Snider, G. L., Tougaw, D., 'Practical issues in the realization of quantum-dot cellular automata'. *Superlattices and Microstruct.*, vol. 20, no. 4, pp. 447–459, 1996.

21.   Liu, W., Swartzlander, E. E., O'Neil, M., Design of semiconductor QCA systems. London: Artech House Publishers, 2013.

22.   Sridharan, K., Vikramkumar, P., Design of arithmetic circuits in quantum dot cellular automata nanotechnology. Switzerland: Springer International, pp. 47-82, 2015.

23.   Singh, G., Sarin, R., Raj, B., 'A Review of Quantum-Dot Cellular Automata Based Adders', *Int. J. Hybrid Inf. Technol., vol. 10, no.* 4, pp. 41–58 2017.

24.   Amir, F., Benny, T., 'New Design for Quantum Dots Cellular Automata to Obtain Fault Tolerant Logic Gates' *J. Nanopart. Res.*, vol. *3*, 27–37. 2001.

25.   Walus, K., Dysart, T., Jullien, G., Budiman, R., 'QCADesigner: A Rapid Design and Simulation Tool for Quantum-Dot Cellular Automata', *IEEE Trans. Nanotechnol., vol. 3, no.* 1, pp. 26–31, 2004.

CITED LITERATURE (continued)

26.   Ahmad, P.Z., Quadri, S., Ahmad, F., Bahar, A. N., Wani, G. M., Tantary, S. M., 'A novel reversible logic gate and its systematic approach to implement cost-efficient arithmetic logic circuits using QCA' *Data Brief,* vol. *15*, pp. 701–708, 2017

27.   Namita, Sasamal, T. N., 'Sequential circuit design using quantum-dot cellular automata', *Energy Procedia.*, vol. *117*, pp. 442–449, 2017.

28.   ---, Walus Lab, 'QCA Designer'. University of British Colombia, 2015. [Online]. Available: https://waluslab.ece.ubc.ca/qcadesigner/ [Accessed: 19-April-2019]

29.   Blundell, S., <u>Superconductivity, A Very Short Introduction</u>. New York: Oxford University Press, 2009

30.   Likharev, K. K., 'Superconducting weak links', *Rev. Mod. Phys.*, vol. 51, no. 1, pp. 101-159.

31.   Baselmans, J. J. A., Morpurgo, A. F., van Wees, B. J., Klapwijk, T. M., 'Reversing the direction of the supercurrent in a controllable Josephson junction', *Nature*, vol. 397, pp. 43-45, 1999.

32.   Dubos, P., Courtois, H., Pannetier, B., Wilhelm, F.K., Zaikin, A. D., Schön, G., 'Josephson critical current in a long mesoscopic S-N-S junction', *Phys. Rev. B*, vol. 63

33.   Martinis, J. M., Osborne, K., 'Superconducting Qubits and the Physics of Josephson Junctions', *National Institute of Standards and Technology*, Boulder, Colorado. [Accessed: 16-Mar-2018].

34.   Maassen van den Brink, A., Berkley, A. J., Yalowsky, M., 'Mediated tunable coupling of flux qubits', *New J. Phys.*, vol. 7, 2005.

35.   Blais, A., Maassen van den Brink, A., Zagoskin, A. M., 'Tunable coupling of superconducting qubits' *Phys. Rev. Lett.*, vol. 90, no. 12, 2003.

36.   Niskanen, A. O., Harrabi, K., Yoshihara, F., Nakamura, Y., Lloyd, S., Tsai, J. S., 'Quantum coherent tunable coupling of superconducting qubits', *Science*, vol. 316, no. 5825, pp.723-726, 2007.

37.   ---, Dwave Systems Inc, [Online]. Available: https://www.dwavesys.com. [Accessed: 9-October-2018].

38.   ---, IBM Corporation. [Online]. Available: https://www.ibm.com/quantum-computing. [Accessed: 9-April-2019].

39.   Johnson, S., 'Google's Sycamore beats top supercomputer to achieve quantum supremacy', *Big Think*, 2019. [Online]. Available: https://bigthink.com/technology-innovation/google-quantum-computer [Accessed: 30-October-2020].

CITED LITERATURE (continued)

40. Bunyk, P., Likharev, K., Zinoviev, D., 'RSFQ Technology: Physics and Devices', Int. J. of High Speed Electron Syst., *vol*. 11, *no*. 1, 2001.

41. Brock, D., 'RSFQ Technology: Circuits and Systems', Hypres Inc. [Accessed: 9-January-2020].

42. Lu, Y., Liu, M., Lent, C. S., 'Molecular quantum-dot cellular automata: From molecular structure to circuit dynamics', *J. Appl. Phys., vol*. 102, 2007.

43. Jin, Z.: 'Fabrication and measurement of molecular quantum cellular automata (QCA) device.' Ph.D. thesis, University of Notre Dame, Notre Dame, 2006.

44. Ardesi, Y., Pulimeno, A., Graziano, M., Riente, R., Piccinini, G., 'Effectiveness of molecules for quantum cellular automata as computing devices', *J. Low Power Electron. Appl.*, *vol*. 8, *no*. 24, 2018.

45. Li, Z., Beatty, A., Fehlner, T., 'Molecular QCA Cells. 1. Structure and functionalization of an unsymmetrical dinuclear mixed-valence complex for surface binding', *Inorg. Chem.*, *vol*. 42, *no*. 18, pp. 5707-5714, 2003.

46. Qi, H., Sharma, S., Li, Z., Snider, G., Orlov, A., Lent, C. S., Fehlner, T., 'Molecular quantum cellular automata cells. Electric field driven switching of a silicon surface bound array of vertically oriented two-dot molecular quantum cellular automata', *J. Am. Chem. Soc.*, *vol*. 125, pp. 15250-15259, 2003.

47. Lu, Y., Lent, C. S., 'Self-doping of molecular quantum-dot cellular automata mixed valence zwitterions' *Phys. Chem.*, *vol*. 13, pp. 14923-14926, 2001.

48. --, IBM Archives, IBM Corporation. Available: https://www.ibm.com/ibm/history/index.html [Accessed: 1-April-2019].

49. Zhu, J. G., Zheng, Y., Prinz, G. A., 'Ultrahigh density vertical magneto-resistive random-access memory', *J. Appl. Phys.*, *vol*. 87, *no*. 9, pp. 6668–6673, 2000.

50. Orlov, A., Imre, A., Csaba, G., Ji, L., Porod, W., Bernstein, G. H., 'Magnetic quantum-dot cellular automata: Recent developments and prospects. *J. Nanoelectron. and Optoelectron.*, *vol*. 3, *no*. 1, pp. 55–68, 2008.

51. Bernstein G. H., Imre, A., Metlushko, V., Orlov, A., Zhou, L., Ji, L., Porod, W., 'Magnetic QCA systems', *Microelectronics J.*, *vol*. 36, *no*. 7, pp. 619–624, 2005.

52. Allwood, D. A., Xiong, G., Faulkner, C. C., Atkinson, D., Petit, D., Cowburn, R. P., 'Magnetic domain wall logic', *Science*, *vol*. 309, 2005.

CITED LITERATURE (continued)

53.   Das, J., Alam, S. M., Bhanja, S., 'Low power magnetic quantum cellular automata realization using magnetic multi-layer structures', *IEEE Trans. Emerg. Sel. Topics Circuits Syst., vol*. 1, *no*. 3, pp. 1–9, 2011.

54.   Ralph, D. C., Stiles, M. D., 'Spin transfer torques', *J. Magn. Magn. Mater.*, *vol*. 320, pp. 1190-1216, 2008.

55.   Shinjo, T., Okuno, T., Hassdorf, R., Shigeto, K., Ono, T., 'Magnetic vortex core observation in circular dots of Permalloy', *Science*, *vol*. 289, 2000.

56.   Cowburn, R. P., Welland, M. E., 'Room temperature magnetic quantum cellular automata', *Science*, *vol*. 287, *no*. 5457, pp. 1466–1468, 2005.

57.   Imrem A., Zhou, L., Orlov, G., Csaba, G., Bernstein, G. H., Porod, W., Methlushko, V., 'Application of mesoscopic magnetic rings for logic devices', *4th IEEE Conf. Nanotechnol.*, pp. 137-139 2004.

58.   Schnieder, M., Hoffman, H., Zweck, J., 'Lorentz microscopy of circular ferromagnetic Permalloy nano-disks', *Appl. Phys. Lett.*, *vol*. 77, *no*. 18, pp. 2909-2911, 2000.

59.   Vavassori, P., Grimsditch, M., Novosad, V., Methlushko, V., IIic, B., 'Magnetization switching in Permalloy square ring magnets', *J. Appl. Phys.*, *vol*. 93, *no*. 10, pp. 7900-7902, 2003.

60.   Fumagalli, L., Zohar, A., Methlushko, V., 'Micromagnetic simulation of switching mechanism in Permalloy square rings', *Int. Conf. on Electromagn. Adv. Appl.*, pp. 617-620, 2007

61.   Donahue, M. J., Porter, D. G., 'OOMMF User's Guide,Version 1.0,' Interagency Report NlST 6376. Available: http://math.nist.gov/oommf. [Accessed: 9-November-2018].

62.   Landau, L., Lifshitz, E., 'On the theory of the dispersion of magnetic permeability in ferromagnetic bodies', *Ukr. J. Phys.*, *vol*. 53, pp. 153-169, 1935.

63.   Gilbert, T. L., 'A phenomenological theory of damping in ferromagnetic materials', *IEEE Trans. Mag., Classics in Magnetics*, *vol*. 4, *no*. 6, pp. 3443-3449, 2004.

64.   Lakshmanan, M., 'The Fascinating World of Landau-Lifshitz-Gilbert Equation: An Overview', *Phil. Trans. R. Soc. A.*, *vol*. 369, pp. 1280-1300, 2011.

65.   Fähnle, M., Steiauf, D., Seib, J., 'The Gilbert equation revisited anisotropic and nonlocal damping of magnetization dynamics', *J. Phys. D: Appl. Phys.*, *vol*. 41, 2008.

CITED LITERATURE (continued)

66.   Krüger, B.: 'Current-Driven Magnetization Dynamics Analytical Modeling and Numerical Simulation'. Ph. D. thesis, University of Hamburg, Hamburg, 2011.

67.   D'Aquino, M.: 'Nonlinear Magnetization Dynamics in Thin Films and Nano-particles', Ph. D. thesis, University of Naples, "Federico II", Naples, 2004.

68.   Ferona, M. A.: 'Nonlinear and Chaotic Magnetization Dynamics in Single-domain Nano-particles and Exchange-couples Thin Films', Ph. D. thesis, University of Colorado, Colorado Springs, 2015.

69.   Filder, J., Schrefl, T., Tsiantos, V. D., Scholz, W., Suess, D., 'Micromagnetic Simulations of the Magnetic Switching Behavior of Mesoscopic and Nanoscopic Structure', _J. Comput. Phys._, EMRS Conference pp. 18-41, 2001.

70.   Coey, J. M., Magnetism and Magnetic Materials, Cambridge: Cambridge University Press, 2010.

71.   Smith, D. O., 'Anisotropy in Permalloy Films', _J. Appl. Phys., vol_. 30, no. 4, pp. 264-265, 1959.

72.   Imre, A., Csaba, G., Bernstein, G. H., Porod, W., Metlushko, V., 'Investigation of shape-dependent switching of coupled nanomagnets', _Superlattices and Microstruct., vol_. 34, pp. 513–518, 2003.

73.   Vavassori, P., Bovolenta, R., Methlusho, V., Illic, B., 'Vortex rotation control in Permalloy disks with small circular voids', _J. Appl. Phys., vol_. 99, 2006.

74.   Silva, J. H., Toscano, D., Sato, F., Coura, P. Z., Costa, B. V., Leonel, S. A., 'The influence of magnetic impurities in the vortex core dynamics in magnetic nano-disks', _J. Magn. Magn. Mater., vol_. 324, pp. 3083-3086, 2012.

75.   Cullity, B. D., Introduction to Magnetic Materials, Reading: Addison-Wesley Publishing, 1972.

76.   Morrish, A. H., Yu, S. P., 'Magnetic Measurements on Individual Microscopic Ferrite Particles Near the Single-domain Size', _Phys. Rev., vol_. 102, _no_. 3, pp. 670-673, 1956.

77.   Frei, E. H., Shtrikman, S., Treves, D., 'Critical Size and Nucleation Field of Ideal Ferromagnetic Particles', _Phys. Rev., vol_. 106, _no_. 3, pp. 446-455, 1957.

78.   Abo, G. S., Hong, Y., Park, J., Lee, J., Lee, W., & Choi, B. 'Definition of Magnetic Exchange Length' _IEEE Trans. Mag., vol_. 49 _no_. 8, pp. 4937-4939, 2013.

79.   Ladak, S., Walton, S. K., Zeissler, K., Tyliszczak, T., Read, D. E., Branford, W. R., Cohen, L. F., _New J. Phys., vol_. 14, 2012.

CITED LITERATURE (continued)

80.   Cowburn, R. P., Welland, M. E., 'Magnetic Switching and Anisotropy in Nanomagnets: The Influence of Size and Shape' *INTERMAG 2000 Digest of Technical Papers, IEEE Int. Magn. Conf.*, 2000.

81.   Bellitto, V.: Magnetic Force Microscopy: Basic Principles and Applications. In: <u>Atomic Force Microscopy – Imaging, Measuring, and Manipulating,</u> eds. Ferri, F. A., Pereira-da-Silva, M. A., Marega Jr., E., pp. 39-56, Intech, 2012.

82.   Hopster, H., Oepen, H. P. <u>Magnetic Microscopy of Nanostructures</u>. Berlin: Springer. 2005

83.   Jamalim, M., Lee, K. J., Yang, H. S., 'Metastable magnetic domain wall dynamics', <u>*New J. Phys.*</u>, *vol*. 14, 2012.

84.   Schneider, M., Hoffmann, H., Zweck, J., 'Lorentz Microscopy of Circular Ferromagnetic Permalloy Disks', <u>*J. Appl. Phys. Lett.*</u>, *vol*. 77, *no*. 18, pp. 2909-2911. 2000.

85.   Durowade, T., Metlushko, V., 'Micro-magnetic simulations of correlated switching in touching circular nano-magnetic elements', <u>*AIP Adv*</u>., *vol*. 10, *no*. 3, 2020.

86.   Welp, U., Vlasko-Vlasov, V. K., Crabtree, G. W., Hiller, J., Zaluzec, N., Metlushko, V., Ilic, B., 'Magnetization reversal in arrays of individual and coupled Co-rings', <u>*J. Appl. Phys.*</u>, *vol*. 93, *no*. 10, pp. 7056–7058, 2003.

87.   Subramani, A., Geerpuram, D., Bakaran, V., Friedlund, J., Metlushko, .V., 'Precise control of the vortex chirality in magnetic nano-rings with deliberately introduced asymmetry', *Physica C.*, *vol*. 437-438, pp. 293-298, 2006.

88.   D. Schor, 'ASML Starts NXE:3400C Shipment, But Supply Constraints Loom,' WikiChip Fuse, 2019. [Online]. Available: <u>https://fuse.wikichip.org/news/2794/asml-starts-nxe3400c-shipment-but-supply-constraints-loom/</u> [Accessed: 15-April-2020].

89.   Khodr, M.: '3D Electron Beam Lithography for Biomedical Applications'. Ph.D. thesis, University of Illinois at Chicago, Chicago, 2015

90.   Li, P., 'A Review of Proximity Effect Correction in Electron-beam Lithography', Department of Electrical and Computer Engineering, Auburn University, Auburn, 2015.

91.   --, Central Microscopy, University of Iowa. [Online]. Available: https://cmrf.research.uiowa.edu/transmission-electron-microscopy/ [Accessed:21-October-2018]

92.   Warot-Fonrose, B., 'Magnetic Imaging and Microscopy - Electron Microscopies.' Lecture presented at European School of Magnetism: New Experimental Approaches to Magnetism, Constanta, Romania, 2005.

APPENDICES

APPENDIX A

The following is a sample OOMMF code used for the simulations in this work. Comments are in preceded by #.

```
# MIF 2.1
# MIF Example File: disk.mif
# Material: Permalloy

# constant pi and μ0
set pi [expr {4*atan(1.0)}]
set mu0 [expr {4*$pi*1e-7}]

# for random generation of vectors
RandomSeed 1

#############################################################
# dimension in x,y,z axis, xy plane of view during simulation,
#  name of file - draw in another program and then import in bmp format
#  white in the field is nonmagnetic and black in the file is magnetic

    Specify Oxs_ImageAtlas:Mbuffer {
      xrange {0.000E-6 0.400E-6}
      yrange {0.000E-6 0.400E-6}
      zrange {0.000E-6 0.025E-6}
      image disk.bmp
      viewplane xy
      colormap {
         white nonmagnetic
         black magnetic
         }}

#############################################################
# Sets global atlas - multiple atlases can be under it
# Atlas being used is Mbuffer

    Specify Oxs_MultiAtlas:globalatlas {
     atlas :Mbuffer
     }
```

APPENDIX A (continued)

```
###########################################################
# Create a mesh - based on magnetostatic-exchange length
# which is sqrt[2A/{mu0*(Ms^2)}]

    Specify Oxs_RectangularMesh:mesh {
     cellsize {5e-9 5e-9 25e-9}
     atlas :globalatlas
    }
###########################################################
# Exchange Energy

    Specify Oxs_UniformExchange {
     A 13e-12
    }
###########################################################
# Anisotropy in permalloy in neglible

    Specify Oxs_UniaxialAnisotropy {
        K1 0.0
        axis {Oxs_RandomVectorField {
        min_norm 1.0
                    max_norm 1.0
        }}}
###########################################################
# External Field applied in x,y,z.
# Last number is the number of steps taken to reach field value - must be an integer

    Specify Oxs_UZeeman:extfield0 [subst {
     comment {Field values in Tesla; scale to A/m}
     multiplier [expr {1/$mu0}]
     Hrange {
          {  0.2     0.01     0        0       0     0   5}
          {    0       0      0      -0.2    -0.01   0   5}
          {  -0.2    -0 .01    0        0       0     0   5}
          {    0       0      0       0.2     0.01   0   5}
        }}]
###########################################################
# Demagnetization - does not accept any arguments
    Specify Oxs_Demag {}
```

APPENDIX A (continued)

```
###########################################################
# Solver,
# do_precess determines whether or not the precession term in the Landau-Lifshitz ODE # is used.
# Default value is 1.
# gamma_LL - gyromagnetic  ratio from literature
# alpha - damping factor
# Current density J and unit polarization direction mp are required. Positive J produces torque that
#  ends to align m towards mp. The default values for polarization, P, is 0.4

   Specify Oxs_SpinXferEvolve:evolver {
    do_precess 1
    gamma_LL 2.21e5
    alpha 0.0312
    start_dm 0.001
    mp {0 0 0}
    J 1e6
    P 0.4
   }


################################################################
# Time Driver used for simulation

   Specify Oxs_TimeDriver [subst {
    basename disk
    vector_field_output_format {binary 4}
    scalar_output_format %.15g
    evolver :evolver
    mesh :mesh
   stopping_dm_dt 0.001
   Ms { Oxs_AtlasScalarField {
     atlas :globalatlas
       default_value 0.0
     values {
             nonmagnetic 0
             universe 0
             magnetic   860e3  }  }}

   m0 { 0.2  0.01  0 }   # initial magnetization
   }]
```

APPENDIX A (continued)

```
#####################################################################
# Specifies graph and display for vectors

    Destination my_graph mmGraph
    Destination my_display mmDisp
####################################################################
#Specify what should be saved how often to update

    Schedule DataTable my_graph Step 1
    Schedule Oxs_TimeDriver::Magnetization my_display Stage 1
Schedule Oxs_TimeDriver::Magnetization my_display Step 1
```

APPENDIX B

License Number	4818371175672
License date	Apr 29, 2020
Licensed Content Publisher	Elsevier
Licensed Content Publication	Microelectronics Journal
Licensed Content Title	Magnetic QCA systems
Licensed Content Author	G.H. Bernstein,A. Imre,V. Metlushko,A. Orlov,L. Zhou,L. Ji,G. Csaba,W. Porod
Licensed Content Date	Jul 1, 2005
Licensed Content Volume	36
Licensed Content Issue	7
Licensed Content Pages	6
Start Page	619
End Page	624
Type of Use	reuse in a thesis/dissertation
Portion	figures/tables/illustrations
Number of figures/tables/illustrations	2
Format	electronic
Are you the author of this Elsevier article?	No
Will you be translating?	No
Title	Micromagnetic Simulations of Circular Nano-magnets for Room Operable Quantum Cellular Automata
Institution name	University of Illinois at Chicago
Expected presentation date	May 2020
Portions	Figures 1 and 5
Requestor Location	Tejumade Durowade 1831 218th Pl CHICAGO HEIGHTS, IL 60411 United States Attn: Tejumade Durowade
Publisher Tax ID	98-0397604
Total	0.00 USD

APPENDIX B (continued)

INTRODUCTION

1. The publisher for this copyrighted material is Elsevier. By clicking "accept" in connection with completing this licensing transaction, you agree that the following terms and conditions apply to this transaction (along with the Billing and Payment terms and conditions established by Copyright Clearance Center, Inc. ("CCC"), at the time that you opened your Rightslink account and that are available at any time at http://myaccount.copyright.com).

GENERAL TERMS

2. Elsevier hereby grants you permission to reproduce the aforementioned material subject to the terms and conditions indicated.

3. Acknowledgement: If any part of the material to be used (for example, figures) has appeared in our publication with credit or acknowledgement to another source, permission must also be sought from that source. If such permission is not obtained then that material may not be included in your publication/copies. Suitable acknowledgement to the source must be made, either as a footnote or in a reference list at the end of your publication, as follows:

"Reprinted from Publication title, Vol /edition number, Author(s), Title of article / title of chapter, Pages No., Copyright (Year), with permission from Elsevier [OR APPLICABLE SOCIETY COPYRIGHT OWNER]." Also Lancet special credit - "Reprinted from The Lancet, Vol. number, Author(s), Title of article, Pages No., Copyright (Year), with permission from Elsevier."

4. Reproduction of this material is confined to the purpose and/or media for which permission is hereby given.

5. Altering/Modifying Material: Not Permitted. However figures and illustrations may be altered/adapted minimally to serve your work. Any other abbreviations, additions, deletions and/or any other alterations shall be made only with prior written authorization of Elsevier Ltd. (Please contact Elsevier at permissions@elsevier.com). No modifications can be made to any Lancet figures/tables and they must be reproduced in full.

6. If the permission fee for the requested use of our material is waived in this instance, please be advised that your future requests for Elsevier materials may attract a fee.

7. Reservation of Rights: Publisher reserves all rights not specifically granted in the combination of (i) the license details provided by you and accepted in the course of this

APPENDIX B (continued)

licensing transaction, (ii) these terms and conditions and (iii) CCC's Billing and Payment terms and conditions.

8. License Contingent Upon Payment: While you may exercise the rights licensed immediately upon issuance of the license at the end of the licensing process for the transaction, provided that you have disclosed complete and accurate details of your proposed use, no license is finally effective unless and until full payment is received from you (either by publisher or by CCC) as provided in CCC's Billing and Payment terms and conditions. If full payment is not received on a timely basis, then any license preliminarily granted shall be deemed automatically revoked and shall be void as if never granted. Further, in the event that you breach any of these terms and conditions or any of CCC's Billing and Payment terms and conditions, the license is automatically revoked and shall be void as if never granted. Use of materials as described in a revoked license, as well as any use of the materials beyond the scope of an unrevoked license, may constitute copyright infringement and publisher reserves the right to take any and all action to protect its copyright in the materials.

9. Warranties: Publisher makes no representations or warranties with respect to the licensed material.

10. Indemnity: You hereby indemnify and agree to hold harmless publisher and CCC, and their respective officers, directors, employees and agents, from and against any and all claims arising out of your use of the licensed material other than as specifically authorized pursuant to this license.

11. No Transfer of License: This license is personal to you and may not be sublicensed, assigned, or transferred by you to any other person without publisher's written permission.

12. No Amendment Except in Writing: This license may not be amended except in a writing signed by both parties (or, in the case of publisher, by CCC on publisher's behalf).

13. Objection to Contrary Terms: Publisher hereby objects to any terms contained in any purchase order, acknowledgment, check endorsement or other writing prepared by you, which terms are inconsistent with these terms and conditions or CCC's Billing and Payment terms and conditions. These terms and conditions, together with CCC's Billing and Payment terms and conditions (which are incorporated herein), comprise the entire agreement between you and publisher (and CCC) concerning this licensing transaction. In the event of any conflict between your obligations established by these terms and conditions and those established by CCC's Billing and Payment terms and conditions, these terms and conditions shall control.

APPENDIX B (continued)

14. Revocation: Elsevier or Copyright Clearance Center may deny the permissions described in this License at their sole discretion, for any reason or no reason, with a full refund payable to you. Notice of such denial will be made using the contact information provided by you. Failure to receive such notice will not alter or invalidate the denial. In no event will Elsevier or Copyright Clearance Center be responsible or liable for any costs, expenses or damage incurred by you as a result of a denial of your permission request, other

than a refund of the amount(s) paid by you to Elsevier and/or Copyright Clearance Center for denied permissions.

Terms & Conditions applicable to all Open Access articles published with Elsevier:

Additional Terms & Conditions applicable to each Creative Commons user license:

CC BY: The CC-BY license allows users to copy, to create extracts, abstracts and new works from the Article, to alter and revise the Article and to make commercial use of the Article (including reuse and/or resale of the Article by commercial entities), provided the user gives appropriate credit (with a link to the formal publication through the relevant DOI), provides a link to the license, indicates if changes were made and the licensor is not represented as endorsing the use made of the work. The full details of the license are available at http://creativecommons.org/licenses/by/4.0.

CC BY NC SA: The CC BY-NC-SA license allows users to copy, to create extracts, abstracts and new works from the Article, to alter and revise the Article, provided this is not done for commercial purposes, and that the user gives appropriate credit (with a link to the formal publication through the relevant DOI), provides a link to the license, indicates if changes were made and the licensor is not represented as endorsing the use made of the work. Further, any new works must be made available on the same conditions. The full details of the license are available at http://creativecommons.org/licenses/by-nc-sa/4.0.

CC BY NC ND: The CC BY-NC-ND license allows users to copy and distribute the Article, provided this is not done for commercial purposes and further does not permit distribution of the Article if it is changed or edited in any way, and provided the user gives appropriate credit (with a link to the formal publication through the relevant DOI), provides a link to the license, and that the licensor is not represented as endorsing the use made of the work. The full details of the license are available at http://creativecommons.org/licenses/by-nc-nd/4.0. Any commercial reuse of Open Access articles published with a CC BY NC SA or CC BY NC ND license requires permission from Elsevier and will be subject to a fee.

v1.9

Questions? customercare@copyright.com or +1-855-239-3415 (toll free in the US) or +1-978-646-2777.

APPENDIX B (continued)

THE AMERICAN ASSOCIATION FOR THE ADVANCEMENT OF SCIENCE LICENSE TERMS AND CONDITIONS

May 07, 2020

This Agreement between Tejumade Durowade ("You") and The American Association for the Advancement of Science ("The American Association for the Advancement of Science") consists of your license details and the terms and conditions provided by The American Association for the Advancement of Science and Copyright Clearance Center.

License Number	4823810771782
License date	May 07, 2020
Licensed Content Publisher	The American Association for the Advancement of Science
Licensed Content Publication	Science
Licensed Content Title	Quantum Coherent Tunable Coupling of Superconducting Qubits
Licensed Content Author	A. O. Niskanen,K. Harrabi,F. Yoshihara,Y. Nakamura,S. Lloyd,J. S. Tsai
Licensed Content Date	May 4, 2007
Licensed Content Volume	316
Licensed Content Issue	5825
Volume number	316
Issue number	5825
Type of Use	Thesis / Dissertation
Requestor type	Scientist/individual at a research institution
Format	Print and electronic
Portion	Figure
Number of figures/tables	1
Title	Micromagnetic Simulations of Circular Nano-magnets for Room Operable Quantum Cellular Automata
Institution name	University of Illinois at Chicago

Expected presentation date	May 2020
Portions	Figure 1
	Tejumade Durowade
	1831 218th Pl
Requestor Location	
	CHICAGO HEIGHTS, IL 60411
	United States
	Attn: Tejumade Durowade
Total	0.00 USD

Terms and Conditions

American Association for the Advancement of Science TERMS AND CONDITIONS

APPENDIX B (continued)

Regarding your request, we are pleased to grant you non-exclusive, non-transferable permission, to republish the AAAS material identified above in your work identified above, subject to the terms and conditions herein. We must be contacted for permission for any uses other than those specifically identified in your request above.

The following credit line must be printed along with the AAAS material: "From [Full Reference Citation]. Reprinted with permission from AAAS."

All required credit lines and notices must be visible any time a user accesses any part of the AAAS material and must appear on any printed copies and authorized user might make.

This permission does not apply to figures / photos / artwork or any other content or materials included in your work that are credited to non-AAAS sources. If the requested material is sourced to or references non-AAAS sources, you must obtain authorization from that source as well before using that material. You agree to hold harmless and indemnify AAAS against any claims arising from your use of any content in your work that is credited to non-AAAS sources.

If the AAAS material covered by this permission was published in Science during the years 1974 - 1994, you must also obtain permission from the author, who may grant or withhold permission, and who may or may not charge a fee if permission is granted. See original article for author's address. This condition does not apply to news articles.

The AAAS material may not be modified or altered except that figures and tables may be modified with permission from the author. Author permission for any such changes must be secured prior to your use.

Whenever possible, we ask that electronic uses of the AAAS material permitted herein include a hyperlink to the original work on AAAS's website (hyperlink may be embedded in the reference citation).

AAAS material reproduced in your work identified herein must not account for more than 30% of the total contents of that work.

AAAS must publish the full paper prior to use of any text.

AAAS material must not imply any endorsement by the American Association for the Advancement of Science.

This permission is not valid for the use of the AAAS and/or Science logos.

AAAS makes no representations or warranties as to the accuracy of any information contained in the AAAS material covered by this permission, including any warranties of

merchantability or fitness for a particular purpose.

APPENDIX B (continued)

If permission fees for this use are waived, please note that AAAS reserves the right to charge for reproduction of this material in the future.

Permission is not valid unless payment is received within sixty (60) days of the issuance of this permission. If payment is not received within this time period then all rights granted herein shall be revoked and this permission will be considered null and void.

In the event of breach of any of the terms and conditions herein or any of CCC's Billing and Payment terms and conditions, all rights granted herein shall be revoked and this permission will be considered null and void.

AAAS reserves the right to terminate this permission and all rights granted herein at its discretion, for any purpose, at any time. In the event that AAAS elects to terminate this permission, you will have no further right to publish, publicly perform, publicly display, distribute or otherwise use any matter in which the AAAS content had been included, and all fees paid hereunder shall be fully refunded to you. Notification of termination will be sent to the contact information as supplied by you during the request process and termination shall be immediate upon sending the notice. Neither AAAS nor CCC shall be liable for any costs, expenses, or damages you may incur as a result of the termination of this permission, beyond the refund noted above.

This Permission may not be amended except by written document signed by both parties.

The terms above are applicable to all permissions granted for the use of AAAS material. Below you will find additional conditions that apply to your particular type of use.

FOR A THESIS OR DISSERTATION
If you are using figure(s)/table(s), permission is granted for use in print and electronic versions of your dissertation or thesis. A full text article may be used in print versions only of a dissertation or thesis.

Permission covers the distribution of your dissertation or thesis on demand by ProQuest / UMI, provided the AAAS material covered by this permission remains in situ.

If you are an Original Author on the AAAS article being reproduced, please refer to your License to Publish for rules on reproducing your paper in a dissertation or thesis.

FOR JOURNALS:
Permission covers both print and electronic versions of your journal article, however the AAAS material may not be used in any manner other than within the context of your article.

FOR BOOKS/TEXTBOOKS:
If this license is to reuse figures/tables, then permission is granted for non-exclusive world rights in all languages in both print and electronic formats (electronic formats are defined below).

APPENDIX B (continued)

If this license is to reuse a text excerpt or a full text article, then permission is granted for non-exclusive world rights in English only. You have the option of securing either print or electronic rights or both, but electronic rights are not automatically granted and do garner additional fees. Permission for translations of text excerpts or full text articles into other languages must be obtained separately.

Licenses granted for use of AAAS material in electronic format books/textbooks are valid only in cases where the electronic version is equivalent to or substitutes for the print version of the book/textbook. The AAAS material reproduced as permitted herein must remain in situ and must not be exploited separately (for example, if permission covers the use of a full text article, the article may not be offered for access or for purchase as a stand-alone unit), except in the case of permitted textbook companions as noted below.

You must include the following notice in any electronic versions, either adjacent to the reprinted AAAS material or in the terms and conditions for use of your electronic products: "Readers may view, browse, and/or download material for temporary copying purposes only, provided these uses are for noncommercial personal purposes. Except as provided by law, this material may not be further reproduced, distributed, transmitted, modified, adapted, performed, displayed, published, or sold in whole or in part, without prior written permission from the publisher."

If your book is an academic textbook, permission covers the following companions to your textbook, provided such companions are distributed only in conjunction with your textbook at no additional cost to the user:

- Password-protected website
- Instructor's image CD/DVD and/or PowerPoint resource
- Student CD/DVD

All companions must contain instructions to users that the AAAS material may be used for non-commercial, classroom purposes only. Any other uses require the prior written permission from AAAS.

If your license is for the use of AAAS Figures/Tables, then the electronic rights granted herein permit use of the Licensed Material in any Custom Databases that you distribute the electronic versions of your textbook through, so long as the Licensed Material remains within the context of a chapter of the title identified in your request and cannot be downloaded by a user as an independent image file.

Rights also extend to copies/files of your Work (as described above) that you are required to provide for use by the visually and/or print disabled in compliance with state and federal laws.

APPENDIX B (continued)

This permission only covers a single edition of your work as identified in your request.

FOR NEWSLETTERS:
Permission covers print and/or electronic versions, provided the AAAS material reproduced as permitted herein remains in situ and is not exploited separately (for example, if permission covers the use of a full text article, the article may not be offered for access or for purchase as a stand-alone unit)

FOR ANNUAL REPORTS:
Permission covers print and electronic versions provided the AAAS material reproduced as permitted herein remains in situ and is not exploited separately (for example, if permission covers the use of a full text article, the article may not be offered for access or for purchase as a stand-alone unit)

FOR PROMOTIONAL/MARKETING USES:
Permission covers the use of AAAS material in promotional or marketing pieces such as information packets, media kits, product slide kits, brochures, or flyers limited to a single print run. The AAAS Material may not be used in any manner which implies endorsement or promotion by the American Association for the Advancement of Science (AAAS) or Science of any product or service. AAAS does not permit the reproduction of its name, logo or text on promotional literature.

If permission to use a full text article is permitted, The Science article covered by this permission must not be altered in any way. No additional printing may be set onto an article copy other than the copyright credit line required above. Any alterations must be approved in advance and in writing by AAAS. This includes, but is not limited to, the placement of sponsorship identifiers, trademarks, logos, rubber stamping or self-adhesive stickers onto the article copies.

Additionally, article copies must be a freestanding part of any information package (i.e. media kit) into which they are inserted. They may not be physically attached to anything, such as an advertising insert, or have anything attached to them, such as a sample product. Article copies must be easily removable from any kits or informational packages in which they are used. The only exception is that article copies may be inserted into three-ring binders.

FOR CORPORATE INTERNAL USE:
The AAAS material covered by this permission may not be altered in any way. No additional printing may be set onto an article copy other than the required credit line. Any alterations must be approved in advance and in writing by AAAS. This includes, but is not limited to the placement of sponsorship identifiers, trademarks, logos, rubber stamping or self-adhesive stickers onto article copies.

If you are making article copies, copies are restricted to the number indicated in your request and must be distributed only to internal employees for internal use.

APPENDIX B (continued)

If you are using AAAS Material in Presentation Slides, the required credit line must be visible on the slide where the AAAS material will be reprinted

If you are using AAAS Material on a CD, DVD, Flash Drive, or the World Wide Web, you must include the following notice in any electronic versions, either adjacent to the reprinted AAAS material or in the terms and conditions for use of your electronic products: "Readers may view, browse, and/or download material for temporary copying purposes only, provided these uses are for noncommercial personal purposes. Except as provided by law, this material may not be further reproduced, distributed, transmitted, modified, adapted, performed, displayed, published, or sold in whole or in part, without prior written permission from the publisher." Access to any such CD, DVD, Flash Drive or Web page must be restricted to your organization's employees only.

FOR CME COURSE and SCIENTIFIC SOCIETY MEETINGS:
Permission is restricted to the particular Course, Seminar, Conference, or Meeting indicated in your request. If this license covers a text excerpt or a Full Text Article, access to the reprinted AAAS material must be restricted to attendees of your event only (if you have been granted electronic rights for use of a full text article on your website, your website must be password protected, or access restricted so that only attendees can access the content on your site).

If you are using AAAS Material on a CD, DVD, Flash Drive, or the World Wide Web, you must include the following notice in any electronic versions, either adjacent to the reprinted AAAS material or in the terms and conditions for use of your electronic products: "Readers may view, browse, and/or download material for temporary copying purposes only, provided these uses are for noncommercial personal purposes. Except as provided by law, this material may not be further reproduced, distributed, transmitted, modified, adapted, performed, displayed, published, or sold in whole or in part, without prior written permission from the publisher."

FOR POLICY REPORTS:
These rights are granted only to non-profit organizations and/or government agencies. Permission covers print and electronic versions of a report, provided the required credit line appears in both versions and provided the AAAS material reproduced as permitted herein remains in situ and is not exploited separately.

FOR CLASSROOM PHOTOCOPIES:
Permission covers distribution in print copy format only. Article copies must be freestanding and not part of a course pack. They may not be physically attached to anything or have anything attached to them.

FOR COURSEPACKS OR COURSE WEBSITES:
These rights cover use of the AAAS material in one class at one institution. Permission is valid only for a single semester after which the AAAS material must be removed from the Electronic Course website, unless new permission is obtained for an additional semester. If

APPENDIX B (continued)

the material is to be distributed online, access must be restricted to students and instructors enrolled in that particular course by some means of password or access control.

FOR WEBSITES:
You must include the following notice in any electronic versions, either adjacent to the reprinted AAAS material or in the terms and conditions for use of your electronic products: "Readers may view, browse, and/or download material for temporary copying purposes only, provided these uses are for noncommercial personal purposes. Except as provided by law, this material may not be further reproduced, distributed, transmitted, modified, adapted, performed, displayed, published, or sold in whole or in part, without prior written permission from the publisher."

Permissions for the use of Full Text articles on third party websites are granted on a case by case basis and only in cases where access to the AAAS Material is restricted by some means of password or access control. Alternately, an E-Print may be purchased through our reprints department (brocheleau@rockwaterinc.com).

REGARDING FULL TEXT ARTICLE USE ON THE WORLD WIDE WEB IF YOU ARE AN 'ORIGINAL AUTHOR' OF A SCIENCE PAPER

If you chose "Original Author" as the Requestor Type, you are warranting that you are one of authors listed on the License Agreement as a "Licensed content author" or that you are acting on that author's behalf to use the Licensed content in a new work that one of the authors listed on the License Agreement as a "Licensed content author" has written.

Original Authors may post the 'Accepted Version' of their full text article on their personal or on their University website and not on any other website. The 'Accepted Version' is the version of the paper accepted for publication by AAAS including changes resulting from peer review but prior to AAAS's copy editing and production (in other words not the AAAS published version).

FOR MOVIES / FILM / TELEVISION:
Permission is granted to use, record, film, photograph, and/or tape the AAAS material in connection with your program/film and in any medium your program/film may be shown or heard, including but not limited to broadcast and cable television, radio, print, world wide web, and videocassette.

The required credit line should run in the program/film's end credits.

FOR MUSEUM EXHIBITIONS:
Permission is granted to use the AAAS material as part of a single exhibition for the duration of that exhibit. Permission for use of the material in promotional materials for the exhibit must be cleared separately with AAAS (please contact us at permissions@aaas.org).

APPENDIX B (continued)

FOR TRANSLATIONS:
Translation rights apply only to the language identified in your request summary above.

The following disclaimer must appear with your translation, on the first page of the article, after the credit line: "This translation is not an official translation by AAAS staff, nor is it endorsed by AAAS as accurate. In crucial matters, please refer to the official English-language version originally published by AAAS."

FOR USE ON A COVER:
Permission is granted to use the AAAS material on the cover of a journal issue, newsletter issue, book, textbook, or annual report in print and electronic formats provided the AAAS material reproduced as permitted herein remains in situ and is not exploited separately

By using the AAAS Material identified in your request, you agree to abide by all the terms and conditions herein.

Questions about these terms can be directed to the AAAS Permissions department permissions@aaas.org.

Other Terms and Conditions:

v 2

Questions? customercare@copyright.com or +1-855-239-3415 (toll free in the US) or +1-978-646-2777.

APPENDIX B (continued)

APS physics — **American Physical Society Reuse and Permissions License**

07-May-2020

This license agreement between the American Physical Society ("APS") and Tejumade Durowade ("You") consists of your license details and the terms and conditions provided by the American Physical Society and SciPris.

Licensed Content Information

License Number:	RNP/20/MAY/025581
License date:	07-May-2020
DOI:	10.1103/PhysRevLett.90.127901
Title:	Tunable Coupling of Superconducting Qubits
Author:	Alexandre Blais, Alexander Maassen van den Brink, and Alexandre M. Zagoskin
Publication:	Physical Review Letters
Publisher:	American Physical Society
Cost:	USD $ 0.00

Request Details

Does your reuse require significant modifications: No

Specify intended distribution locations:	United States
Reuse Category:	Reuse in a thesis/dissertation
Requestor Type:	Student
Items for Reuse:	Figures/Tables
Number of Figure/Tables:	1
Figure/Tables Details:	Figure 1
Format for Reuse:	Electronic

Information about New Publication:

University/Publisher:	University of Illinois at Chicago
Title of dissertation/thesis:	Micromagnetic Simulations of Circular Nano-magnets for Room Operable Quantum Cellular Automata
Author(s):	Tejumade Durowade
Expected completion date:	May. 2020

License Requestor Information

Name:	Tejumade Durowade
Affiliation:	Individual
Email Id:	tdurow3@uic.edu
Country:	United States

APPENDIX B (continued)

APS physics™ American Physical Society
Reuse and Permissions License
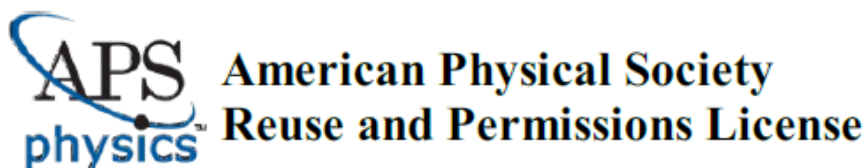
TERMS AND CONDITIONS

The American Physical Society (APS) is pleased to grant the Requestor of this license a non-exclusive, non-transferable permission, limited to Electronic format, provided all criteria outlined below are followed.

1. You must also obtain permission from at least one of the lead authors for each separate work, if you haven't done so already. The author's name and affiliation can be found on the first page of the published Article.

2. For electronic format permissions, Requestor agrees to provide a hyperlink from the reprinted APS material using the source material's DOI on the web page where the work appears. The hyperlink should use the standard DOI resolution URL, http://dx.doi.org/{DOI}. The hyperlink may be embedded in the copyright credit line.

3. For print format permissions, Requestor agrees to print the required copyright credit line on the first page where the material appears: "Reprinted (abstract/excerpt/figure) with permission from [(FULL REFERENCE CITATION) as follows: Author's Names, APS Journal Title, Volume Number, Page Number and Year of Publication.] Copyright (YEAR) by the American Physical Society."

4. Permission granted in this license is for a one-time use and does not include permission for any future editions, updates, databases, formats or other matters. Permission must be sought for any additional use.

5. Use of the material does not and must not imply any endorsement by APS.

6. APS does not imply, purport or intend to grant permission to reuse materials to which it does not hold copyright. It is the requestor's sole responsibility to ensure the licensed material is original to APS and does not contain the copyright of another entity, and that the copyright notice of the figure, photograph, cover or table does not indicate it was reprinted by APS with permission from another source.

7. The permission granted herein is personal to the Requestor for the use specified and is not transferable or assignable without express written permission of APS. This license may not be amended except in writing by APS.

8. You may not alter, edit or modify the material in any manner.

9. You may translate the materials only when translation rights have been granted.

10. APS is not responsible for any errors or omissions due to translation.

11. You may not use the material for promotional, sales, advertising or marketing purposes.

12. The foregoing license shall not take effect unless and until APS or its agent, Aptara, receives payment in full in accordance with Aptara Billing and Payment Terms and Conditions, which are incorporated herein by reference.

13. Should the terms of this license be violated at any time, APS or Aptara may revoke the license with no refund to you and seek relief to the fullest extent of the laws of the USA. Official written notice will be made using the contact information provided with the permission request. Failure to receive such notice will not nullify revocation of the permission.

14. APS reserves all rights not specifically granted herein.

15. This document, including the Aptara Billing and Payment Terms and Conditions, shall be the entire agreement between the parties relating to the subject matter hereof.

.

VITA

NAME: Tejumade Durowade

EDUCATION: B.S., Electrical Engineering, University of Illinois at Chicago, Chicago, Illinois, 2013.

M.S., Electrical Engineering, University of Illinois at Chicago, Chicago, Illinois, 2016.

Ph.D., Electrical Engineering, University of Illinois at Chicago, Chicago, Illinois, 2020.

WORK EXPERIENCE: Graduate Research Assistant, Nanotechnology Core Facility, May 2015-May 2020

Teaching Assistant, University of Illinois at Chicago, Jan 2017-May 2020

Internship, EPIR Technologies, May 2012-Aug 2012

Internship, University of Sydney, School of Physics, May 2011-July 2011

HONORS: Scholarship Association for UIC, Sargent and Lundy Award, 2012

ABSTRACTS: Durowade, T., Metlushko, V., (Oct. 2019). 'Micro-magnetic simulations of correlated switching in touching nano-magnetic element.' Presented at the AVS 66th International Symposium and Exhibition, Columbus, OH.

Admassu, D., Durowade, T., Gao Wei., Velicu, S., Sivananthan, S., (Oct. 2017) 'Micro-opto-electro-mechanical (MOEMS) MWIR Fabry-Pérot filters for hyperspectral imaging'. Presented at the II-VI Workshop, Chicago, IL.

PUBLICATIONS: Durowade, T., Metlushko, V., 'Micro-magnetic simulations of correlated switching in touching circular nano-magnetic elements', *AIP Adv*., *vol*. 10, *no*. 3, 2020.

Palacios, F., Durowade, T., Feinerman, A., Busta, H., Gorski, R., 'Investigation of field emission properties of 2-D electron accumulation and inversion layers in cleaved silicon MOS capacitors and transistors.' To be presented at the virtual International Vacuum Nanoelectronics Conference, Lyon, France, July, 2020.